Doctoral Dissertation

Molecular Alignment Control and Crystal Structure Analysis in Solution-processed Thin Films of Columnar Liquid-crystalline Semiconductor

Masashi Ohmori

大森 雅志

January 2018

Graduate School of Engineering,

Osaka University

Contents

Abstract

Organic electronics fabricated by printing technology have attracted much attention in recent years. Organic semiconductors form unique crystal structures based on the molecular structure, and their electrical properties depend on the crystal structure. However, typical organic thin films fabricated by solution process consist of amorphous or non-oriented polycrystals. Typical organic semiconductors exhibit anisotropic electrical transport properties. The best carrier transport properties are obtained when the molecular orientation is controlled. Thus, molecular alignment control in thin films is important for organic electrical applications.

In this study, an alkyl-substituted phthalocyanine, 1,4,8,11,15,18,22,25-octahexylphthalocyanine ($C6PcH_2$), was used as an organic semiconductor. $C6PcH_2$ is a solution-processable low-molecular-weight semiconductor and exhibits the discotic liquid crystalline (LC) phase. Alkyl-substituted phthalocyanines tend to form columnar structures, and a uniaxial carrier transport property along the column axis is expected. In particular, $C6PcH_2$ exhibits excellent carrier transport properties, such as hole mobility of 1.4 cm^2/Vs and electron mobility of 0.5 cm^2/Vs. Solar cells made of $C6PcH_2$ exhibit a power conversion efficiency of 4.2 %. $C6PcH_2$ exhibits excellent electrical properties; however, molecular alignment control in thin films of $C6PcH_2$ has not been carried out so far. Moreover, $C6PcH_2$ exhibits the LC phase, and LC materials exhibit unique properties, such as large domains and self-organization; therefore, molecular alignment control can be used to investigate the unique properties of LC materials.

In the present research, molecular alignment control of columnar LC materials in thin films was carried out to enhance their carrier transport properties, and their molecular packing structure and molecular alignment were investigated. The following is a summary of each chapter.

Chapter 1: Introduction

The background, purpose, and overview of the dissertation are described. The fundamentals of molecular alignment control and crystal structure analysis in thin films are also described.

Chapter 2: Single crystal structure and its thermal behavior

Single crystals of C6PcH$_2$ were fabricated by recrystallization, and the crystal structures were determined. C6PcH$_2$ exhibited two types of polymorphism, α-type and β-type, and the conditions required for forming each polymorphism was investigated by thermal analysis.

The irreversible thermal phase transition from α to β-type crystal was observed. The stability is discussed using Gibbs' free energy. The α-type crystals are stable state at room temperature, and can form only if the crystals slowly grow at room temperature.

Simulation of carrier transport properties was carried out by the density functional theory (DFT) calculation using the crystal structure determined by single crystal X-ray analysis. The α-type crystals exhibited one order higher carrier mobility than the β-type crystals. The results show that the device performance is enhanced when α-type crystals.

Chapter 3: Molecular packing structure in thin film prepared by spin-coating

Molecular packing structure in the thin films of C6PcH$_2$ prepared by spin-coating was measured by the grazing incidence wide angle X-ray scattering (GIWAXS) method. The X-ray diffraction (XRD) peaks derived from intercolumn and intermolecular distances was detected, and the molecular packing structure was simulated using the XRD patterns by considering the extinction rule. The simulated molecular packing structure was almost equal in all the β-type crystals, and the molecular stacking direction is parallel to the substrate; moreover, the simulated molecular packing structure in the thin film was ascertained by Fourier analysis.

Chapter 4: Molecular alignment control and molecular packing structure analysis in thin film

Uniaxially planar alignment of C6PcH$_2$ molecules in thin films was induced by the bar-coating method. The speed of film fabrication was controlled to be lower than that of the crystal growth, and uniaxial crystal growth was induced in the thin films. Uniaxial planar alignment was confirmed to be induced over an area of 1 mm^2 by polarized optical microscopy, and the direction of the molecular alignment was clarified by the polarized absorption spectrum measurement and atomic force microscopy.

The three-dimensional (3-D) molecular packing structure in the molecularly oriented film

was determined by the GIWAXS technique that involves sample rotation. In the case of the conventional GIWAXS technique with a fixed sample, determination of the 3-D molecular packing structure in the film is not possible; however, when the GIWAXS technique is used with sample rotation, the 3-D molecular packing structure in the film can be determined. Moreover, the positions and intensities of the XRD peaks were calculated by using the crystal structure of β-type crystals of $C6PcH_2$, and the XRD patterns were reproduced. The reliability factor, which represents the difference between the simulated and measured results, was calculated. The technique of detail crystal structure analysis in a uniaxial molecularly oriented thin film was proposed using the reliability factor.

Homeotropic alignment in the film of $C6PcH_2$ was induced using the LC phase. A $C6PcH_2$ films was covered with a poly(vinylphenol) layer, and the sample was annealed at a temperature of the LC phase, and $C6PcH_2$ molecules in the film were reoriented. The cause of inducing homeotropic alignment was discussed based on molecular alignment in the LC phase determined by X-ray structure analysis.

Chapter 5: Carrier transport properties of molecularly oriented thin films and its device applications

Field effect transistors (FETs) and solar cells were fabricated by using planar and homeotropically oriented thin films, respectively, and the electrical properties of FETs and solar cells were investigated. The high mobility along the column axis of $C6PcH_2$ was obtained by using the transfer characteristics of FETs, and the mobility was compared with the simulated mobility determined by the DFT calculation. The photovoltaic properties were discussed by taking the mobility measured by the photo-CELIV method. The mobility perpendicular to the substrate was enhanced by inducing homeotropic alignment, and the photovoltaic properties improved. This production process of inducing homeotropic alignment is effective for solar cell applications.

Chapter 6: Conclusions

The results and findings discussed in chapters 2–5 are summarized, and the main concluding remarks are drawn.

Chapter 1.

Introduction

1.1 Introductory remarks

Semiconductor devices utilizing inorganic semiconductors of silicon have made our lives more convenient. Inorganic semiconductors exhibit excellent characteristics for device application, such as high carrier mobility and stability, and the devices utilizing such semiconductors have long been studied. Consequently, the electrical properties of these semiconductors are close to the theoretical limitation, specifically power conversion efficiency of solar cells and degree of integration of transistors [1].

Organic semiconductors have attracted attention as the next-generation functional materials. These semiconductors consist of many atoms, such as hydrogen, carbon, and contain nitrogen, and numerous combination of atoms. Excellent characteristics, such as high solubility in typical organic solvents, and optical and electrical properties, can be introduced by varying the molecular design. To obtain high solubility, thin films can be fabricated by the solution process, and large-area and low-cost products are expected [2]. Plastic substrates can be used because of a low process temperature. Organic semiconductors are relatively soft materials. Therefore, flexible devices can be fabricated. Moreover, organic semiconductors exhibit excellent optical properties that are useful in solar cells, such as broad absorption in the near-infrared and visible light regions [3] and high carrier mobility exceeding that of amorphous silicone [4], have been reported.

Examples of such organic semiconductor devices include electro-luminescence lightings, organic solar cells, and organic field effect transistors. However, most of them are not popular, because of some inherent problems. One of the problems that hinder their practical use is the control of the molecular alignment in thin films. Generally, organic semiconductors with ex-

cellent carrier transport properties possess a highly oriented molecular packing structure, and are made of crystals with anisotropic carrier transport properties. In devices, the direction of the carrier transport is determined; therefore, control of the molecular orientation is necessary for device application. Many studies have long been carried out on molecularly oriented thin films [5]; however, the orientation process has not been established. Even analysis methods for the molecularly oriented thin films are not resolved.

The preferred method for preparing a molecularly oriented thin film is a wet process. A number of studies have addressed the fabrication of molecularly oriented thin films by utilizing liquid crystalline (LC) semiconductors by a wet process [6], [7]. LC materials have the fluidity of liquids as well as regularity of solids, and also exhibit many unique properties such as self-organization. Thus LC materials are considered to be suitable for control of molecular alignment.

In this study, columnar LC semiconductors were used as organic semiconductors. Columnar LC materials tend to form the columnar structure, and they are considered to exhibit high carrier mobility along the column axis. The molecularly oriented thin films utilizing columnar LC materials was fabricated, and the molecular packing structure in the thin films was investigated. Additionally, the carrier transport and photovoltaic properties were investigated.

1.2 Organic semiconductors

1.2.1 Classification of organic semiconductors

Organic semiconductors can be broadly classified into two categories: small molecules and polymers. Conductive polymer materials consist of main chain backbones with alternating double and single bonds between carbon atoms. Therefore, conductive polymer materials exhibit high electrical conductivity along the main chain. Uniform thin films are essential for device applications; however, general chain conductive polymers are insoluble in common organic solvents; therefore, fabrication of thin films by the solution process is impossible. Moreover, thin film fabrication by the dry process is also impossible because of the thermal decomposition of the main chains of polymers. Substituent groups like long alkyl chains has been introduced to polymers by synthetic modification for reducing the cohesive force between the polymers and improving the solubility in common organic solvents. This has made thin film fabrication by the wet process possible [8].

Small molecular semiconductors have extended π-conjugated systems. Uniform thin films can be fabricated by the vacuum deposition method, and organic electronic devices utilizing small molecular semiconductors have long been studied. Some conductive polymers and small molecular semiconductors form unique crystal structures based on each molecular shapes. If the distance between two molecules are sufficiently close, superposition of wave function of the two molecules can be increased, and efficient carrier transport can be obtained. Carrier transport properties depend on the molecular packing structure, while electrical anisotropy depend on the plane direction of the crystal. Therefore, development of organic materials with excellent carrier transport properties and control of molecular alignment in the devices are important to enhance the device properties.

Purification of polymer materials is difficult owing to the high degree of polymerization; however, small molecular materials can be easily purified. Films with highly ordered molecular alignment can be fabricated owing to high purity, and some of them exhibited high carrier mobilities. Single crystals have been shown as examples of the highly ordered molecular alignment, and carrier mobility in the single crystals of pentacene and rubrene obtained by the transistor measurement exceeded that of amorphous silicon [9], [10].

Film formation involving non-substituted small molecules can be carried out only with the dry process because of the low solubility. For such device applications, solution processes should be adopted because of the low cost and flexible and large-area products. Introducing substitutes to small molecular semiconductors has been researched to improve the solubility in organic solvents.

In this dissertation, solution-processable small molecular semiconductors were used for device applications, such as solar cells and field-effect transistors (FETs). Control of molecular alignment in the devices was carried out for enhancing the device properties, and the molecular packing structure was investigated.

1.2.2 Liquid crystalline phthalocyanine

Figure 1.1(a) shows the molecular packing structure of non-substituted phthalocyanine (Pc). Pcs are well-known small molecular semiconductors exhibiting high and stable electrical properties [11], and the development of organic devices utilizing Pcs, such as solar cells [12], [13] and transistors [14], has been reported previously. For such device applications, solution processes

should be adopted; however, thin films of Pcs can only be fabricated by the deposition method owing to their low solubility in common organic solvents. Therefore, alkyl chains have been introduced to the cores of Pcs to enhance the solubility in organic solvents [15].

Two types of alkyl-substituted phthalocyanines have been reported as columnar LC materials [16]. One is peripherally alkyl-substituted Pcs, which are introduced at the position of 2,3,9,10,16,17,23,24 of Pc cores (Fig. 1.1(a)), and the other is non-peripherally alkyl-substituted Pcs, introduced at the position of 1,4,8,11,15,18,22,25 of Pc cores (Fig. 1.1(a)). Both of them exhibited a discotic LC phase owing to the introduction of long alkyl-chains and tend to form a columnar structure. The columnar structure is considered to be appropriate for the carrier transport, because charge carriers are considered to be efficiently transported along the column axis [17].

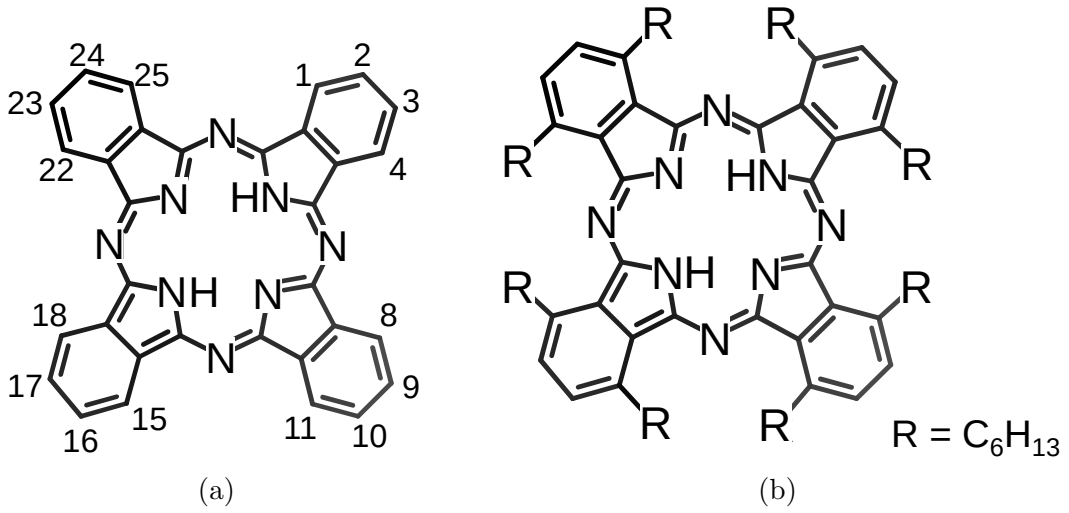

Fig. 1.1 Molecular structures of (a) non-substituted Pc and (b) C6PcH$_2$.

Peripherally alkyl-substituted Pcs show the ordered columnar phase, in which the Pc cores are orderly aligned in the column [16], while non-peripherally alkyl-substituted Pcs show the disordered columnar phase, in which the Pc cores are disorderly aligned in the column [18]. Generally, the carrier mobility increases as the molecular orientational order increases [19]; therefore, peripherally alkyl-substituted Pcs are considered to exhibit higher carrier mobility than non-peripherally alkyl-substituted Pcs. The carrier mobilities of the peripherally and non-peripherally alkyl-substituted Pcs were of the order of 10^{-3} and 10^{-1}cm^2/Vs, respectively [20], [21], [22]; in other words, non-peripherally alkyl-substituted Pcs exhibited two orders higher

carrier mobility than that of peripherally ones. The origin of better carrier transport properties of non-peripherally alkyl-substituted Pcs has not been clarified. Carrier transport properties mainly depend on the molecular packing structure; therefore, clarification of their molecular packing structure is important for clarification of their better carrier transport properties.

In particular, non-peripherally hexyl-substituted Pc, 1,4,8,11,15,18,22,25-octahexylphthalocyanine ($C6PcH_2$), exhibits excellent carrier transport properties, such as hole mobility of 1.4 cm^2/Vs and electron mobility of 0.5 cm^2/Vs, which were evaluated by the time-of-flight (TOF) measurement [23], [24]. Figure 1.1(b) shows the molecular structure of $C6PcH_2$. $C6PcH_2$ also exhibits an LC phase and tends to form the columnar structure in the crystal phase as well as the LC phase. Therefore, molecularly oriented thin films are expected to have unique characteristics of LC, such as large domains and self-organization.

As a device application of $C6PcH_2$, thin-film solar cells with a bulk heterojunction of $C6PcH_2$ and 1-(3-methoxycarbonyl)-propyl-(6,6)C61 (PCBM), which exhibited a high efficiency of 4.2%, have been reported [25]. The bulk heterojunction film of $C6PcH_2$ and PCBM is fabricated by spin-coating, but the molecular alignment of $C6PcH_2$ in the film cannot be controlled. $C6PcH_2$ is considered to exhibit carrier transport property along the column axis [17]. Thus, control of the direction of the column axis in films is considered to be important to improve the photovoltaic properties. However, molecularly oriented thin films of $C6PcH_2$ have not been fabricated.

Control of molecular alignment in films is required for improving the device properties, and the detail crystal structure of $C6PcH_2$ was necessary to evaluate the molecular alignment and molecular packing structure in the films. The crystal structures of $C6PcH_2$ in the LC phase and single-crystalline state have been reported in previous works [26], [27]. $C6PcH_2$ in the LC phase forms a pseudo-disordered hexagonal columnar (Col_{hd}) mesophase because of the free motion of its alkyl chains, and the column interval is about 21 Å [26]. The tilt angle of the normal vector of the Pc core is 26° from the column axis in each column. The crystal structure in the single-crystalline state is determined to be triclinic with space group $P1$, $a = 9.2668(9)$, $b = 9.7323(8)$, $c = 19.991(2)$ Å, $\alpha = 100.964(7)$, $\beta = 91.166(7)$, and $\gamma = 95.899(7)°$ [27]. The tilt angle of the normal vector of Pc core is 68° from the column axis in each column. That is, the molecular packing structure in the single-crystal state is different from that in the LC phase. Moreover, the molecular packing structure measured by single-crystal X-ray structure analysis did not match that in the film prepared by spin-coating, which is used for solar cells [28]. Non-

substituted Pcs form two types of crystal polymorphism [29]. Thus, C6PcH_2 is also considered to form crystal polymorphism; however, the crystal structure of C6PcH_2 has not been clarified.

1.2.3 Molecular orientation control of liquid crystalline materials

The carrier transport properties of the organic thin film depend on the molecular packing structure. The carrier transport of organic semiconductors are generally described by the hopping model [30], [31]. In the hopping model, the carrier mobility is calculated by using the overlap integral of the molecular orbital, and the overlap integral depends on the distance between molecules. For example, the molecular stacking distance of the columnar LC semiconductors is shorter than the intercolumn distance; therefore, the columnar LC semiconductors exhibit one-dimensional carrier transport properties along the column axis. These properties depend on the molecular shape.

In addition, the carrier transport properties in the organic thin film also depend on the molecular alignment, and the carrier transport direction in devices depends on the device structure. Accordingly, control of molecular alignment in the thin film is required to enhance the device properties. Discotic LC materials tend to form the columnar structure. Molecular alignment in the film can be broadly classified into two types: planar and homeotropic alignment. The schematic of the planar and homeotropic alignment in the film is shown in Fig. 1.2. The charge carriers are efficiently transported along the column axis, i.e., films with induced planar and homeotoropic alignment exhibit excellent carrier transport properties parallel and perpendicular to the substrate, respectively. For typical transistor applications, the direction of the carrier transport is parallel to the substrate; thus, the films with induced planar alignment are suitable. For typical solar cell applications, the direction of the carrier transport should be perpendicular to the substrate; thus, the films with induced homeotropic alignment are suitable.

Control of molecular alignment of LC materials in the films have long been studied, and many production processes have been reported. The processes for controlling the speed and direction of the crystal growth have been reported by using printing processes, such as zone-casting [32], inkjet [33], and blade-coated processes [6], [34]. Secondly, the processes of exerting force to the films, such as exerting shearing stress [35], rubbing method [36], drawing method [37], and frictional transfer method [38] have also been reported. Thirdly, fabrication of films on ground alignment layers has also been reported. As examples of a ground alignment layer, polyimide

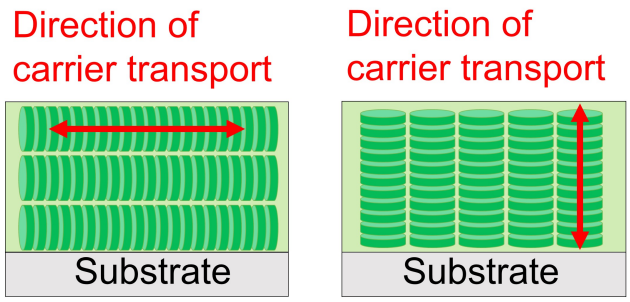

(a) (b)

Fig. 1.2 Schematic diagrams of (a) planar and (b) homeotropic alignment of discotic LC materials in films. Red two-way arrows represent the direction of the efficient carrier transport.

and poly(tetrafluoroethylene) alignment layers obtained by the rubbing method and frictional transfer method, respectively, were used [39], [40], [41]. Fourthly, the process of application of external field, such as polarized light [42] and magnetic field [43], fifthly, the processes of using the unique characteristic of an LC phase, such as large domains and self-organization, have also been reported. For example, molecularly oriented films have been fabricated by using molecular alignment and packing structure in the smectic E phase, which is a highly ordered liquid crystalline phase [7]. These molecularly oriented thin films have been used for electrical devices, such as transistors and solar cells, and reported to exhibit excellent properties [44], [45].

1.2.4 Organic thin film transistor

Recently, properties of organic thin film transistors have been significantly improved, and the device applications such as wireless tags and display are expected. Additionally, large-area electronics, such as electronic papers and sensors, can also be prepared by taking advantage of large-area and flexible products. The fabrication cost of organic thin film transistors prepared by printing a certain area is calculated to be two orders of magnitude lower than that of silicon transistors [46]; thus the organic thin film transistors are effective for preparing large-area devices.

The principle of the operation of OFETs can be described as follows. The schematic diagram of the top-contact bottom-gate type FET is shown in Fig. 1.3(a). FETs consist of source, drain, and gate electrodes and semiconductor and insulator layers, as with silicon transistors. Charge carriers are supplied from the source electrode and stored in the semiconductor layer, and then,

the carriers are withdrawn from the drain electrodes.

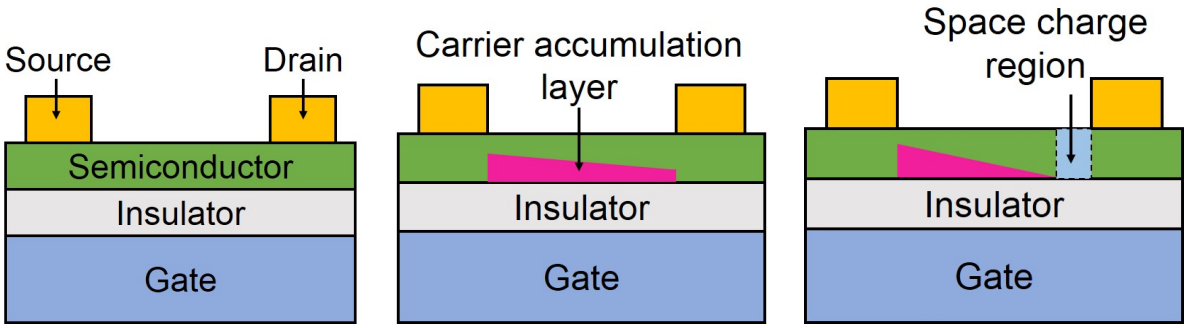

(a) (b) (c)

Fig. 1.3 Schematic diagrams of the top-contact bottom-gate type FET under various conditions: (a) a region of a low gate voltage ($V_g < V_{th}$), (b) a linear region ($V_g < V_{th}$ and $V_d < V_g - V_{th}$), and (c) a saturation region ($V_g < V_{th}$ and $V_d > V_g - V_{th}$).

Schematic diagrams of the FETs under various conditions such as (i) a region of a low gate voltage ($V_g < V_{th}$), (ii) a linear region ($V_g < V_{th}$ and $V_d < V_g - V_{th}$), and (iii) a saturation region ($V_g < V_{th}$ and $V_d > V_g - V_{th}$) are shown in Fig. 1.3; here, V_g, V_d, and V_{th} are gate, drain, and threshold voltages, respectively. When $V_g < V_{th}$, even if the drain voltage is applied, drain current cannot be observed because the semiconductor layer exhibits low conductivity, as shown in Fig. 1.3(a). In the case of $V_g > V_{th}$, the charge carriers accumulate in an area near an interface with the insulator layer, and the carrier accumulation layer is formed as shown in Fig. 1.3(b). The gate voltage formed at the carrier accumulation layer is called threshold voltage. When $V_d < V_g - V_{th}$, the resistance of the carrier accumulation layer is regard as a constant, and the drain current is directly proportional to the drain voltage according to Ohm's law. The region is called a linear region and the properties can be calculated by Eq. (1.1).

$$I_d = \frac{W}{L}\mu C_{OX}\left[(V_g - V_{th}) - \frac{1}{2}V_d^2\right], \tag{1.1}$$

where, I_d is the drain current, W and L are the width and length of the channel, respectively, μ is mobility, and C_{OX} is capacitance of the insulator layer.

When $V_d > V_g - V_{th}$, the difference between the drain and gate voltages vanishes, and the carrier accumulation layer near the drain electrode disappears as shown in Fig. 1.3(c). This area is called the space charge region. In this case, even if the drain voltage increased, the drain voltage consumed during the extension of the space charge region, and the drain current

is saturated as shown in Eq. (1.2). The region is called the saturation region.

$$I_{\mathrm{d}} = \frac{W}{2L}\mu C_{\mathrm{OX}} \left(V_{\mathrm{g}} - V_{\mathrm{th}}\right)^2 , \tag{1.2}$$

In this study, the carrier mobilities of FETs were calculated by using the I_{d}–V_{g} characteristics, which are called transfer characteristics, in the saturation region. Equation (1.2) is rewritten by using the inclination of the $\sqrt{I_{\mathrm{d}}}$–V_{g} characteristic, and the carrier mobility of the FET is calculated by Eq. (1.3).

$$\frac{\partial \sqrt{I_{\mathrm{d}}}}{\partial V_{\mathrm{g}}} = \sqrt{\frac{W}{2L}\mu C_{\mathrm{OX}}}. \tag{1.3}$$

1.2.5 Organic thin film solar cell

For Si-based solar cells, p-type and n-type semiconductors are prepared by ion implantation, and p-n junction diodes are manufactured. In the case of organic thin film solar cells, two types of molecules are used as donor and acceptor materials. Additionally, the bulk-heterojunction films of donor and acceptor materials are used as the active layer of the typical organic cells.

The schematic diagram of the photoelectric conversion process of organic solar cells is shown in Fig. 1.4. The operation principle of the organic solar cells can be divided into four steps: (i) light absorption and exciton formation, (ii) diffusion of the generated excitons to the boundary between the donor and acceptor materials, (iii) separation of excitons and charge carrier formation, and (iv) charge transport to electrodes.

Firstly, absorbance depends on the species of the organic materials used and the thickness of the organic layer. Secondly, probability of the arrival of the exciton at the boundary between the donor and acceptor materials depends on the exciton diffusion length and area of the boundary. Thirdly, exciton dissociation efficiency at the boundary between the donor and acceptor materials depends on the energy levels of the donor and acceptor materials. Finally, the carrier transport efficiency depends on the path available to the electrodes involved in charge carrier.

It is difficult to successfully obtain high efficiency at both the second and fourth steps. When the boundary between the donor and acceptor materials is increased, the probability of the arrival of the exciton at the boundary increases; however, the path tends to disappear from the electrodes. For this reason, the ideal microphase separation structure has long been

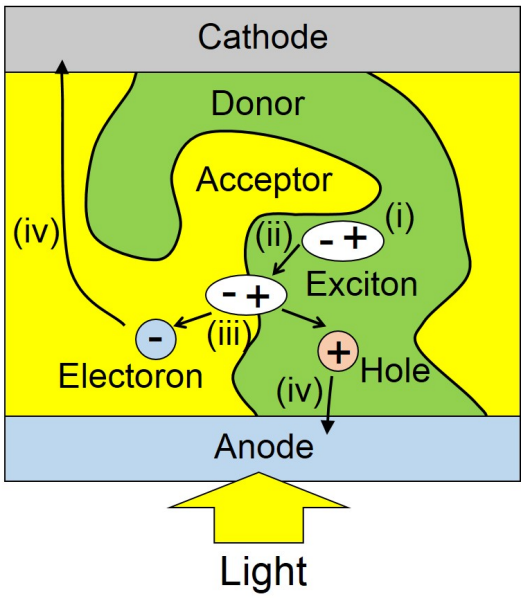

Fig. 1.4 Schematic diagram of the photoelectric conversion process of organic solar cells: (i) light absorption and exciton formation, (ii) diffusion of the generated excitons to the boundary between the donor and acceptor materials, (iii) separation of excitons and charge carrier formation, and (iv) charge transport to electrodes.

studied [47], and the interpenetrating structure of the donor and acceptor materials is regarded as the ideal structure for the organic solar cell [45].

The parameters of solar cells can be described as follows. The typical current density (J)–voltage (V) property of the solar cell is shown in Fig. 1.5. As parameters of the solar cells, open circuit voltage (V_{OC}), short-circuit current density (J_{SC}), fill factor (FF), and energy conversion efficiency (η_e) are usable. V_{OC} depends on the difference between the highest occupied molecular orbital (HOMO) level of the donor material and the lowest unoccupied molecular orbital (LUMO) level of the acceptor material, as well as the difference between the work function of the anode and cathode. J_{SC} is the current density when the voltage is 0 V, and depends on the absorbance, exciton dissociation efficiency, and carrier transport efficiency. FF is the ratio of the maximum power to the multiplication of V_{OC} and J_{SC},

$$FF = \frac{V_{\mathrm{max}} J_{\mathrm{max}}}{V_{\mathrm{OC}} J_{\mathrm{SC}}}, \tag{1.4}$$

where, V_{max} and J_{max} are the voltage and current density at the maximum power point, respectively. FF improves on decreasing the leak current, which is caused by the reverse current and

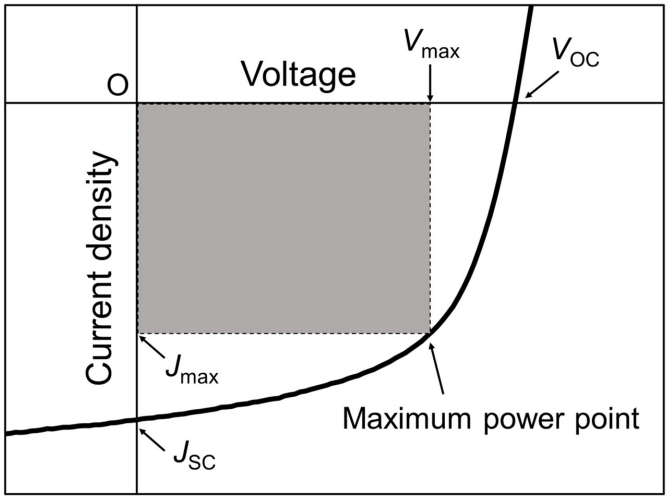

Fig. 1.5 Typical J–V property of the solar cell. The gray area represents the maximum power of the solar cell.

recombination of charge carriers, and resistance of the devices. Parameter η_e is the ratio of the electrical energy generated by the solar cell to the energy of the incident light,

$$\eta_e = \frac{V_{\mathrm{OC}} J_{\mathrm{SC}} FF}{P_{\mathrm{in}}} \times 100\ (\%), \tag{1.5}$$

where, P_{in} is the energy of the incident light per unit time. The power and spectrum of the incident light are determined by the standard test cell conditions, which are 100 mW/cm^2 and spectrum of solar light, respectively.

The external quantum efficiency (EQE) is known as a parameter of solar cells. EQE is represented as the ratio of the number of charge carriers to that of incident photons. EQE is usually measured under monochromatic light irradiation, i.e., EQE represents spectral characteristics.

1.3 X-ray diffraction analysis

1.3.1 Fundamentals of X-ray diffraction

X-ray is a kind of electromagnetic wave, i.e., it exhibits the properties of both wave and particles, similar to light. Thus, X-ray exhibits the diffraction phenomenon, which is one of the properties of waves. The principle of the diffraction phenomenon can be described as follows. When X-ray enters a material, it is scattered by the electrons of the atoms of the materials. This phenomenon is called Thomson scattering. The wavelength of X-ray is almost equal to the distance between

neighboring atoms; therefore, the scattered X-rays can be intensified by the neighboring atoms. Generally, atoms in crystals show regular alignment, and form a periodic structure called crystal lattice. When the atoms are aligned with regularity like crystals, the intensity of the scattered X-rays increases. This phenomenon is called Bragg's diffraction, and the condition for intensifying the scattered X-ray is shown by the following equation, which is called Bragg's laws;

$$2d\sin\theta_B = n\lambda, \tag{1.6}$$

where, d is a lattice interval, θ_B is a diffracted angle, n is an integer and λ is the wavelength of the incident X-ray. Bragg's law can be rewritten in vector representation by using the wave vector of the incident and diffracted X-ray as follows,

$$\boldsymbol{d} \cdot (\boldsymbol{k_2} - \boldsymbol{k_1}) = 2n\pi, \tag{1.7}$$

where, $\boldsymbol{d}$, $\boldsymbol{k_1}$, and $\boldsymbol{k_2}$ are the lattice interval and incident and diffracted X-rays in vector representation, respectively.

Parameter($\boldsymbol{k_2} - \boldsymbol{k_1}$) in Eq. (1.7) is called a scattering vector, and the direction and magnitude of the scattering vector indicate the direction and interval of the reciprocal lattice plane, respectively. The magnitude of $\boldsymbol{k_1}$ is equal to that of $\boldsymbol{k_2}$ because of elastic scattering. Therefore, the X-rays are diffracted under the conditions required for fulfilling a Bragg's diffraction qualification, as shown in Fig. 1.6. The end point of the wave vector of the incident X-ray is the origin of the reciprocal lattice space. The circle in Fig. 1.6 is called Ewald's sphere, the center and radius of which are the start point and magnitude of the wave vector of the incident X-ray, respectively. X-rays are diffracted when the reciprocal lattice points intersect Ewald's sphere.

Diffraction from the atoms can be described as follows. X-rays are scattered by the electrons of atoms, and the number of electron depends on the atomic species, i.e., the intensity of the diffracted X-ray depends on the scattered atomic species. The intensity of the X-rays diffracted from each atom has been studied by taking the distribution of the electrons of atoms and can be represented by the following equation [48],

$$f = \sum_{j=1}^{4} a_j \exp\left(\frac{-b_j \sin^2\theta}{\lambda^2}\right) + c, \tag{1.8}$$

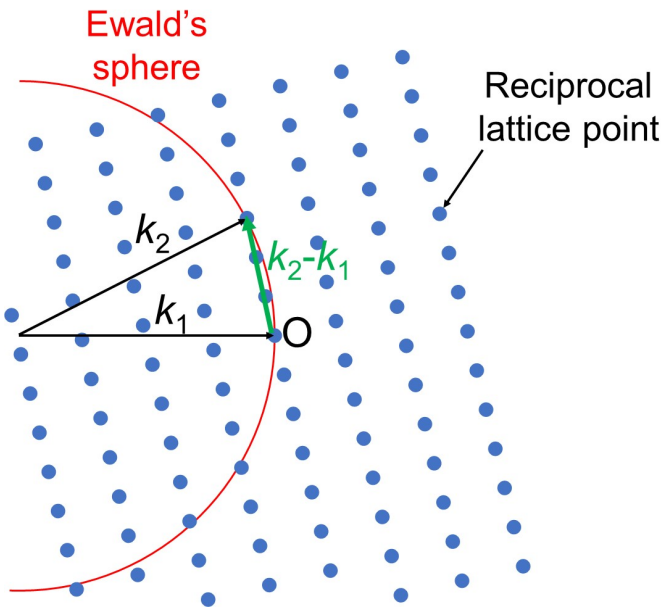

Fig. 1.6 Schematic diagram of incident and diffracted X-rays under the condition fulfilling a Bragg's diffraction qualification. Blue plots, the red circle, and the green arrow represent the reciprocal lattice points, Ewald's sphere, and a scattering vector, respectively.

where, f is the atomic scattering factor, a_j, b_j, and c are the values obtained by theoretical calculations; and the values of hydrogen, carbon, and oxygen atoms are shown in Table 1.1. The theoretical value of a, b, and c are given in the Internal Tables for X-ray Crystallography Vol. 4.

Table 1.1 Theoretical values of a, b, and c in Eq. (1.8).

Element	a_1	b_1	a_2	b_2	a_3	b_3	a_4	b_4	c
1 H	0.494	10.51	0.3229	26.13	0.1401	3.142	0.04081	57.80	0.003038
6 C	2.31	20.84	1.02	10.21	1.589	0.5687	0.865	51.65	0.2156
8 O	3.049	13.28	2.287	5.701	1.546	0.3239	0.867	32.91	0.2508

Now, we consider the diffraction from all atoms in a crystal lattice. The phases of X-rays scattered from each atom in a crystal lattice are different, and they depend on the positions of atoms in a crystal lattice. Therefore, it is important to consider the relationship between the phases of X-rays and positions of atoms.

By considering the diffraction from the (hkl) plane, the phase of the diffracted X-ray can be

described as follows,

$$\phi = 2\pi(hu + kv + lw), \tag{1.9}$$

where, u, v, and w are the coordinates of an atom divided by lattice constants a, b, and c, respectively. The intensity of the scattered X-ray depends on the atomic scattering factor, and the X-rays diffracted from a crystal lattice can be described by summing up the diffraction of all atoms in a crystal lattice as follows,

$$F_{hkl} = \sum_{j=1}^{N} f_j e^{i\phi_j} = \sum_{j=1}^{N} f_j e^{2\pi i(hu_j + kv_j + lw_j)}, \tag{1.10}$$

where, F_{hkl} is called a structure factor that represents the amplitude and phase of the diffracted X-ray, N is the total number of atoms in a crystal lattice, and f_j, ϕ_j, u_j, v_j, and w_j are f, ϕ, u, v, and w of the j th atom, respectively.

Now, we consider diffraction from the crystal. The intensity of the diffracted X-ray is not affected by only the structure factor, but also by polarization, Lorentz-polarization factor, absorption, and temperature factor, and calculated as follows,

$$I = |F|^2 \left(\frac{1 + \cos^2 2\theta}{2\sin^2\theta\cos\theta} \right) \frac{1}{2\mu_{\text{abs}}} e^{-2M}, \tag{1.11}$$

where, I is the intensity of the diffracted X-ray, the second term of Eq. (1.11) is Lorentz-polarization factor, μ_{abs} is an absorption factor, and M is a temperature factor [49]. When the relative intensities from each lattice plane are calculated, the absorption and temperature factors are ignored because of the constant or undecidable values, and the intensity of the diffracted X-ray can be described in simple terms as follows,

$$I \propto |F|^2 \left(\frac{1 + \cos^2 2\theta}{2\sin^2\theta\cos\theta} \right). \tag{1.12}$$

In this dissertation, the relative intensities of the X-rays diffracted from each lattice plane were calculated by using Eq. (1.12.).

1.3.2 Grazing incidence wide-angle X-ray scattering

XRD analysis has long been used to clarify the crystal structures. Generally, a scintillation counter, which is a zero-dimensional detector, is used as a detector of X-rays. The intensities of XRD are plotted against various parameters such as diffraction, tilt, and azimuthal angles using a scintillation counter, and line profiles are obtained. For a sample without an orientational order like powder crystals, all XRD peaks can be detected by measuring the diffracted angle dependence on the XRD intensity. For samples with an orientational order like molecular oriented films or single-crystals, tilt or azimuthal angle dependence on the XRD intensities can be measured at a fixed diffracted angle fulfilling the Bragg's diffraction qualification, and the degree of orientation or molecular alignment direction can be evaluated. The measurement method is called the X-ray rocking curve. However, it is difficult to detect all XRD peaks of a sample with an orientational order by the XRD measurement utilizing a zero-dimensional detector. The reciprocal lattice points of the oriented samples are located three-dimensionally, and the XRD peaks can be detected by two or three-dimensionally moving of the zero-dimensional detector [50]; therefore, it takes too long time to measure.

Recently, XRD analysis utilizing a two-dimensional (2-D) detector has been carried out because of the availability of synchrotron radiation facilities, such as SPring-8, and popularization of semiconductor detectors. XRD analysis utilizing a 2-D detector can afford a 2-D XRD pattern, and it is suitable to measure the sample with an orientational order. The grazing incidence wide-angle X-ray scattering (GIWAXS) technique is one of the methods that uses the 2-D detector. Figure 1.7 shows the schematic of the measurement setup of the GIWAXS technique. The GIWAXS measurement setup consists of an X-ray source, a multi-axis diffractometer, and a 2-D detector. X-rays enter the sample with a nearly zero incident angle, and the diffracted X-rays are detected by the 2-D detector.

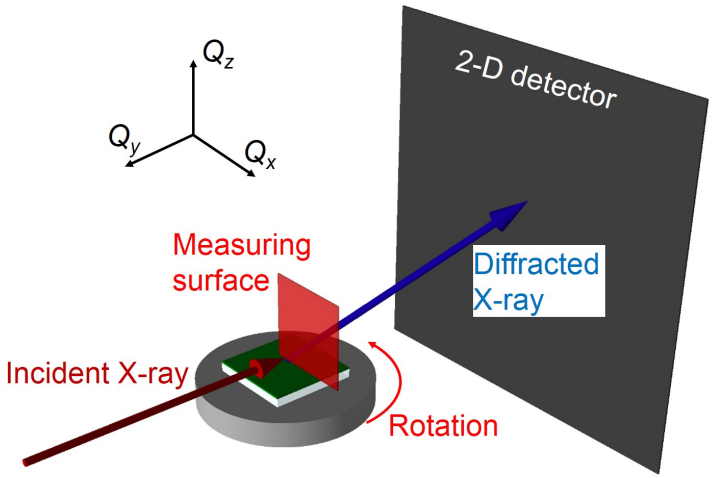

Fig. 1.7 Schematic diagram of the GIWAXS measurement setup. Q_x, Q_y, and Q_z represent coordinates of the reciprocal lattice space.

XRD patterns depend on the periodicity of the sample. The XRD patterns from the samples with various dimensions of periodicities can be described as follows. Figure 1.8 shows the schematics of the reciprocal lattice points of the samples with various dimensions of periodicity, such as powder crystals and molecular oriented films with and without dependence on azimuthal angles. Since the directions of crystal planes in powder crystals are random, the reciprocal lattice points of the powder crystals are spherical as shown in Fig. 1.8(a), and the diffracted X-rays are generated at all directions, fulfilling the Bragg's diffraction qualification. That is, the reciprocal lattice points of powder crystals possess only one parameter of plane intervals. X-rays are diffracted when the reciprocal lattice points intersects Ewald's sphere, and the intersection of two spheres is a circle; therefore, circular XRD patterns are detected on the 2-D detector.

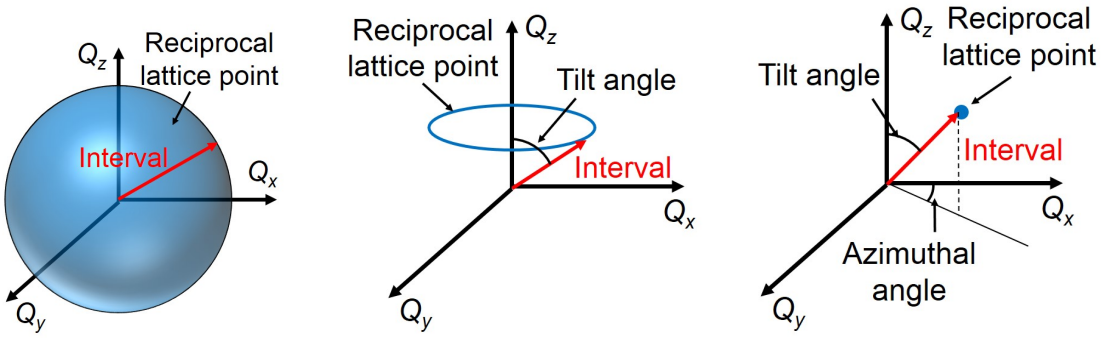

(a) (b) (c)

Fig. 1.8 Schematics of the reciprocal lattice points of the samples with various dimensions of periodicity: (a) powder crystals and molecular oriented films (b) without and (c) with dependence on azimuthal angles.

Molecules in some films prepared by evaporation and spin-coating possess molecular orientation order in the out-of-plane direction; however, there is no molecular order in the azimuthal direction. The reciprocal lattice points are circular because there is no molecular orientation order in the azimuthal direction as shown in Fig. 1.8(b), and the reciprocal lattice points possess two parameters of plane intervals and tilt angles. The intersection of Ewald's sphere and circular lattice points are points; therefore, spotty XRD patterns are detected on the 2-D detector.

In the case of a single-crystal, X-rays are diffracted to specific directions, and the reciprocal lattice points are dotted as shown in Fig. 1.8(c). Reciprocal lattice points possess three parameters of plane intervals, tilt, and azimuthal angles. The three-dimensional information of the reciprocal lattice points cannot be obtained by the 2-D detector, and it is necessary to rotate the sample for detecting the XRD peaks. Therefore, spotty XRD patterns that depend on the sample rotation are detected on the 2-D detector.

1.3.3 Molecular packing structure of discotic liquid crystals

Discotic LC materials tend to form a columnar structure. The intercolumn distance is much longer than the intermolecular distance, and XRD peaks based on the inter-molecular distance are detected at a lower angle than that based on the intercolumn distance. The arrangement of the columns can be determined by taking the XRD peaks based on the intercolumn distance.

The columnar mesophses formed by discotic LC materials can be broadly classified into four categories: oblique, rectangular, tetragonal, and hexagonal phases [51]. That is, the relative

positions of the molecules are oblique, rectangular, tetragonal, and hexagonal, as seen from the column direction, respectively. The rectangular phases can be classified into four categories based on the symmetry: $C2/m$, $P2_1/a$, $P2m$, and $P2/a$. Figure 1.9 shows the schematics of oblique, tetragonal, hexagonal, and four types of rectangular phases. The molecules in the columns are tilted in the case of hexagonal and tetragonal phases, as shown in Figs. 1.9(a), (b), respectively. However, they are not tilted for the oblique and rectangular phases as shown in Figs. 1.9(c)–(g).

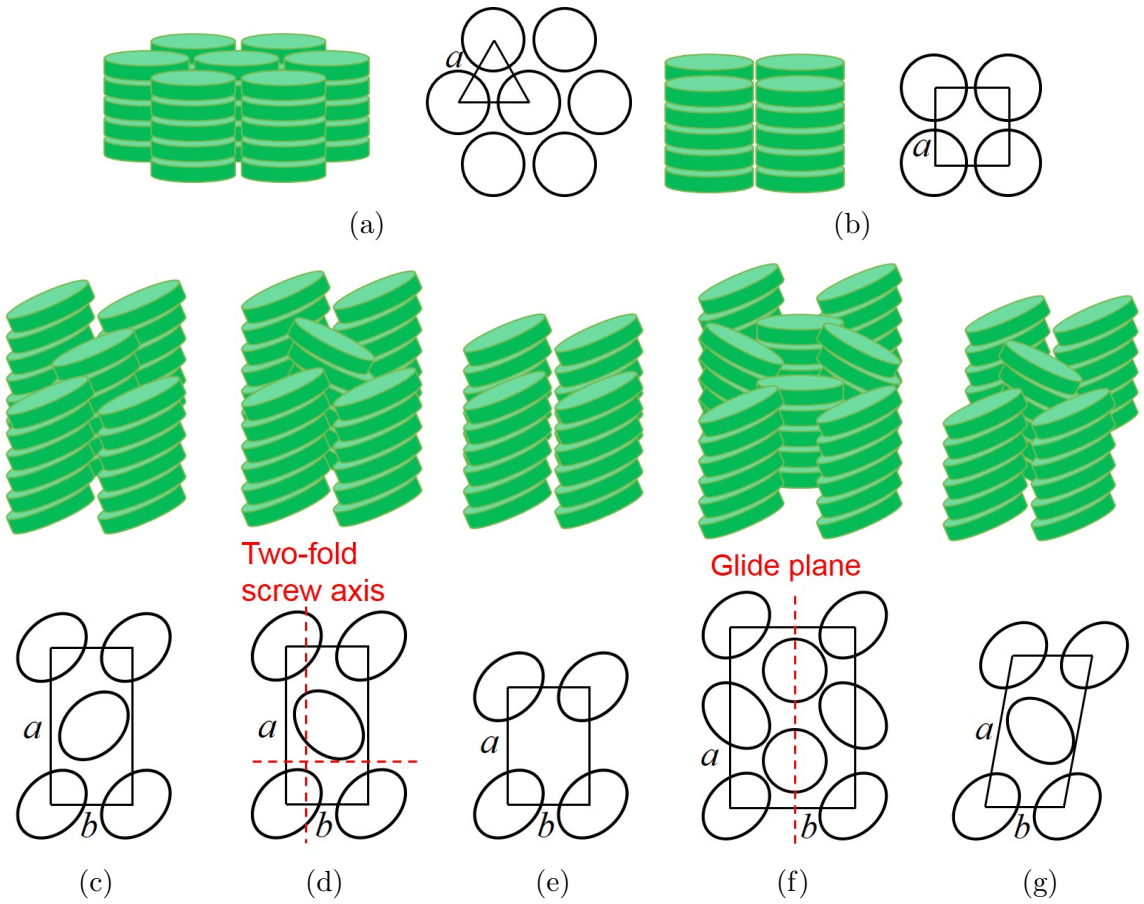

Fig. 1.9 Schematic diagrams of (a) hexagonal, (b) tetragonal, (c)–(f) rectangular, and (g) oblique phases of columnar LC materials. The rectangular phases are classified into four categories by the symmetry: (c) $C2/m$, (d) $P2_1/a$, (e) $P2m$, and (f) $P2/a$.

The hexagonal phase has the highest symmetry in these four phases, and this phase is almost equal to the centered rectangular phase, the ratio of the long and short sides of which is $\sqrt{3}$, as shown in Fig. 1.9(a). The tetragonal phase is almost equal to the rectangular phase, the length of the long side of which is equal to that of the short side, as shown in Fig. 1.9(b). Therefore, the hexagonal and rectangular phases are discussed by considering the rectangular phase.

It has been observed that XRD peaks disappear because of the interference of X-rays, and this is called the extinction rule. The extinction rule depends on the symmetry of the crystal structure. Many XRD peaks disappear in crystals with high symmetry, while all peaks appear in crystals with low symmetry.

The intensity of the diffracted X-rays in the four types of rectangular columnar phases shown in Figs. 1.9(c)–(f) can be calculated by Eq. (1.10). Lattice constant c is determined to be in the molecular stacking direction, and lattice constants a and b are determined to be in the intercolumn direction. In this section, the periodicity of the molecular stacking direction is not considered for simplicity.

In the case of a centered rectangular with the symmetry of $C2/m$, as shown in Fig. 1.9(c), there are two molecules in a unit cell, and the position of the two molecules can be described by $(u,v)=(x,y)$, $(x+1/2,y+1/2)$; therefore, F_{hk} in Eq. (1.10) can be calculated as follows,

$$\begin{aligned} F_{hk} &= f e^{2\pi i(hx+ky)} + f e^{2\pi i\left(hx+ky+\frac{h+k}{2}\right)} \\ &= \left\{1+e^{\pi i(h+k)}\right\} f e^{2\pi i(hx+ky)}, \end{aligned} \tag{1.13}$$

where, f is the scattering factor of a molecule. F_{hkl} is zero when $h+k=2n+1$ (n is an integer), and XRD peaks disappear.

In the case of a centered rectangular with the symmetry of $P2_1/a$, as shown in Fig. 1.9(d), there are two two-fold screw axes along the a and b axes. The two-fold screw axes along the a and b axes can be described as $(x,y) \to (x+1/2,-y)$ and $(x,y) \to (-x,y+1/2)$, respectively; therefore, F_{hk} in Eq. (1.10) can be calculated as follows,

$$\begin{aligned} F_{hk} &= f e^{2\pi i(hx+ky)} + f e^{2\pi i\left(hx-ky+\frac{h}{2}\right)} \\ F_{h0} &= \left(1+e^{\pi ih}\right) f e^{2\pi ihx}, \end{aligned} \tag{1.14}$$

$$\begin{aligned} F_{hk} &= f e^{2\pi i(hx+ky)} + f e^{2\pi i\left(-hx+ky+\frac{k}{2}\right)} \\ F_{0k} &= \left(1+e^{\pi ik}\right) f e^{2\pi iky}, \end{aligned} \tag{1.15}$$

therefore, F_{hkl} is zero when $h=2n+1$ and $k=0$, or $h=0$ and $k=2n+1$, and XRD peaks

disappear.

In the case of a rectangular phase with the symmetry of $P2m$, as shown in Fig. 1.9(e), there is no extinction rule; therefore, all XRD peaks appear. For a rectangular phase with the symmetry of $P2/a$, as shown in Fig. 1.9(f), there is a glide plane along the a axis, and the symmetry can be described as $(x, y) \rightarrow (x + 1/2, -y)$. The result is similar to the result obtained using Eq. (1.14); therefore, XRD peaks disappear when when $h = 2n+1$ and $k = 0$. The symmetry of the rectangular columnar phase can be determined by the extinction rule.

The lattice constant of the rectangular columnar phase can be also determined by the positions of XRD peaks. The plane interval and direction can be determined by the following equations,

$$\frac{1}{d(hk0)} = \frac{h^2}{a^2} + \frac{k^2}{b^2}, \tag{1.16}$$

$$\alpha(hk0) = \tan^{-1}\left(\frac{ka}{hb}\right), \tag{1.17}$$

where, $d(hk0)$ and $\alpha(hk0)$ are the interval and tilt angle, respectively, from the a axis of the lattice plane in the rectangular phase, h and k are Miller indices, and a and b are lattice constants.

1.4 Motivation of the dissertation

A columnar LC material, C6PcH$_2$, exhibits excellent electrical properties such as high carrier mobility and excellent solar cell properties. However, the reported C6PcH$_2$-based devices are fabricated by spin-coating, and control of the molecular orientation in the thin film was not carried out; thus, the excellent electrical properties of these devices have not been used to the fullest. For this reason, the fabrication of a molecular oriented thin film of C6PcH$_2$ is desired. However, even the analysis methods for the molecular packing structure and molecular orientation in such thin films have still not been resolved.

In this dissertation, planar and homeotropic alignments of columnar LC materials in thin films was investigated by using C6PcH$_2$, and the analytical method for the molecular packing structure and molecular alignment in the molecularly oriented thin film are investigated. Moreover, the devices utilizing molecularly oriented thin films were fabricated, and this process of

molecular orientation was shown to be effective for device application.

1.5 Contents of the dissertation

This dissertation is organized in six chapters.

Chapter 1 describes the background, purpose, and overview of this dissertation. The fundamental of X-ray structure analysis were explained.

In Chapter 2, the structures of crystal polymorphisms of discotic LC materials were investigated by single-crystal X-ray structure analysis, and the stability of each crystal is discussed by thermal analysis. The carrier transport properties of each crystal polymorphism are discussed based on the results of the DFT calculation.

In Chapter 3, the molecular packing structure and molecular alignment in the film prepared by spin-coating were investigated by the GIWAXS measurement and discussed by taking the molecular packing structure determined in Chapter 2.

In Chapter 4, uniaxially planar alignment of discotic LC materials in films was induced by bar-coating, and the 3-D molecular packing structure and molecular alignment were investigated by GIWAXS measurement with sample rotation. The XRD patterns were reproduced by a simulation using the molecular packing structure determined in Chapter 2, and a technique for detailed crystal structure analysis in a uniaxial molecularly oriented thin film is proposed. Moreover, homeotropic alignment in thin films was also induced, and the molecular alignment was investigated by the GIWAXS measurement. The fabrication conditions in inducing homeotropic alignment are discussed based on the molecular packing structure in the LC phase.

In Chapter 5, FETs and solar cells utilizing molecularly oriented films prepared by the process shown in Chapter 4 were fabricated, and the device characteristics of FETs and solar cells are discussed based on the carrier transport properties of discotic LC materials.

Chapter 6 concludes this dissertation.

Chapter 2.

Single crystal structure and its thermal behavior

2.1 Introduction

A columnar LC semiconductor, C6PcH$_2$, has been reported to exhibit a high carrier mobility [23], and device applications utilizing C6PcH$_2$ are expected [52]. The high carrier mobility is based on the molecular packing structure of C6PcH$_2$. The molecular packing structure in the LC phase and single-crystal state has been investigated by X-ray structure analysis [23], [27]. However, the diffracted patterns of the reported molecular packing structure are different from those in the thin film of the device structure [28]. Non-substituted Pc has been reported to exhibit crystal polymorphs [29]; C6PcH$_2$ has also been suggested to exhibit crystal polymorphs. However, the detail crystal structure has not been determined.

In this chapter, the single-crystals of C6PcH$_2$ were grown by the recrystallization method under various conditions, and the crystal structures were determined by single-crystal X-ray structure analysis. Moreover, the carrier transport properties were simulated by the density functional theory (DFT) calculation.

The single crystals of the non-peripheral pentyl-substituted phthalocyanine 1,4,8,11,15,18,22,25-octapentyl-phthalocyanine (C5PcH$_2$) and the non-peripheral hexyl-substituted tetrabenzotriazaporphyrin 1,4,8,11,15,18,22,25-octahexyl-tetrabenzotriazaporphyrin (C6TBTAPH$_2$) were also grown by the recrystallization method and their crystal structures were determined. The alkyl-chain length of C5PcH$_2$ is shorter than that of C6PcH$_2$, and the core structure of C6TBTAPH$_2$ is different from that of C6PcH$_2$. The crystal structure of C6PcH$_2$ was discussed based on the crystal structures of C5PcH$_2$ and C6TBTAPH$_2$. The selective crystal growth of the crystal

polymorphs was discussed by considering their thermal behaviors measured by different scanning calorimetry (DSC) and temperature-controlled X-ray structure analysis.

2.2 Sample fabrication

2.2.1 Materials

Molecular structures of $C6PcH_2$, $C5PcH_2$, and $C6TBTAPH_2$ are shown in Fig. 2.1. $C6PcH_2$, $C5PcH_2$, and $C6TBTAPH_2$ were synthesized by a previously reported procedure [53], [54].

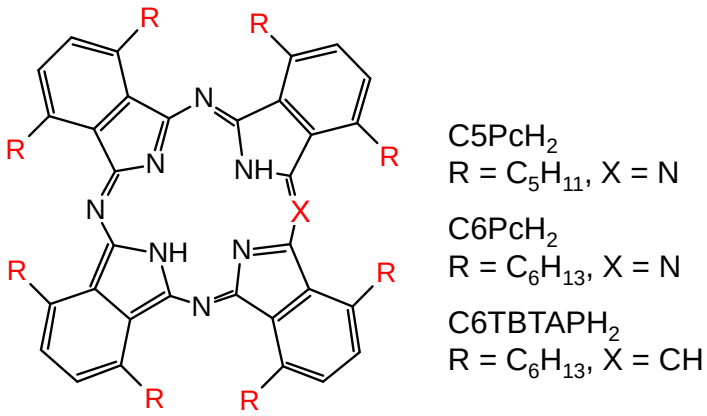

Fig. 2.1 Molecular structures of $C5PcH_2$, $C6PcH_2$, and $C6TBTAPH_2$.

Figure 2.2 shows the phase transition temperatures of $C6PcH_2$, $C5PcH_2$, and $C6TBTAPH_2$, determined by DSC by heating [23], [55], [56]. $C5PcH_2$ did not exhibit the LC phase and its melting point was determined to be 218 °C. $C6PcH_2$ and $C6TBTAPH_2$ exhibit the LC phase from 161 °C to 170 °C and from 151 °C to 170 °C, respectively.

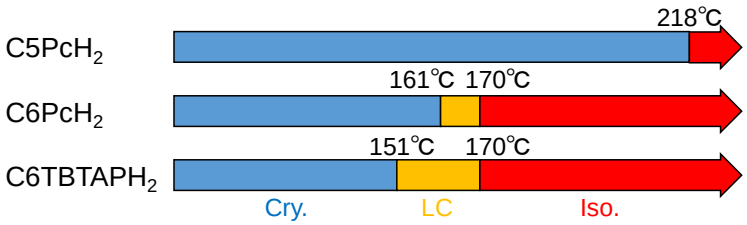

Fig. 2.2 Phase transition temperature of $C5PcH_2$, $C6PcH_2$, and $C6TBTAPH_2$ in the heating process.

2.2.2 Preparation of single crystals

The single crystals were fabricated by two types of recrystallization methods, solvent evaporation technique and slow cooling method.

In the solvent evaporation technique, saturated solutions were prepared in screw-top vials, and the solvents were vaporized for a month at room temperature under atmospheric conditions. A mixed solvent of tetrahydrofuran and acetonitrile was used as a recrystallization solvent.

In the slow cooling method, supersaturated solutions were prepared in screw-top vials at room temperature under atmospheric conditions. The solutions were heated at 333 K and gradually cooled to room temperature over 3 days. A mixed solvent of tetrahydrofuran and ethanol was used as a recrystallization solvent for the $C5PcH_2$. In the other cases, a mixed solvent of tetrahydrofuran and acetonitrile was used. The crystals fabricated by the solvent evaporation technique and slow cooling method were called α and β-type crystals, respectively.

2.2.3 Measurement setups

The shapes of the single crystals were observed by a digital microscope (KEYENCE VHX-1000). The single-crystal X-ray diffraction measurement was carried out by using a curved imaging plate (RIGAKU R-AXIS RAPID-191R) with an X-ray generator (RIGAKU FR-E++ SuperBright and Cu Kα radiation. The crystallographic calculation was performed by using program packages for structure analysis (RIGAKU Crystal Structure 4.1). The crystal structure of β-type $C6PcH_2$ was determined by a direct method (SHELXS-2013), and the other crystal structures were determined by direct method (SIR-2008). $C6PcH_2$ crystals were measured at 273 K. The α-type crystals of $C5PcH_2$ and $C6TBTAPH_2$ were measured at 123 K, and the β-type crystals of $C5PcH_2$ and $C6TBTAPH_2$ were measured at 213 K. The temperature dependence of the lattice constants of single crystals of β-type $C6PcH_2$ were measured in the same way.

The charge transport of organic molecules at room or higher temperature could be described as the hopping transport [30], [31]. The electron hopping rate W_{EH} is estimated using the Marcus model [57],

$$W_{EH} = \frac{V^2}{\hbar}\left(\frac{\pi}{\lambda_s k_B T}\right)^{1/2} \exp\left(-\frac{\lambda_s}{4k_B T}\right), \tag{2.1}$$

where, V is the electronic coupling between the molecules in the dimer, $\hbar$ is Planck's constant, λ_s is the reorganization energy, k_B is Boltzmann's constant, and T is the temperature. Diffusion constant D of charge hopping in the crystals is approximated by the following equation:

$$D = \frac{1}{2n_D} \sum_i d_i^2 W_i P_i, \tag{2.2}$$

where n_D is the spatial dimensionality and d is the center-of-mass distance between the molecules in the dimer; d_i and W_i are d and W_{EH} of a specific hopping pathway i, respectively; and P_i is the hopping probability of the hopping pathway i. P_i is calculated by

$$P_i = \frac{W_i}{\sum_i W_i}, \tag{2.3}$$

The charge mobility μ is estimated using the Einstein relation:

$$\mu = \frac{q}{k_B T} D, \tag{2.4}$$

where, q is the elementary charge. The columnar LC semiconductor exhibits a high carrier mobility along its column axis; therefore, the one-dimensional (1-D) hopping model, which calculates hopping paths along a column axis, is suitable for simulating the carrier transport properties. Assuming the 1-D hopping model, the 1-D mobility μ_{1D} is calculated from the equation (2.1)–(2.4), $n_D = 1$, and $P_i = 1$ [30], [58].

$$\mu_{1D} = \frac{qd^2}{2k_B T} \frac{V^2}{\hbar} \left(\frac{\pi}{\lambda_s k_B T} \right)^{1/2} \exp\left(-\frac{\lambda_s}{4k_B T} \right) \tag{2.5}$$

The values of V were obtained by using the "fragment approach" implemented in the Amsterdam density functional (ADF) package [59]. The calculation was performed using Generalized Gradient Approximation (GGA) and the Perdew-Wang 91 (PW91) functional with triple-zeta Slater-type orbital (STO) basis set with only one set of polarization functions on each atom (TZP).

2.3 Crystal structure of crystal polymorphism

2.3.1 Crystal morphology

Figure 2.3 shows the microscopy images of the α- and β-type crystals of $C5PcH_2$, $C6PcH_2$, and $C6TBTAPH_2$. The crystals of α-type $C6PcH_2$ and $C6TBTAPH_2$ are cuboidal and the other crystals have needle-like shapes. The typical widths of the needle-like crystals are approximately 100 µm and the typical sizes of the cuboidal crystals are approximately 1 mm square. The α-type crystals of $C5PcH_2$ are blue, β-type crystals of $C6PcH_2$ and $C6TBTAPH_2$ are gray, and the other crystals are black. The α-type crystals of $C6PcH_2$ and $C6TBTAPH_2$ and the β-type crystals of $C6PcH_2$ have angular pieces. The angle of the crystals depends on the angle of the crystal plane.

Non-substituted phthalocyanines mainly form two types of crystal polymorphism and the phase transition from the α-type to β-type tend to take place by thermal annealing [29]. Two types of crystal polymorphism exist for $C5PcH_2$, $C6PcH_2$, and $C6TBTAPH_2$.

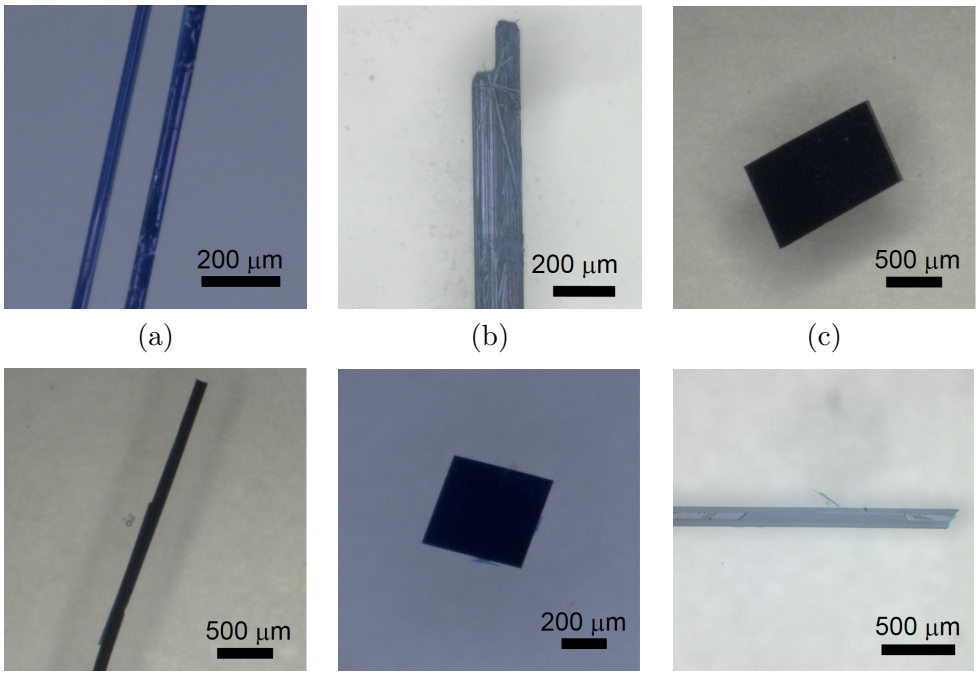

Fig. 2.3 Microscopy images of the crystals. (a) α-type $C5PcH_2$, (b) β-type $C5PcH_2$, (c) α-type $C6PcH_2$, (d) β-type $C6PcH_2$, (e) α-type $C6TBTAPH_2$, and (f) β-type $C6TBTAPH_2$.

2.3.2 Molecular packing structure

Figure 2.4 shows both types of molecular packing structures in the direction parallel and perpendicular to the column axis of $C6PcH_2$, $C5PcH_2$, and $C6TBTAPH_2$, and Tables 2.1 and 2.2 summarize their lattice parameters and crystal and experimental data, where a, b, c, α, β, and γ are the lattice parameters, Z is a number of the molecules present in the unit cell, T is the measured temperature, μ_{abs} is the absorption coefficient, R_F is the reliability factor, and R_W is the radiation weighting factor. The crystal structures of α-type $C6PcH_2$ and $C6TBTAPH_2$ are similar to those reported previously [27], [56].

The normal vectors of the core structure of the α-type compounds used in this section and β-type $C6TBTAPH_2$ are tilted in the same direction, while those of β-type $C5PcH_2$ and $C6PcH_2$ are tilted in an alternate pattern from column to column to give a herringbone-like packing structure.

The crystal structure of α-type $C6TBTAPH_2$ is almost similar to that of α-type $C6PcH_2$. The difference between $C6TBTAPH_2$ and $C6PcH_2$ is in the core structure; therefore, it seems that the core structures are not very effective in determining the basic structure of the α-type crystals. In contrast, the crystal structure of α-type $C5PcH_2$ was different from those of $C6PcH_2$ and $C6TBTAPH_2$; therefore, the difference in the alkyl-substituent length affects the molecular packing structure in the α-type crystals.

The core parts of β-type $C6TBTAPH_2$ are tilted in the same direction, while β-type $C6PcH_2$ and $C5PcH_2$ exhibit a herringbone-like packing structure, and the crystal structure of β-type $C5PcH_2$ resemble that of β-type $C6PcH_2$. These columnar stacks are considered to depend on the symmetry of the core structure. Phthalocyanines have higher symmetries than tetrabenzotriazaporphyrins; therefore, the crystal systems and space groups in β-type $C6PcH_2$ and $C5PcH_2$ have higher symmetries than $C6TBTAPH_2$. These results show that the crystal structures of the β-type crystals are affected by the core structure rather than by the alkyl-substituent length.

The crystal morphologies were simulated by the Bravais Friedel Donnay Harker (BFDH) method by using the single-crystal structures [60]. The simulation was carried out by using the crystal structure visualisation software (Mercury 3.9). The simulated crystal morphologies of α-type $C6PcH_2$ and $C6TBTAPH_2$ are cuboidal, and the other crystals are needle-like. This result is consistent with the microscopy images shown in Fig. 2.3.

The α-type crystals of $C5PcH_2$ grew significantly in the direction of the a axis of its crystal structure, which is parallel to the molecular stacking direction. The β-type crystals of $C5PcH_2$ and $C6PcH_2$ grew significantly in the direction of the b axis, which is also parallel to the molecular stacking direction. The crystal morphologies of β-type $C5PcH_2$ and $C6PcH_2$ were simulated to be hexagonal prisms, because of the high symmetries of the crystal structures. The crystals of β-type $C6TBTAPH_2$ grew significantly in the direction of the a axis, which is also parallel to the molecular stacking direction. The crystal morphology of β-type $C6TBTAPH_2$ was simulated to be a distorted prism, because the symmetry of β-type $C6TBTAPH_2$ is lower than those of β-type $C5PcH_2$ and $C6PcH_2$. The α-type $C6PcH_2$ and $C6TBTAPH_2$ crystals grew in two directions, a and b axes of their crystal structures, because lattice parameter a is almost equal to lattice parameter b. The crystal growth directions of the compounds used in this section were clarified based on the crystal morphology simulations utilizing single crystal structures.

Table 2.1 Lattice parameters in α-type and β-type $C6PcH_2$, $C5PcH_2$, and $C6TBTAPH_2$.

	a (Å)	b (Å)	c (Å)
α-type $C6PcH_2$	9.3149(4)	9.7909(5)	19.9810(14)
β-type $C6PcH_2$	20.7430	9.7984	36.0961
α-type $C5PcH_2$	5.14406(13)	16.7097(4)	18.6864(13)
β-type $C5PcH_2$	19.3788(5)	9.7975(3)	34.289(2)
α-type $C6TBTAPH_2$	9.2558(8)	9.6764(8)	19.9021(16)
β-type $C6TBTAPH_2$	9.64161(17)	22.9419(4)	32.721(2)

	α (deg)	β (deg)	γ (deg)	Z
α-type $C6PcH_2$	100.534(7)	91.084(6)	95.653(7)	1
β-type $C6PcH_2$	90	93.8750	90	4
α-type $C5PcH_2$	92.730(7)	94.415(7)	91.667(7)	1
β-type $C5PcH_2$	90	91.781(7)	90	4
α-type $C6TBTAPH_2$	99.760(7)	91.118(6)	95.409(7)	1
β-type $C6TBTAPH_2$	82.445(6)	85.376(6)	81.577(6)	4

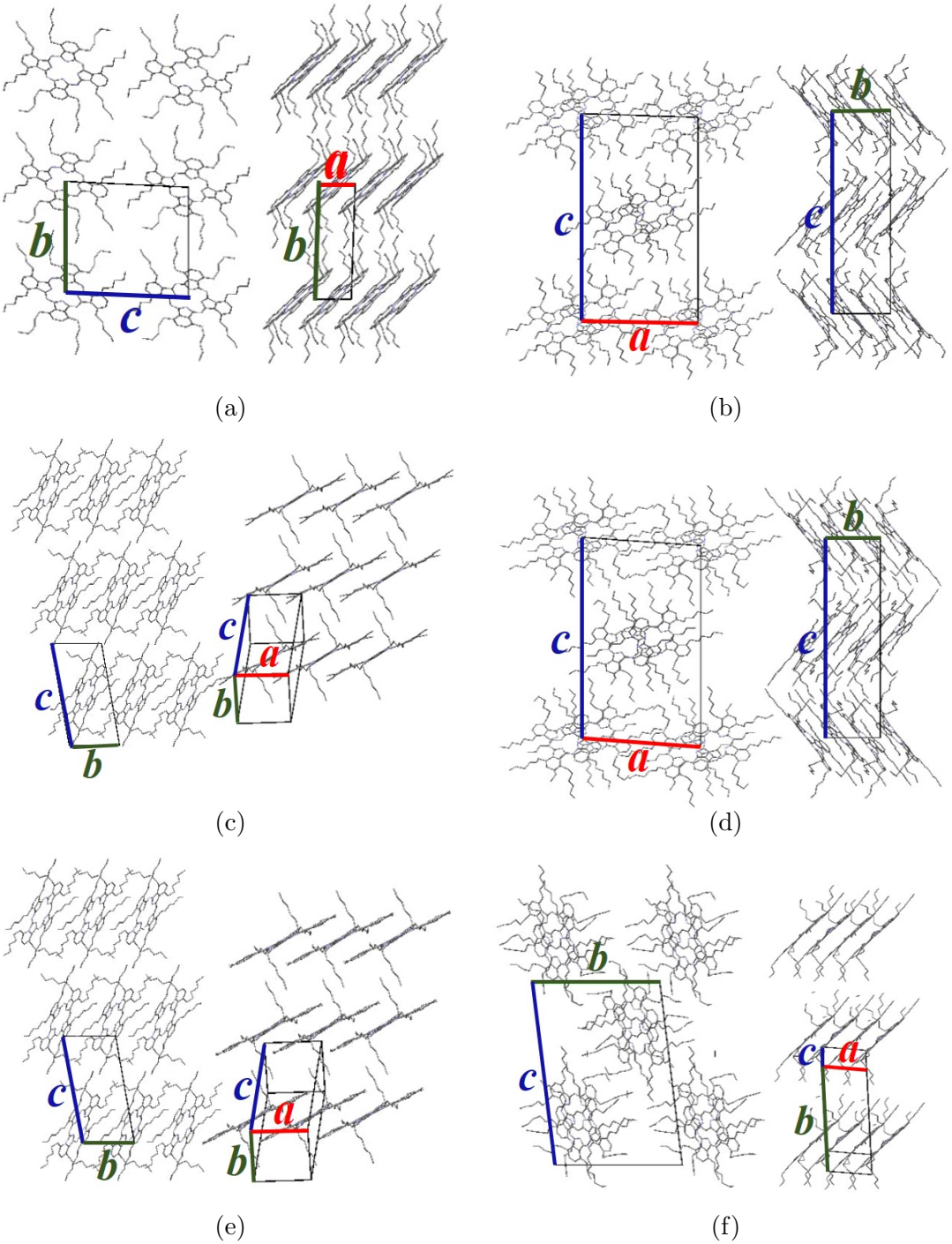

Fig. 2.4 Molecular packing structures of the crystals in the directions parallel and perpendicular to the column axis of (a) α-type $C5PcH_2$, (b) β-type $C5PcH_2$, (c) α-type $C6PcH_2$, (d) β-type $C6PcH_2$, (e) α-type $C6TBTAPH_2$, and (f) β-type $C6TBTAPH_2$

.

Table 2.2 Crystal and experimental data in α-type and β-type $C6PcH_2$, $C5PcH_2$, and $C6TBTAPH_2$.

	Crystal system	Space group	T (K)	μ_{abs}	R_F (%)	R_W (%)
α-type $C6PcH_2$	Triclinic	$P1$	273	0.498	5.78	19.54
β-type $C6PcH_2$	Monoclinic	$P2_1/n$	273	0.473	22.20	47.59
α-type $C5PcH_2$	Triclinic	P-1	123	0.496	14.06	25.70
β-type $C5PcH_2$	Monoclinic	$P2_1/n$	213	0.487	10.90	26.51
α-type $C6TBTAPH_2$	Triclinic	$P1$	123	0.490	9.01	17.61
β-type $C6TBTAPH_2$	Triclinic	P-1	213	0.484	11.39	23.48

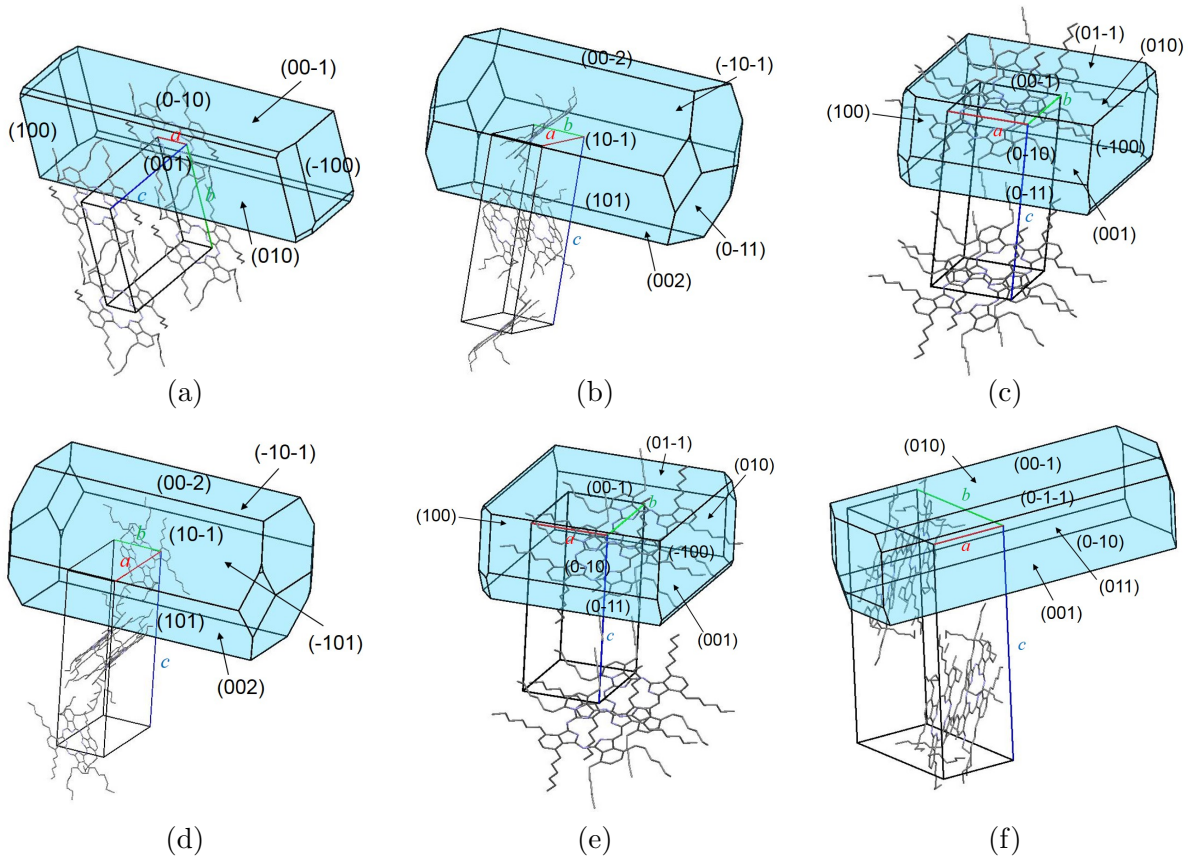

Fig. 2.5 Crystal morphologies and crystal planes simulated by the BFDH method. The crystal planes of the backside of the crystals are indicated by the arrows. (a) α-type $C5PcH_2$, (b) β-type $C5PcH_2$, (c) α-type $C6PcH_2$, (d) β-type $C6PcH_2$, (e) α-type $C6TBTAPH_2$, and (f) β-type $C6TBTAPH_2$.

2.3.3 Calculation of charge transport properties

The hole mobilities of $C5PcH_2$ and $C6PcH_2$ were simulated by the DFT calculation. The hole mobility of $C6TBTAPH_2$ could not be calculated because the position of the carbon atom of

the core structure could not be determined.

For β-type $C5PcH_2$ and $C6PcH_2$ crystals, there are two molecules along the b axis in the unit cell, i.e., there are two paths along the molecular stacking direction. Table 2.3 shows the reorganization energy, λ_s, electronic couplings between the molecules in dimer V, and calculated mobilities μ by using Eq. (2.5). In the case of $C6PcH_2$, the reported values of λ_s, V, and μ were used [58]. The 1-D diffusion constant D_{1D} of β-type $C5PcH_2$ and $C6PcH_2$ can be evaluated by Eq. (2.6) [61], [62].

$$D_{1D} = \frac{1}{2}\left\langle \frac{1}{d_i^2 W_i} \right\rangle^{-1}, \tag{2.6}$$

The 1-D mobility considering two paths was calculated by combining Eqs. (2.2), (2.4), and (2.6) into the following equation,

$$\mu_{1D} = \frac{2\mu_1\mu_2}{\mu_1 + \mu_2}, \tag{2.7}$$

where, μ_1 and μ_2 are the hole mobilities of paths 1 and 2, respectively. The hole mobility of β-type $C5PcH_2$ and $C6PcH_2$ were calculated to be 0.30 and 1.49 cm^2/Vs by Eq. (2.7), respectively. Based on these results, the mobilities of β-type $C6PcH_2$ were calculated to be higher than that of β-type $C5PcH_2$.

The hole mobilities of α-type $C5PcH_2$ and $C6PcH_2$ were calculated to be 7.51 and 11.63 cm^2/Vs, respectively. As mentioned above, the hole mobilities of β-type $C5PcH_2$ and $C6PcH_2$ were calculated to be 0.30 and 1.49 cm^2/Vs, respectively. These results show that for both $C5PcH_2$ and $C6PcH_2$, the hole mobilities of α-type crystals were higher than that of β-type crystals. This result is discussed by taking the shortest intermolecular distance of the Pc core. Generally, electronic couplings between the molecules in the dimer (V) depend on the intermolecular distance, and increase as the distance decrease. The shortest intermolecular distances of α-type $C5PcH_2$ and $C6PcH_2$ were calculated to be 3.418 and 3.511 Å, respectively. On the other hand, those of β-type $C5PcH_2$ were calculated as 3.804 Å (path 1) and 3.681 Å (path2), respectively, and those of β-type $C6PcH_2$ were calculated to be 3.776 Å (path 1) and 3.644 Å (path 2), respectively. The α-type compounds were considered to exhibit higher carrier mobilities than the β-type compounds because of the short intermolecular distance.

The α-type C6PcH$_2$ crystals exhibit a higher carrier mobility than α-type C5PcH$_2$ even though the shortest intermolecular distance of α-type C6PcH$_2$ was longer than that of α-type C5PcH$_2$, which was explained by the center-of-mass distance between the molecules in the dimer. V of α-type C6PcH$_2$ was lower than that of α-type C5PcH$_2$ because of the longer shortest intermolecular distance; however, d of α-type C6PcH$_2$ was longer than that of α-type C5PcH$_2$. High carrier mobility can be obtained in the case of high d by Eq. (2.5). Therefore, the highest mobility can be obtained in the case of α-type C6PcH$_2$.

Table 2.3 λ_s, d, V, and μ of C5PcH$_2$ and C6PcH$_2$ simulated by DFT calculation using single-crystal structures.

	λ_s (eV)	d (Å)	V (eV)	μ (cm^2/Vs)
α-type C5PcH$_2$	8.10×10^{-2}	5.14	7.41×10^{-2}	7.51
β-type C5PcH$_2$ (path 1)	1.11×10^{-1}	7.21	9.30×10^{-3}	0.16
β-type C5PcH$_2$ (path 2)	1.11×10^{-1}	6.92	4.50×10^{-2}	3.38
α-type C6PcH$_2$	6.71×10^{-2}	9.27	4.51×10^{-2}	11.63
β-type C6PcH$_2$ (path 1)	8.8×10^{-2}	7.38	1.80×10^{-2}	0.83
β-type C6PcH$_2$ (path 2)	8.8×10^{-2}	6.89	5.43×10^{-2}	6.63

The carrier mobility perpendicular to the column axis of β-type C6PcH$_2$ was also simulated. The maximum value of the electronic coupling in the hopping path between the molecules in the dimer is $V = 5{\times}10^{-5}$ eV for the inter-column distance, and the center-of-mass distance is d =1.664 nm. As a result, the maximum carrier mobility perpendicular to the column axis is calculated to be $3.8{\times}10^{-5}$ cm^2/Vs by Eq. (2.5). It is noted that the simulated mobility parallel to the column axis is over 10^4 times higher than that perpendicular to the column axis.

2.3.4 Temperature dependence of the lattice constant

The single-crystal X-ray structure measurement was carried out at a lower temperature than room temperature because of decrease in the thermal vibration of molecules. For organic device application, it is important to determine the crystal structure at room temperature, therefore, the temperature dependence of the lattice parameters of β-type C6PcH$_2$ has been investigated.

Figure 2.6 shows the temperature dependences of the lattice parameters in β-type C6PcH$_2$, which confirmed a volumetric change. The lattice parameters of β-type C6PcH$_2$ at 123 K were a = 21.024 Å, b = 9.543 Å, and c = 35.260 Å. With increasing temperature, lattice constant a decreased, while b and c gradually increased. The lattice constants in β-type C6PcH$_2$ at 293 K

were $a = 20.652$ Å, $b = 9.875$ Å, and $c = 36.232$ Å. The volume of the unit cell monotonically increased. The results indicated that there is no phase transition of β-type C6PcH$_2$ from 123 K to 293 K. The b axis of β-type C6PcH$_2$ is parallel to the molecular stacking direction, and lattice constant b increased with increasing temperature. The carrier mobility significantly depends on the intermolecular distance; therefore, the carrier mobility of β-type C6PcH$_2$ is considered to exhibit negative temperature dependence [23].

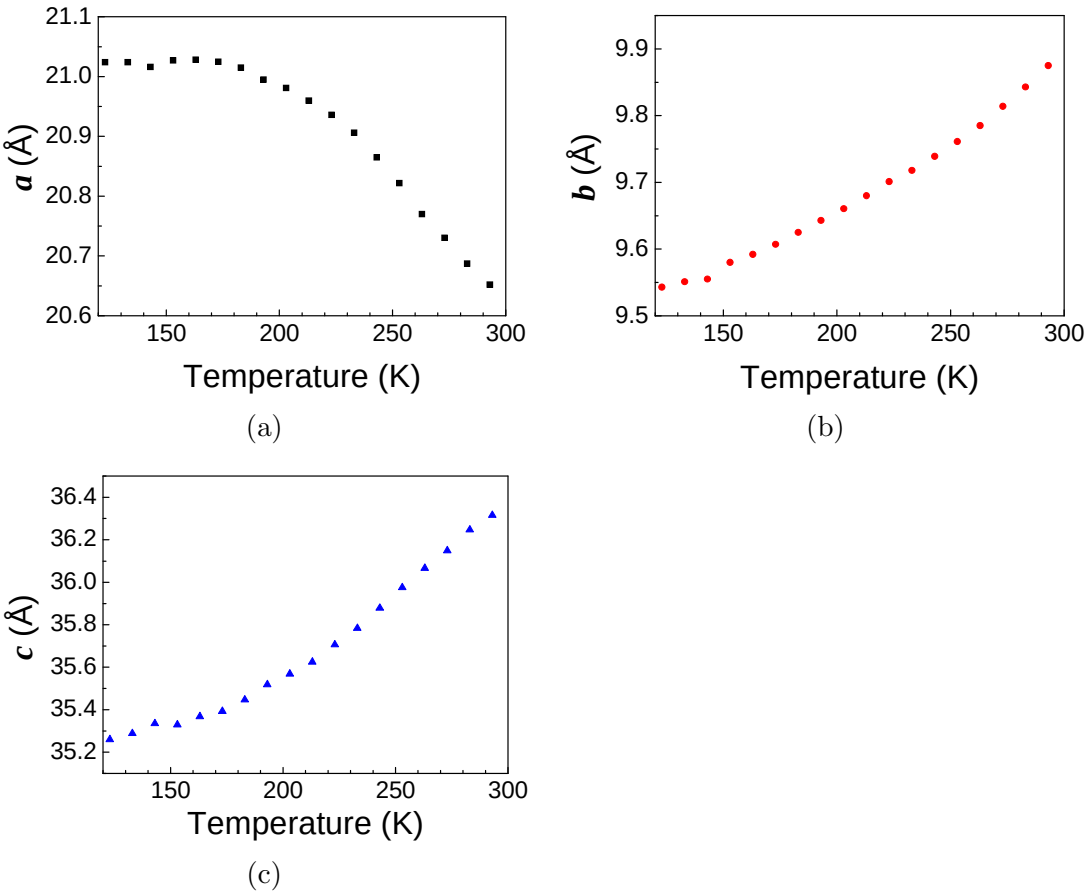

Fig. 2.6 Temperature dependence of lattice constants (a) a, (b) b, and (c) c in β-type C6PcH$_2$ measured by single-crystal X-ray structure analysis.

2.4 Crystal-to-crystal thermal phase transition

2.4.1 Experimental setups

The crystals of α-type C5PcH$_2$, C6PcH$_2$, and C6TBTAPH$_2$ were prepared according to the procedure described in Section 2.2.2 and the thermal phase transitions of the pulverized α-type crystals were observed by using DSC (TA Instruments Q2000) and X-ray diffractometer

(RIGAKU SmartLab) with Cu Kα radiation and a heating stage (Anton-Paar DHS900) at various temperatures under atmospheric pressure conditions. The DSC and XRD measurements were performed at 1 and 5 °C/min, respectively.

The changes of enthalpy ΔH and entropy ΔS were calculated by the following equations,

$$\Delta H = \int C_p dT, \tag{2.8}$$

$$\Delta S = \int \frac{C_p}{T} dT, \tag{2.9}$$

where C_p is the heat capacity and T is the temperature.

2.4.2 Thermal phase transition behavior

Figure 2.7 shows the DSC thermograms of α-type C5PcH$_2$, C6PcH$_2$, and C6TBTAPH$_2$. Table 2.4 shows the peak temperatures T and changes of enthalpy ΔH and entropy ΔS of thermal anomalies shown in Fig. 2.7. ΔH and ΔS were calculated by Eqs. (2.8)–(2.9).

According to the thermal phase transition as shown in Fig. 2.2, the thermal anomalies at 161 °C in Fig. 2.7(b) and 151 °C in Fig. 2.7(c) were based on the transition to the LC phase and the thermal anomalies at 218 °C in Fig. 2.7(a), 170 °C in Fig. 2.7(b), and 171 °C in Fig. 2.7(c) were clearing points. Therefore, the other thermal anomalies were based on the crystal-to-crystal phase transitions. The transition temperature to the LC phase, i.e., the melting point and clearing points of all compounds appeared in both the first and second heating process.

ΔS at the clearing point of C5PcH$_2$, C6PcH$_2$, and C6TBTAPH$_2$ were calculated to be 6.20×10^{-2}, 2.77×10^{-2}, and 1.92×10^{-2} J/gK, respectively. The ΔS value for C5PcH$_2$ is higher than those of C6PcH$_2$ and C6TBTAPH$_2$ since C5PcH$_2$ does not exhibit the LC phase. The total values of ΔS at the melting and clearing points of C6PcH$_2$ and C6TBTAPH$_2$ were calculated to be 6.30×10^{-2} and 5.98×10^{-2} J/gK, respectively. Therefore, the value of ΔS at the clearing point of C5PcH$_2$ was almost equal to the total value of ΔS at the melting and clearing points of the other compounds, i.e., ΔS of the transitions from the crystal to the isotropic phase of all compounds was almost equal.

The DSC thermograms in the first heating process of all compounds were different from

those in the second heating process. The anomaly peak at 181 K in the first heating process of α-type C5PcH$_2$ was shifted to 174 K in the second heating process. The broad peaks at 102 °C in Fig. 2.7(a), 59 and 82 °C in Fig. 2.7(b), and 47 and 81 °C in Fig. 2.7(c) in the first heating process did not reappear in the second heating. The results indicate that the irreversible crystal-to-crystal thermal phase transition occurred, and these thermal anomalies are considered to be based on the irreversible crystal-to-crystal thermal phase transitions.

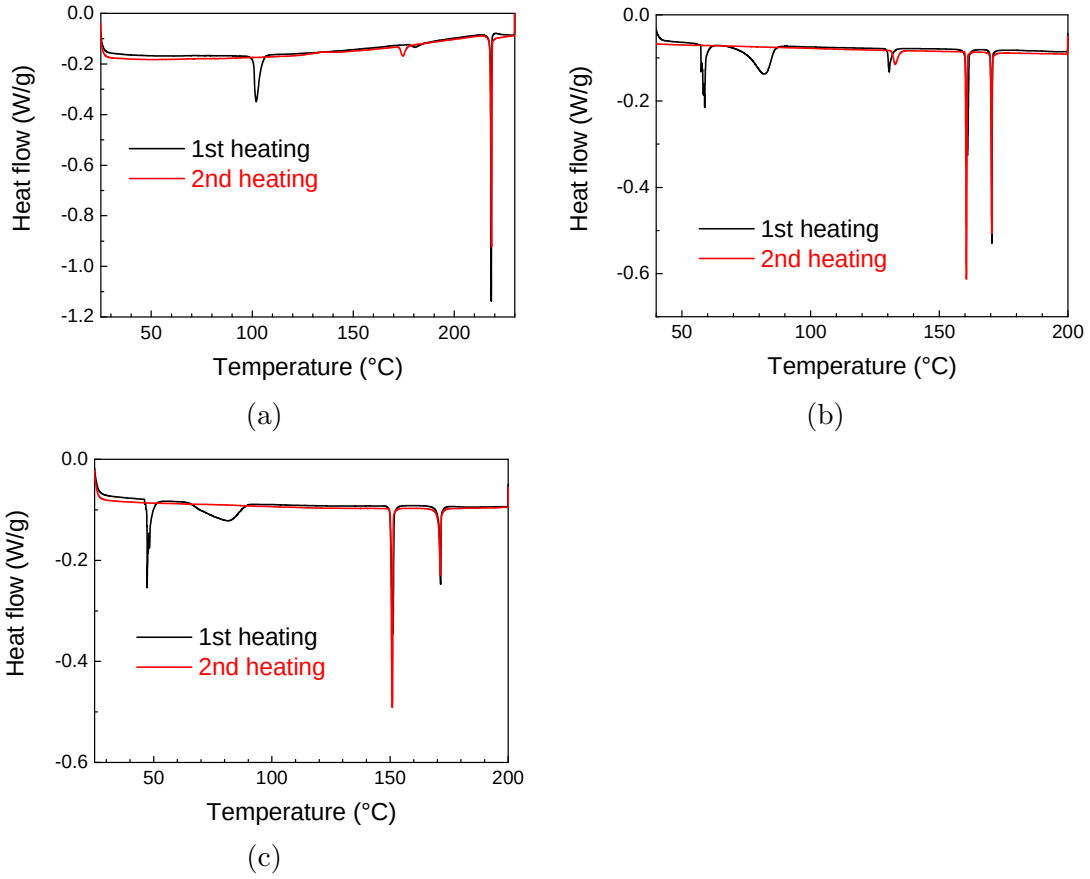

Fig. 2.7 DSC thermograms of α-type (a) C5PcH$_2$, (b) C6PcH$_2$, and (c) C6TBTAPH$_2$. The black and red lines indicate the first and second heating, respectively.

The ΔS values of the irreversible crystal-to-crystal thermal phase transition of C5PcH$_2$, C6PcH$_2$, and C6TBTAPH$_2$ were calculated to be 8.49×10^{-2}, 1.29×10^{-1}, and 1.28×10^{-1} J/gK, respectively, as shown in Table 2.4. The high values of ΔS indicate that the crystal structures of all compounds significantly changed. The ΔS values of C6PcH$_2$ and C6TBTAPH$_2$ were almost equal, and that of C5PcH$_2$ was smaller than those of C6PcH$_2$ and C6TBTAPH$_2$. In a previous research, the entropy of the smectic A–nematic phase transition increased as the alkyl-chain

length increases [63]. The results of this study could be explained by a similar reason, i.e., the irreversible crystal-to-crystal thermal phase transitions were considered to be caused by the melting of the alkyl chains.

Table 2.4 T, ΔH, and ΔS values of thermal anomalies of α-type C5PcH$_2$, C6PcH$_2$, and C6TBTAPH$_2$ in the first and second heating of the DSC measurement.

C5PcH$_2$ 1st heating	T (°C)	102	181	218		
	ΔH (J/g)	31.95	3.91	30.45		
	ΔS (J/gK)	8.49×10^{-2}	8.48×10^{-3}	6.20×10^{-2}		
C5PcH$_2$ 2nd heating	T (°C)	174	218			
	ΔH (J/g)	5.72	30.67			
	ΔS (J/gK)	1.27×10^{-2}	6.24×10^{-2}			
C6PcH$_2$ 1st heating	T (°C)	59	82	130	161	170
	ΔH (J/g)	11.70	33.22	4.53	15.30	12.27
	ΔS (J/gK)	3.53×10^{-2}	9.40×10^{-2}	1.12×10^{-2}	3.53×10^{-2}	2.77×10^{-2}
C6PcH$_2$ 2nd heating	T (°C)	133	161	170		
	ΔH (J/g)	4.09	16.59	12.50		
	ΔS (J/gK)	1.01×10^{-2}	3.83×10^{-2}	2.82×10^{-2}		
C6TBTAPH$_2$ 1st heating	T (°C)	47	81	151	171	
	ΔH (J/g)	12.65	30.97	17.23	8.53	
	ΔS (J/gK)	3.94×10^{-2}	8.80×10^{-2}	4.06×10^{-2}	1.92×10^{-2}	
C6TBTAPH$_2$ 2nd heating	T (°C)	151	171			
	ΔH (J/g)	18.45	8.47			
	ΔS (J/gK)	4.35×10^{-2}	1.91×10^{-2}			

2.4.3 Temperature dependence of crystal structure

Temperature dependences of powder XRD patterns for α-type C5PcH$_2$, C6PcH$_2$, and C6TBTAPH$_2$ in the first heating process are shown in Fig. 2.8. Figure 2.9(a) shows the powder XRD patterns of α and β-type crystals simulated by using the single crystal structure with the crystal structure visualisation software (Mercury 3.9). The lattice spacing $d(hkl)$ was calculated by Bragg's law, as shown in Eq. (1.6).

In the case of C5PcH$_2$ as shown in Fig. 2.8(a), the peak positions of the XRD patterns changed at 110 and 220 °C corresponding the thermal anomalies at 102 and 218 °C measured by the DSC measurement as shown in Table 2.4, respectively. The thermal anomaly at 181 °C is measured by the DSC measurement; however, the change in the diffraction patterns cannot be detected because of the low ΔS of the crystal-to-crystal transition at 181 °C. The XRD peaks at $2\theta = 4.77°$ (18.5 Å), 5.30° (16.7 Å), 7.31° (12.1 Å), and 9.57° (9.3 Å) were detected at room temperature. The peaks correspond to $d(001)$ (18.6 Å), $d(010)$ (16.7 Å), $d(011)$ (12.1 Å), and

d(002) (9.3 Å) of α-type C5PcH$_2$, as shown in Fig. 2.9(a). No peaks, except for pure α-type C5PcH$_2$ crystals, were observed. These pure α-type C5PcH$_2$ crystals were prepared according to the procedure discussed in Section 2.2.2. The XRD peak at $2\theta = 5.22°$ (16.9 Å) was detected at 120 °C. The peak correspond to d(002) (17.1 Å) of β-type C5PcH$_2$, as shown in Fig. 2.9(a). The result indicates that the high and broad thermal anomaly at 102 °C measured by the DSC measurement was based on the phase transitions from α-type to β-type C5PcH$_2$. The broad XRD peak at 2θ = 4.9–5.0° was detected at 220 °C. The peak was observed in spite of the presence of the isotropic phase, and this peak depends on the intercolumn distance. In the isotropic phase, there was no long-distance order; however, a short-distance order structure was formed, and the XRD peaks based on the intercolumn distance was detected.

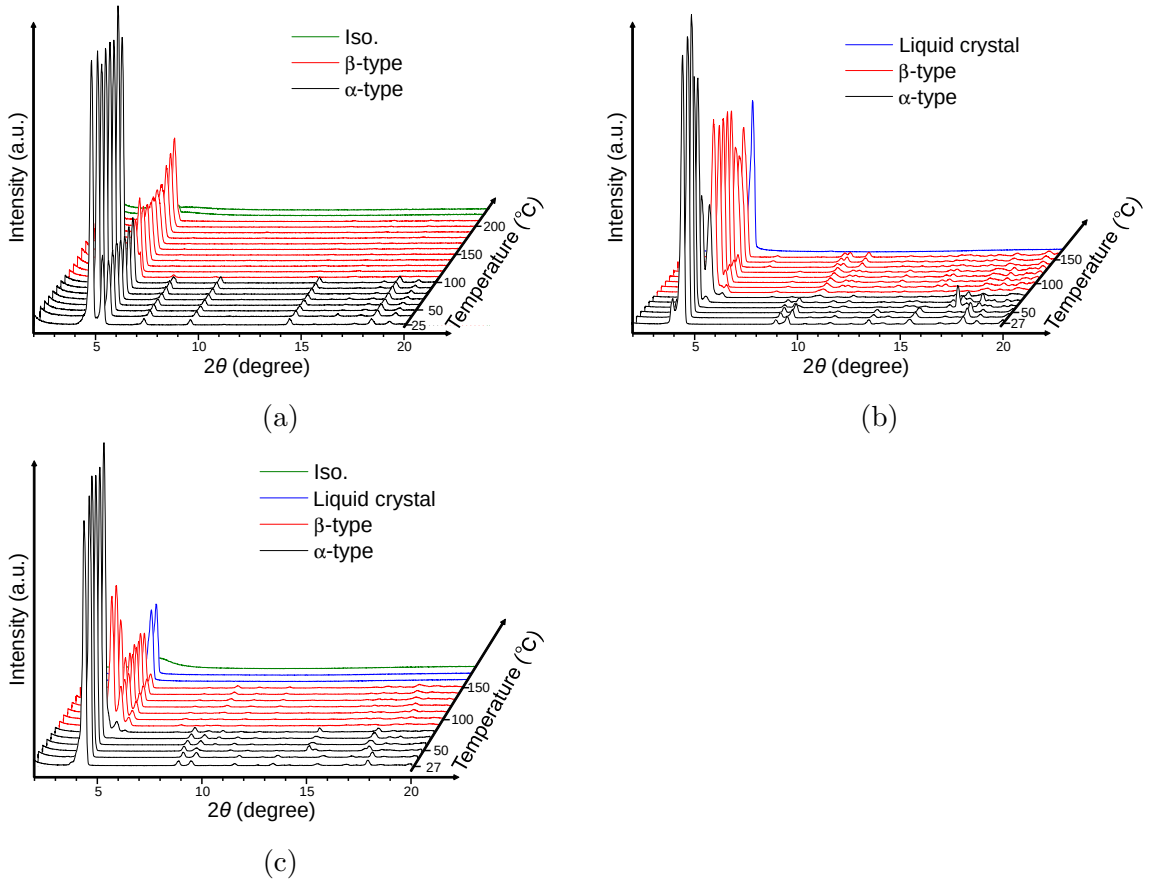

Fig. 2.8 Temperature dependence of powder XRD patterns for α-type crystals of (a) C5PcH$_2$, (b) C6PcH$_2$, and (c) C6TBTAPH$_2$.

In the case of C6PcH$_2$, as shown in Fig. 2.8(b), the XRD patterns changed at 60, 100, and 170 °C, corresponding the thermal anomalies at 59, 82, and 161 °C determined by the DSC

measurement as shown in Table 2.4, respectively. The change in the diffraction patterns cannot be detected because of the low ΔS of the crystal-to-crystal transition at 130 °C. The XRD peaks at $2\theta = 4.47°$ (19.7 Å), 8.98° (9.8 Å), and 9.51° (9.3 Å) were detected at room temperature. The peaks corresponded to $d(001)$ (19.6 Å), $d(002)$ (9.8 Å), and $d(01\bar{1})$ (9.3 Å) of α-type C6PcH$_2$, as shown in Fig. 2.9(a). The small peak at $2\theta = 4.00°$ was considered to be based on the diffraction of $d(001)$ by the Cu Kβ line. The XRD peaks at $2\theta = 4.47°$ shifted to $2\theta = 4.38°$ (20.2 Å) at 60 °C. The XRD patterns first gradually changed in the temperature range of 70–90 °C, and then the XRD peaks at $2\theta = 4.79°$ (18.4 Å) and 5.07° (17.4 Å) were detected at 100 °C. These peaks correspond to $d(002)$ and $d(101)$ of β-type C6PcH$_2$ as shown in Fig. 2.9(a), respectively. The result indicates that the broad thermal anomalies at 59 and 82 °C measured by the DSC measurement depend on the phase transitions from α-type to β-type C6PcH$_2$. The XRD peak at $2\theta = 4.98°$ (17.7 Å) was detected at 170 °C in the LC phase. The peak was considered to correspond to $d(001)$ of the hexagonal columnar mesophase and the intercolumn distance was calculated to be 20.4 Å, which was consistent with the reported value [23].

In the case of C6TBTAPH$_2$, as shown in Fig. 2.8(c), the XRD patterns changed at 60, 100, 160, and 180 °C corresponding the thermal anomalies at 47, 81, 151, and 171 °C determined by the DSC measurement as shown in Table 2.4, respectively. The XRD peaks at $2\theta = 4.41°$ (20.0 Å), 8.91° (9.9 Å), and 9.52° (9.3 Å) were detected at room temperature. The peaks corresponded to $d(001)$ (19.6 Å), $d(002)$ (9.8 Å), and $d(01\bar{1})$ (9.2 Å) of α-type C6TBTAPH$_2$, as shown in Fig. 2.9(a). The XRD peak at $2\theta = 4.41°$ shifted to $2\theta = 4.30°$ at 60 °C. The XRD patterns gradually changed in the temperature range of 70–90 °C and the XRD peaks at $2\theta = 4.52°$ (19.5 Å), 4.92° (17.9 Å), and 5.27° (16.7 Å) were detected at 100 °C. The peaks corresponded to $d(011)$ (19.6 Å), $d(01\bar{1})$ (17.5 Å), and $d(002)$ (16.2 Å) of β-type C6TBTAPH$_2$, as shown in Fig. 2.9(a), respectively. The result indicates that the broad thermal anomalies at 47 and 81 °C determined by the DSC measurement depend on the phase transitions from α-type to β-type C6TBTAPH$_2$. The XRD peak at $2\theta = 4.96°$ (17.8 Å) was detected at 160 °C in the LC phase. The peak was considered to correspond to $d(001)$ of the hexagonal columnar mesophase and the intercolumn distance was calculated 20.6 Å. In the LC phase, C6TBTAPH$_2$ was reported to form a pseudo-disordered hexagonal columnar mesophase with a column interval of 21 Å [26]; therefore, the measured intercolumn distance was consistent with the reported value. The broad XRD peak at $2\theta = 4.9°$ (18.0 Å) was detected at 180 °C in the isotropic phase.

Thus, the thermal phase transitions from α-type to β-type $C5PcH_2$, $C6PcH_2$, and $C6TBTAPH_2$ were observed at 110, 100, and 100 °C, respectively. The pulverized α-type crystals of $C5PcH_2$, $C6PcH_2$, and $C6TBTAPH_2$ were heated at 130, 100, and 100 °C, respectively, and then cooled to room temperature. Both heating and cooling rates were 5 °C/min. The powder XRD patterns before and after the crystal-to-crystal thermal phase transition are shown in Fig. 2.9(b). In all cases of $C5PcH_2$, $C6PcH_2$, and $C6TBTAPH_2$, the powder XRD patterns after heating over the thermal phase transition temperature were almost equal to the simulated XRD patterns obtained by using β-type single-crystal structure crystals. Therefore, the phase transitions from the α-type to β-type crystals were found to be irreversible, i.e., the thermal phase transition from β-type to α-type was never observed by a temperature change.

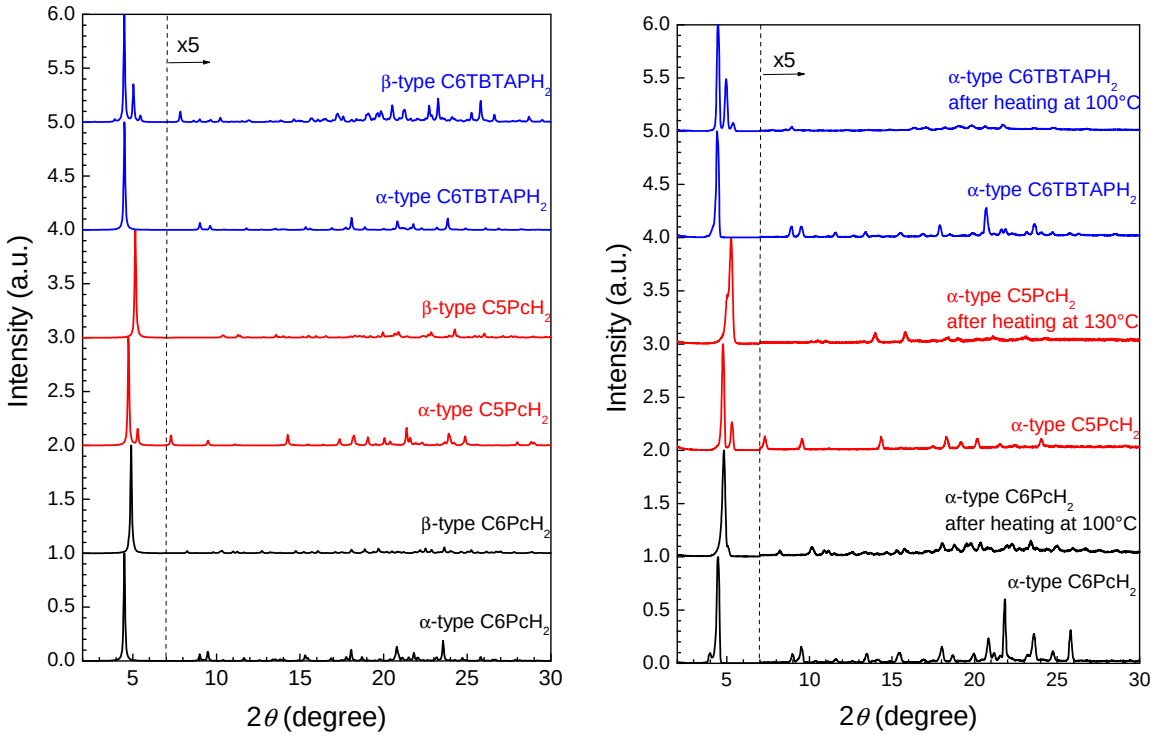

Fig. 2.9 (a) Simulated powder XRD patterns of α- and β-type crystals utillizing single-crystal structure. (b) Measured powder XRD patterns before and after the crystal-to-crystal thermal phase transition.

2.5 Discussion

The phase transition from α-type to β-type is discussed by considering the alkyl-substituent distribution. The thermal ellipsoid plots of α- and β-type C6PcH$_2$ are shown in Fig. 2.10 by using the single crystal structures of α-type and β-type C6PcH$_2$ at 0 °C. The calculation was carried out by using the crystal structure visualization software (Mercury 3.6). The ellipsoids represent the existence probability of atoms with 50% possibility. The alkyl-chain distribution of α-type C6PcH$_2$ was narrower than that of the β-type one, i.e., β-type C6PcH$_2$ was crystallized with a disordered alkyl-chain packing. Therefore, the phase transition from α-type to β-type C6PcH$_2$ should be reasonable, because the motions of the alkyl chains increased as the temperature increased. The α-type and β-type crystals were prepared by the solvent evaporation technique and slow cooling method, respectively. In the solvent evaporation technique, the crystals were prepared at room temperature, while in the slow cooling method, the crystals were prepared at a higher temperature than room temperature.

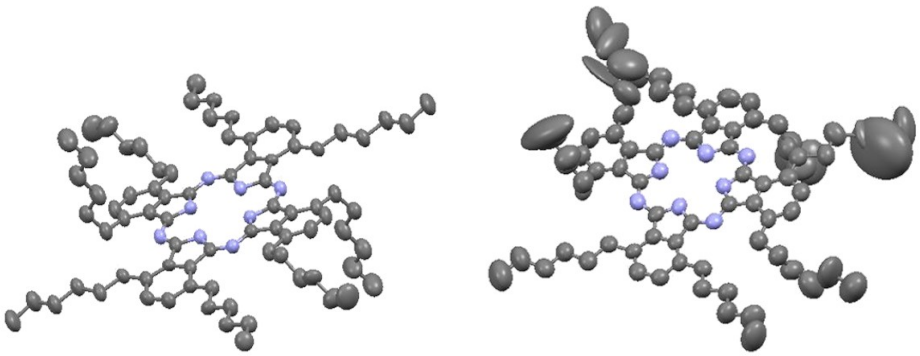

(a) (b)

Fig. 2.10 Thermal ellipsoid plots derived from single-crystal X-ray diffraction data (a) α-type C6PcH$_2$ and (b) β-type C6PcH$_2$ (50% probability ellipsoids).

The selective crystal growth is discussed by using Gibbs' free energy. The change in the Gibbs' free energy ΔG was calculated by the following equations,

$$\Delta G = \Delta H - T\Delta S, \tag{2.10}$$

The change in the Gibbs' free energy of phase transition from the β-type to α-type crystals was

calculated by the following equations,

$$\Delta G_{\beta\to\alpha}(T_1) = \Delta H_{\beta\to\alpha}(T_1) - T_1\Delta S_{\beta\to\alpha}(T_1), \tag{2.11}$$

where, $\Delta G_{\beta\to\alpha}(T_1)$, $\Delta H_{\beta\to\alpha}(T_1)$, and $\Delta S_{\beta\to\alpha}(T_1)$ were determined to be the difference between G, H, and S of the α-type and β-type crystals at temperature T_1, which was less than the phase transition temperature from α-type to β-type crystals T_2. $\Delta H_{\beta\to\alpha}(T_1)$ and $\Delta S_{\beta\to\alpha}(T_1)$ were calculated by Eqs. (2.8) and (2.9).

$$\Delta H_{\beta\to\alpha}(T_1) = \int_{T_1}^{T_2} C_\beta(T)dT - \Delta H_{\alpha\to\beta} + \int_{T_2}^{T_1} C_\alpha(T)dT, \tag{2.12}$$

$$\Delta S_{\beta\to\alpha}(T_1) = \int_{T_1}^{T_2} \frac{C_\beta(T)}{T}dT - \Delta S_{\alpha\to\beta} + \int_{T_2}^{T_1} \frac{C_\alpha(T)}{T}dT. \tag{2.13}$$

Here, $\Delta H_{\alpha\to\beta}$ and $\Delta S_{\alpha\to\beta}$ are the change in the enthalpy and entropy of the phase transition from α-type to β-type crystals, respectively. $C_\alpha(T)$ and $C_\beta(T)$ are the heat capacities of the α-type and β-type crystals, respectively. Therefore, $\Delta G_{\beta\to\alpha}(T_1)$ was calculated to be

$$\Delta G_{\beta\to\alpha}(T_1) = \int_{T_1}^{T_2} \frac{T - T_1}{T}(C_\beta(T) - C_\alpha(T))dT - \Delta H_{\alpha\to\beta} + T_1\Delta S_{\alpha\to\beta} \tag{2.14}$$

In the case of C5PcH$_2$, T_2, $\Delta H_{\alpha\to\beta}$, and $\Delta S_{\alpha\to\beta}$ were 102 °C, 31.95 J/g, and 8.49×10^{-2} J/gK, respectively, as shown in Table 2.4. $C_\beta(T) - C_\alpha(T)$ was calculated by using Fig. 2.7(a). Figure 2.11 shows the temperature dependence of $\Delta G_{\beta\to\alpha}$ of C5PcH$_2$. $\Delta G_{\beta\to\alpha}$ <0 indicates that the phase transition from β-type to α-type C5PcH$_2$ occurs spontaneously. $\Delta G_{\beta\to\alpha}$ was minimum at 56 °C, i.e., the phase transition from β-type to α-type can be considered to occur easily at this temperature. However, the phase transition from β-type to α-type can be not observed in actuality. The crystal structure of α-type C5PcH$_2$ is completely different from that of β-type C5PcH$_2$; thus, the activation energy of the phase transition is considered to be high. The high activation energy is believed to prevent the phase transition from β-type to α-type C5PcH$_2$.

In the case of C6PcH$_2$, T_2, $\Delta H_{\alpha\to\beta}$, and $\Delta S_{\alpha\to\beta}$ were 82 °C, 44.92 J/g, and 1.29×10^{-1} J/gK, respectively, as shown in Table 2.4. $C_\beta(50) - C_\alpha(50)$ was calculated to be 3.5×10^{-1} J/g as shown in Fig. 2.7(b), and the value of $C_\beta(T) - C_\alpha(T)$ was assumed to be 3.5×10^{-1} J/g

in all temperature ranges. Figure 2.11 shows the temperature dependence of $\Delta G_{\beta\to\alpha}$. $\Delta G_{\beta\to\alpha}$ of C6PcH$_2$ decrease as the temperature decrease; therefore, α-type C6PcH$_2$ is a stable state at room temperature and the α-type crystals were selectively prepared at room temperature. The value of $\Delta G_{\beta\to\alpha}$ was negative at room temperature; thus, the phase transition from β-type to α-type crystals occurs easily at room temperature. However, in actuality, the phase transition from α-type to β-type C6PcH$_2$ was irreversible because of the high activation energy.

In the case of C6TBTAPH$_2$, T_2, $\Delta H_{\alpha\to\beta}$, and $\Delta S_{\alpha\to\beta}$ were 81 °C, 43.62 J/g, and 1.29×10^{-1} J/gK, respectively, as shown in Table 2.4. $C_\beta(40) - C_\alpha(40)$ was calculated to be 4.5×10^{-1} J/g as shown in Fig. 2.7(c), and the value of $C_\beta(T) - C_\alpha(T)$ was assumed to be 4.5×10^{-1} J/g in all temperature ranges. Figure 2.11 shows the temperature dependence of $\Delta G_{\beta\to\alpha}$. $\Delta G_{\beta\to\alpha}$ of C6TBTAPH$_2$ decrease as the temperature decreases; therefore, α-type C6TBTAPH$_2$ was stable at room temperature and the α-type crystals were selectively prepared at room temperature.

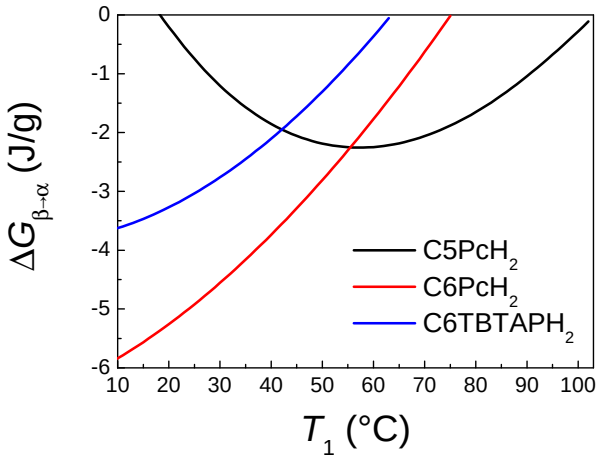

Fig. 2.11 Changes in the Gibbs' free energies of the phase transition from β-type to α-type crystals of C5PcH$_2$, C6PcH$_2$, and C6TBTAPH$_2$ as a function of temperature.

The α-type crystals of C6PcH$_2$ were stable at room temperature. However, the α-type crystals of C6PcH$_2$ have been reported to form in the limited fabricating conditions, such as the solvent vapor treatment [64] and solvent evaporation technique, i.e., slow crystal growth from the solution at room temperature. In contrast, β-type crystals of C6PcH$_2$ were formed by other fabrication processes in spite of the metastable state at room temperature. Specifically, the β-type crystals were formed by phase transition from the LC phase. The sandwich-cell structure is used in the TOF measurement, and the organic semiconductors were injected into

the sandwich-cell at the temperature of the isotropic phase; thus, the carrier mobility of β-type crystals was measured by the TOF measurement. Additionally, the β-type crystals were formed by spin-coating. Thin films of all reported C6PcH$_2$-based solar cells were prepared by spin-coating; thus, the solar cell properties of the β-type C6PcH$_2$-based solar cell were investigated. Therefore, the carrier transport and solar cell properties of α-type crystals of C6PcH$_2$ were not clarified. The mobilities of α- and β-type C6PcH$_2$ were simulated to be 11.63 and 1.486 cm^2/Vs, respectively, i.e., the α-type crystals of C6PcH$_2$ exhibit a higher carrier mobility than the β-type ones. For this reason, the device utilizing the α-type crystals of C6PcH$_2$ is predicted to show high performance. The thin film of the α-type crystals of C6PcH$_2$ has been reported to be fabricated by vapor treatment [64], and the development of transistor devices is now in progress.

As mentioned above, the fabrication conditions of the α-type crystals of C6PcH$_2$ were limited to the slow crystal growth from the solution at room temperature. For rapid crystal growth, the alkyl-chains of C6PcH$_2$ should be fixed as a disordered state, i.e., β-type crystals. However, for slow crystal growth, the alkyl-chains should be fixed as an ordered state, i.e., α-type crystals. Both the α- and β-type crystals of C6PcH$_2$ can exist at room temperature as shown in Fig. 2.8(b). Therefore, the α-type crystals of C6PcH$_2$ can be fabricated only under the conditions of low distribution of alkyl-chains similar to slow crystal growth from the solution at room temperature.

2.6 Conclusions

In this chapter, crystal structures of C5PcH$_2$, C6PcH$_2$, and C6TBTAPH$_2$ were investigated by using single-crystals. Two types of crystals, α- and β-type crystals, were fabricated by the solvent evaporation technique and slow cooling method, respectively, and the crystal structures were clarified by single-crystal X-ray structure analysis. The crystal structures of the α-type crystals were affected by the alkyl-substituent length, while those of the β-type crystals were affected by the core structure. The hole mobilities of C5PcH$_2$ and C6PcH$_2$ were simulated by the DFT calculation. The α-type crystals exhibit a higher hole mobility than the β-type ones; therefore, high device performance can be predicted by using the α-type crystals.

Thermal phase transitions from the α-type to β-type crystals were observed by DSC and temperature-controlled XRD measurements, and the thermal phase was revealed to be irre-

versible. The phase transitions from α-type to β-type were caused by increasing the alkyl-substituent distribution. Additionally, the thermal stability of the polymorphs was discussed by taking the Gibbs' free energy into consideration, and the condition of the selective crystal growth of the polymorphs was clarified.

Chapter 3.

Molecular packing structure in spin-coated thin film

3.1 Introduction

The columnar liquid crystalline (LC) semiconductor, C6PcH$_2$ tends to form a columnar structure. High carrier mobility along the column axis has been reported using the time-of-flight measurement [23]. Electrical devices utilizing C6PcH$_2$ have been studied, and C6PcH$_2$-based solar cells have been reported to exhibit a high power conversion efficiency of 4.2% [25]. For solar cell applications, high carrier transport properties along a direction perpendicular to the substrate is desired, because homeotropic alignment of C6PcH$_2$ molecules enhance the device properties. However, the reported C6PcH$_2$-based solar cells have been fabricated by spin-coating; control of the molecular alignment in thin films has not yet been carried out. Moreover, the molecular packing structure of C6PcH$_2$ in spin-coated films have not been clarified.

C6PcH$_2$ is a columnar LC semiconductor, and the molecules in the spin-coated films are believed to orientate. As discussed in Section 1.3.2, the two-dimensional (2-D) detector is effective for measuring the molecular packing structure in the oriented thin film. In this chapter, the molecular packing structure and molecular alignment of C6PcH$_2$ in a spin-coated thin film are discussed based on the grazing incidence wide-angle X-ray scattering (GIWAXS) technique. The details of the molecular packing structure are determined by comparing the molecular packing structure in the spin-coated film and molecular packing structure obtained by the single-crystal X-ray structure analysis as discussed in Chapter 2. In addition to C6PcH$_2$, the molecular packing structures of C5PcH$_2$ and 1,4,8,11,15,18,22,25-octadecyl-phthalocyanine (C10PcH$_2$) in spin-coated thin films were also investigated by the GIWAXS technique.

3.2 Experimental setups

3.2.1 Sample preparation and measurement setup

Molecular structures of $C5PcH_2$, $C6PcH_2$, and $C10PcH_2$ are shown in Fig. 3.1. $C5PcH_2$, $C6PcH_2$, and $C10PcH_2$ were synthesized by a previously reported procedure [53].

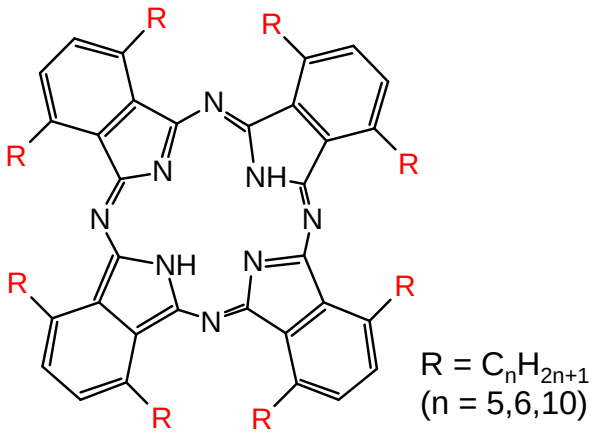

Fig. 3.1 Molecular structures of $C5PcH_2$, $C6PcH_2$, and $C10PcH_2$.

The spin-coated thin films of $C5PcH_2$, $C6PcH_2$, and $C10PcH_2$ were fabricated in the fol-lowing manner. Quartz substrates were cleaned with water, chloroform, acetone, and isopropyl alcohol by ultrasonication and then subjected to UV-ozone treatment. The solutions of $C5PcH_2$, $C6PcH_2$, and $C10PcH_2$ were prepared in accordance with Table 3.1, and the solutions were spin-coated onto substrates at 500 rpm for 60 s in a glove-box filled with nitrogen gas. The thickness of the $C5PcH_2$, $C6PcH_2$, and $C10PcH_2$ films were estimated to be approximately 90 nm, 100 nm, and 100 nm from the absorbance obtained by using a spectrophotometer (Shimadzu UV-3150), respectively.

Table 3.1 Experimental conditions of the solutions of $C5PcH_2$, $C6PcH_2$, and $C10PcH_2$.

Solute	Solvent	Concentration (g/L)
$C5PcH_2$	Toluene	10.6
$C6PcH_2$	Trichloroethylene	12.0
$C10PcH_2$	Chloroform	8.0

The molecular packing structure of C10PcH$_2$ was determined by the powder XRD measurement. The sample was fabricated in the following manner. The quartz substrate was cleaned with water, chloroform, acetone, and isopropyl alcohol by ultrasonication, and then treated with UV-ozone. C10PcH$_2$ was dissolved in chloroform at a concentration of 8 g/L, and the solution was casted onto the quartz substrate. The powder XRD patterns were simulated by using the powder XRD analysis software (PDXL 2.0). The powder XRD measurement was carried out by using a diffractometer (Rigaku SmartLab) with a Cu Kα line, the wavelength of which was 1.54 Å.

The GIWAXS measurement of the spin-coated thin film was carried out at room temperature in the BL46XU beamline at SPring-8. The schematic diagram of the GIWAXS measurement setup is shown in Fig. 1.7. The X-ray diffraction data were recorded with a two-dimensional position-sensitive detector (Dectris PILATUS 300K) equipped on a Huber eight-axis diffractometer. The wavelength of the X-ray was 1.19 Å, and the incident angle was 0.15°.

3.2.2 Theoretical analysis method

As described in Section 1.3.1, X-rays are diffracted when the scattering vectors match the reciprocal lattice vectors. The magnitudes of the scattering vectors was equal to the wave vector of the incident X-ray, and the start points of the scattering vectors are the origin of the reciprocal lattice space; therefore, the end points of the scattering vectors describe a sphere, called Ewald sphere, with the radius of the wave vector of the incident X-ray. The shape of a 2-D detector in this section was plane; therefore, the measured XRD patterns should be corrected by using the wavelength of the incident X-ray, λ, and the distance between the target and 2-D detector, L_{det}.

$$Q_{x,y} = 2\pi\sqrt{\frac{1}{\lambda^2} + R^2 - \frac{2R}{\lambda}\cos\left(\tan^{-1}\frac{L_x}{L_{\mathrm{det}}}\right)}, \tag{3.1}$$

$$Q_z = \frac{2\pi}{\lambda}\frac{L_y}{\sqrt{L_{\mathrm{det}}^2 + L_x^2 + L_y^2}}, \tag{3.2}$$

$$R = \frac{1}{\lambda}\frac{\sqrt{L_{\mathrm{det}}^2 + L_x^2}}{\sqrt{L_{\mathrm{det}}^2 + L_x^2 + L_y^2}}, \tag{3.3}$$

where, (L_x, L_y) is the coordinate of the 2-D detector and $Q_{x,y}$ and Q_z are wavenumbers of the in-plane and out-of-plane direction, respectively. R is the radius of Ewald sphere in the Q_x-Q_y plane at Q_z.

The d-spacing $d(hk0)$ and plane orientation $\alpha(hk0)$ of the rectangular phase were calculated by Eqs. (1.16) and (1.17), respectively. Therefore, the wavenumbers of the reciprocal lattice vectors were calculated by the following equations,

$$Q_{x,y}^{\mathrm{cal}}(hk0) = \frac{2\pi}{d(hk0)} \sin\alpha(hk0), \tag{3.4}$$

$$Q_{z}^{\mathrm{cal}}(hk0) = \frac{2\pi}{d(hk0)} \cos\alpha(hk0), \tag{3.5}$$

where, $Q_{x,y}^{\mathrm{cal}}(hk0)$ and $Q_{z}^{\mathrm{cal}}(hk0)$ are the calculated wavenumbers of the in-plane and out-of-plane directions, respectively. The molecular packing structures were calculated by minimizing the mean square error between the measured and calculated wavenumbers.

The reciprocal lattice points in the out-of-plane direction cannot be measured by the GI-WAXS technique because of the fixed angle of the incident X-ray; therefore, the position of the reciprocal lattice points in the out-of-plane direction was estimated to be ($Q_{x,y}$, Q_z) = (0,$|Q|$); here, $|Q|$ is the magnitude of the reciprocal lattice vectors and is estimated by the position of the tails of the XRD peaks.

3.3 Results and discussion

3.3.1 Crystal structure determination from powder diffraction data

The measured and simulated powder XRD patterns of C10PcH$_2$ are shown in Fig. 3.2. The simulation was carried out by using the powder XRD analysis software (PDXL 2.0), and the lattice constants of the simulated pattern was calculated to be a = 24.22 Å, b = 19.76 Å, and γ = 90.9° by using the peak position of the measured XRD pattern. The XRD peaks at 2θ = 3.37, 4.62, 5.92, and 7.40° were detected, and the plane interval were calculated to be 23.47, 19.10, 14.91, and 11.93 Å by the Bragg's equation, as shown in Eq. (1.6), respectively. The peaks corresponded to $d(100)$ (24.2 Å), $d(010)$ (19.7 Å), $d(110)$ (15.2 Å), and $d(200)$ (12.0 Å), respectively. Based on these results, the molecular packing structure in the C10PcH$_2$ films was determined to be a = 24.22 Å, b = 19.76 Å, and γ = 90.9°.

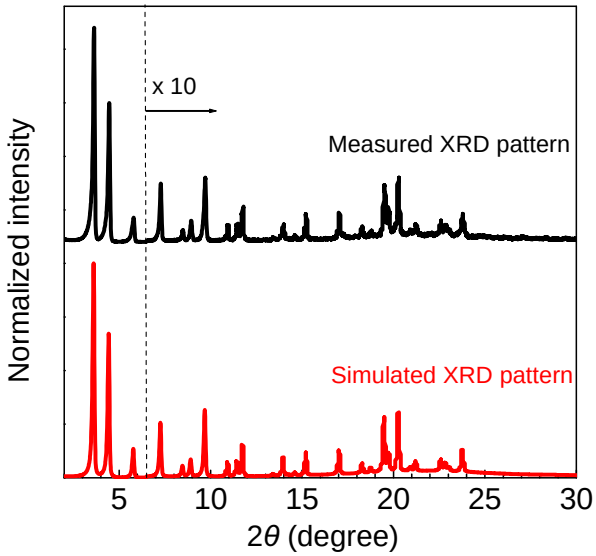

Fig. 3.2 Measured and simulated powder XRD patterns of C10PcH$_2$.

3.3.2 Molecular packing structure

Figure 3.3 shows the XRD pattern of the spin-coated films of C5PcH$_2$, C6PcH$_2$, and C10PcH$_2$, corrected by Eqs. (3.1)–(3.3). The diffraction pattern from a randomly oriented powder is circular because of the averaging of the diffracted intensity at equal scattering angles. Assuming there is no azimuthal dependence of the diffraction pattern in the spin-coated film, the spotty XRD pattern indicates that the phthalocyanine molecules are aligned on the quartz substrate.

The XRD patterns depended on the column interval and intercore distances of C5PcH$_2$, C6PcH$_2$, and C10PcH$_2$. The peaks in a low-wavenumber domain correspond to the column interval, while those in a relatively high-wavenumber domain correspond to the intercore distance and circular peaks corresponding to the quartz substrate.

From the diffraction peaks in a low-wavenumber domain shown in Fig. 3.3(a), many XRD peaks were detected at ($Q_{x,y}$, Q_z) = (0.15, 3.91), (3.23, 2.15), (0.53, 7.63), (6.37, 3.94), (1.19, 11.30), (3.22, 9.61), (6.38, 7.85) and (2.18, 15.13) (nm^{-1}); the peaks are summarized in Table 3.2. From the periodic XRD peaks, the crystal structure of C5PcH$_2$ was determined to be a centered rectangular structure by taking the systematic absence of reflection into consideration. In this case, the measured XRD peaks corresponded to the (002), (101), (004), (202), (006), (105), (204), and (008) planes of the centered rectangular structure, as shown in Table 3.2. From this result, it can be clarified that the column axis of C5PcH$_2$ is parallel to the substrate,

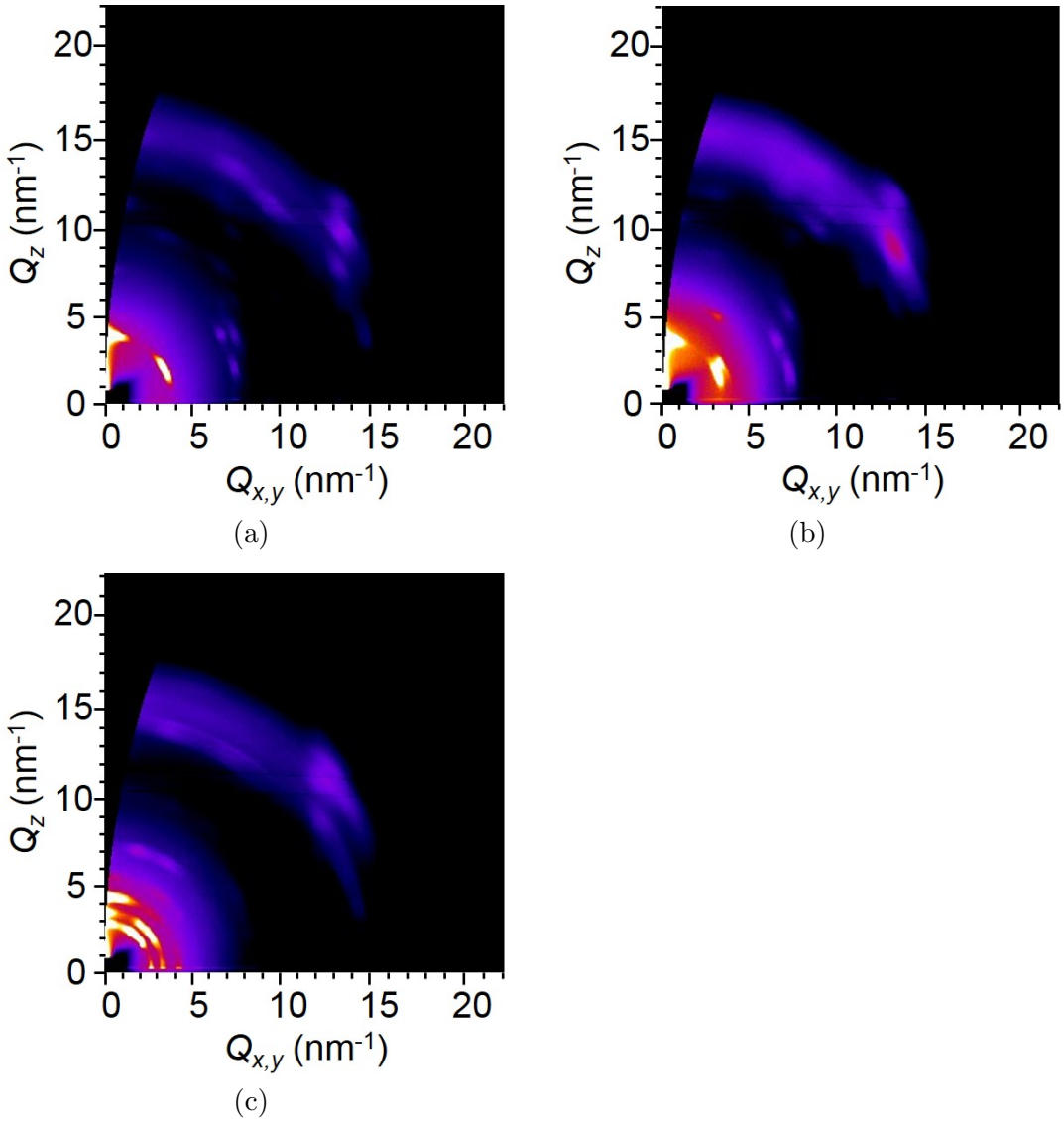

Fig. 3.3 XRD patterns of the spin-coated films of (a) C5PcH$_2$, (b) C6PcH$_2$, and (c) C10PcH$_2$.

and the lattice parameters were calculated to be $a = 19.8$ Å and $c = 31.4$ Å by the least squares method. The schematic diagram of the molecular packing structure of C5PcH$_2$ in the thin film is shown in Fig. 3.4(a).

The position of the XRD peaks based on the (002), (101), (004), (202), (006), (105), (204), and (008) planes were calculated to be ($Q_{x,y}$, Q_z) = (0.00, 4.00), (3.19, 2.00), (0.00, 8.00), (6.38, 4.00), (0.00, 12.00), (3.19, 10.00), (6.38, 8.00) and (0.00, 16.00) (nm^{-1}) by Eqs. (3.4)–(3.5); the peaks are summarized in Table 3.2. The lattice parameters of C5PcH$_2$ β-type crystals were calculated to be $a = 19.38$ Å and $c = 34.29$ Å, and the molecular packing structure is the centered rectangular structure by the single-crystal X-ray structure analysis, as shown in Fig.

2.4(d). The molecular packing structure in the thin film of $C5PcH_2$ was slightly different from that of $C5PcH_2$ β-type crystals. The slight difference in the lattice parameters between the single crystal and the spin-coated film was considered to be caused by the measurement process, such as the conditions of the temperature changes.

The XRD pattern in a low-wavenumber domain of $C6PcH_2$ was also investigated, using a process similar to that of $C5PcH_2$. The XRD peaks were detected at ($Q_{x,y}$, Q_z) = (0.12, 3.55), (3.11, 1.60), (3.06, 4.99), (6.25, 3.69), (1.02, 10.44), and (2.67, 11.95) (nm^{-1}); the peaks are summarized in Table 3.3. Assuming the centered rectangular structure, the peaks corresponded to the (002), (101), (103), (202), (006), and (107) planes. From this result, it can be clarified that the column axis of $C6PcH_2$ is also parallel to the substrate, and the lattice parameters were calculated to be a = 20.3 Å and c = 36.4 Å. The schematic diagram of the molecular packing structure of $C6PcH_2$ in the thin film is shown in Fig. 3.4(c).

The position of the XRD peaks based on the (002), (101), (103), (202), (006), and (107) planes were calculated to be ($Q_{x,y}$, Q_z) = (0.00, 3.45), (3.10, 1.73), (3.10, 5.18), (6.19, 3.45), (0.00, 10.36), and (3.10, 12.08) (nm^{-1}) by Eqs. (3.4)–(3.5); the peaks are summarized in Table 3.3. The lattice parameters of $C6PcH_2$ β-type crystals were a = 20.74 Å and c = 36.10 Å obtained by single-crystal X-ray structure analysis, and the molecular packing structure was the centered rectangular structure, as shown in Fig. 2.4(b). The lattice parameters of β-type $C6PcH_2$ showed temperature dependence and its lattice constants were a = 20.6 Å and c = 36.3 Å at room temperature as shown in Fig. 2.6. These results show that the difference between the lattice constant in the thin films of $C6PcH_2$ and that of β-type $C6PcH_2$ was caused by the measurement temperature. Consequently, the $C6PcH_2$ thin film prepared by spin-coating consisted of $C6PcH_2$ β-type crystals.

The molecular alignment of $C10PcH_2$ in the spin-coated film was also investigated. Many arc-shaped patterns were observed (Fig. 3.3 (c)). The result indicated that the degree of orientation in the $C10PcH_2$ films was lower than that in the $C5PcH_2$ and $C6PcH_2$ films. The wavenumbers of three arc-shaped patterns detected in a low-wavenumber domain were 2.64, 3.33, and 4.33 nm^{-1}, and the plane intervals were calculated to be 23.8, 18.9, and 14.5 Å by the Bragg's equation. As mentioned above, the molecular packing structure of $C10PcH_2$ in the film was determined by the powder pattern and the lattice constants were calculated to be a = 24.22 Å, b = 19.76 Å, and γ = 90.9°. Therefore, the three arc-shaped patterns corresponded to

the (100), (010), and (110) planes of C10PcH$_2$, respectively.

Two peaks were detected in each arc-shaped pattern based on the (100), (010), and (110) planes of C10PcH$_2$. In the case of the (100) plane, the positions of the XRD peaks were ($Q_{x,y}$, Q_z) = (2.00, 1.73) and (1.53, 2.27) (nm^{-1}). For the (010) plane, the positions of the XRD peaks were ($Q_{x,y}$, Q_z) = (1.80, 2.80) and (2.47, 2.13) (nm^{-1}). For the (110) plane, the positions of the XRD peaks were ($Q_{x,y}$, Q_z) = (0.13, 4.33) and (0.80, 4.20) (nm^{-1}). The peaks are summarized in Table 3.4.

The two peaks of each lattice plane indicated that two types of molecular alignment exist in the C10PcH$_2$ thin films. The assumed molecular packing structures of C10PcH$_2$ in the thin film are shown in Figs. 3.4(e) and 3.4(f). In Fig. 3.4(e), the direction of the (110) plane of C10PcH$_2$ is perpendicular to the substrate. In Fig. 3.4(f), the column of C10PcH$_2$ is stacked in the normal direction of the substrate. In the case of the molecular packing structure shown in Fig. 3.4(e), the peak positions of the (100), (010), and (110) planes of C10PcH$_2$ are estimated to be ($Q_{x,y}$, Q_z) = (2.01, 1.63), (2.01, 2.47), and (0.00, 4.11) (nm^{-1}), respectively. The calculated peak positions corresponded to the measured peak position at ($Q_{x,y}$, Q_z) = (2.00, 1.73), (1.80, 2.80), and (0.13, 4.33) (nm^{-1}), respectively. Besides, in the case of the molecular packing structure shown in Fig. 3.4(f), the peak positions of the (100), (010), and (110) planes were estimated to be ($Q_{x,y}$, Q_z) = (1.63, 2.01), (2.47, 2.01), and (0.84, 4.02) (nm^{-1}), respectively. The calculated peak positions corresponded to the measured peak positions at ($Q_{x,y}$, Q_z) = (1.53, 2.27), (2.47, 2.13), and (0.80, 4.20) (nm^{-1}), respectively. The XRD peaks are summarized in Table 3.4. Based on these reasons, it can be clarified that two types of molecular alignment co-existed in the spin-coated thin films of C10PcH$_2$.

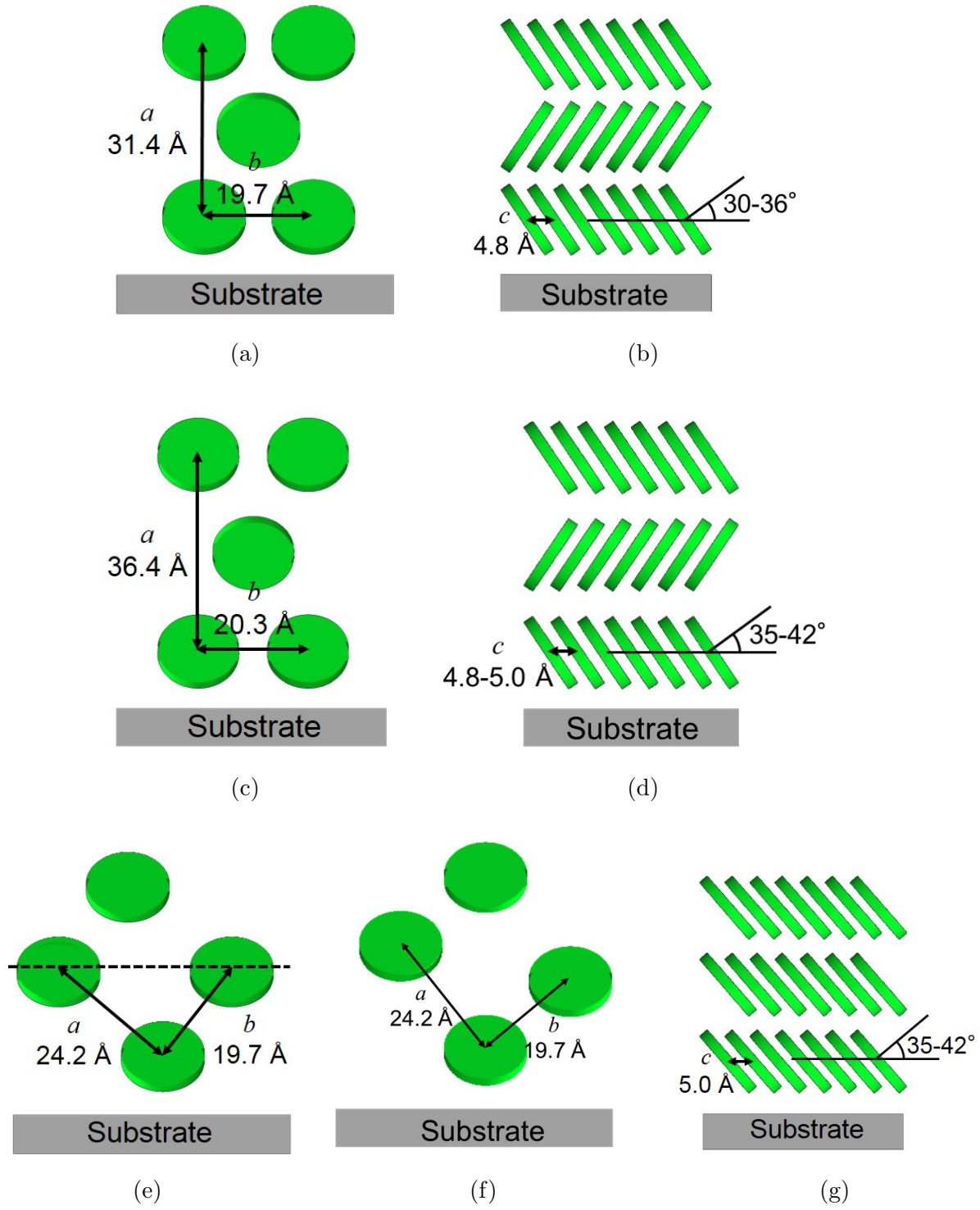

Fig. 3.4 Schematic diagram of the molecular alignment in the spin-coated films of (a), (b) $C5PcH_2$, (c), (d) $C6PcH_2$ and (e)–(g) $C10PcH_2$. The diagram is viewed in the direction (a), (c), (e), (f) parallel and (b), (d), (g) perpendicular to the columnar axis.

Table 3.2 Wavenumber ($Q_{x,y}$, Q_z) of the measured peak positions in the XRD patterns of a spin-coated film of C5PcH$_2$ and calculated peak positions by using the assumed molecular packing structure shown in Fig. 3.4(a), and the corresponding Miller indices (hkl).

Miller index	Measured wavenumber (nm^{-1})		Simulated wavenumber (nm^{-1})	
(hkl)	$Q_{x,y}$	Q_z	$Q_{x,y}$	Q_z
(002)	0.15	3.91	0.00	4.00
(101)	3.23	2.15	3.19	2.00
(004)	0.53	7.63	0.00	8.00
(202)	6.37	3.94	6.38	4.00
(006)	1.19	11.30	0.00	12.00
(105)	3.22	9.61	3.19	10.00
(204)	6.38	7.85	6.38	8.00
(008)	2.18	15.13	0.00	16.00

Table 3.3 Wavenumber ($Q_{x,y}$, Q_z) of the measured peak positions in the XRD patterns of a spin-coated film of C6PcH$_2$ and calculated peak positions by using the assumed molecular packing structure shown in Fig. 3.4(c), and the corresponding Miller indices (hkl).

Miller index	Measured wavenumber (nm^{-1})		Simulated wavenumber (nm^{-1})	
(hkl)	$Q_{x,y}$	Q_z	$Q_{x,y}$	Q_z
(002)	0.12	3.55	0.00	3.45
(101)	3.11	1.60	3.10	1.73
(103)	3.06	4.99	3.10	5.18
(202)	6.25	3.69	6.19	3.45
(006)	1.02	10.44	0.00	10.36
(107)	2.67	11.95	3.10	12.08

Table 3.4 Wavenumber ($Q_{x,y}$, Q_z) of the measured peak positions in the XRD patterns of a spin-coated film of C10PcH$_2$ and calculated peak positions by using the assumed molecular packing structure shown in Fig. 3.4(e), and the corresponding Miller indices (hkl).

Miller index	Measured wavenumber (nm^{-1})		Simulated wavenumber (nm^{-1})	
(hkl)	$Q_{x,y}$	Q_z	$Q_{x,y}$	Q_z
(100)	2.00	1.73	2.01	1.63
(010)	1.80	2.80	2.01	2.47
(110)	0.13	4.33	0.00	4.11
(100)	1.53	2.27	1.63	2.01
(010)	2.47	2.13	2.47	2.01
(110)	0.80	4.20	0.84	4.02

The XRD peaks based on the stacking distance were detected in a high-wavenumber domain in the diffraction patterns. In the case of $C5PcH_2$, the XRD peaks based on the stacking distance were detected at ($Q_{x,y}$, Q_z) = (12.87, 7.67) and (12.73, 9.47) (nm^{-1}). For $C6PcH_2$, the XRD peaks were detected at ($Q_{x,y}$, Q_z) = (12.60, 8.73) and (12.46, 11.33) (nm^{-1}). In the case of $C10PcH_2$, the XRD peaks were detected at ($Q_{x,y}$, Q_z) = (11.87, 8.33) and (12.13, 10.53) (nm^{-1}). X-rays are diffracted by the lattice plane close to the molecular stacking periodicity, i.e., the interval and tilt angle of the diffracted plane are close to the shortest distance of the molecular stacking and tilt angle of the Pc core, respectively. Assuming planar alignment of the columns, the plane interval and tilt angle from the direction parallel to the substrate represent the shortest intermolecular distance and tilt angle from the columns.

In the case of $C5PcH_2$, the intermolecular distance along the column axis was calculated to be approximately 4.8 Å, which agreed with the results of the single-crystal structure analysis. The tilt angle of the normal vector of the Pc core from the column axis was calculated to be 30–36°. The tilt angle of the Pc cores of $C5PcH_2$ β-type crystals was calculated to be 41.27° by single-crystal structure analysis. As mentioned above, X-rays are diffracted by the lattice plane close to the molecular stacking periodicity, i.e., the position of the peaks showed discontinuity. The difference between the tilt angle of the assumed molecular packing structure and single-crystal structure was considered to be caused by the discontinuous position of the lattice plane. The schematic diagram of $C5PcH_2$ in the thin film is shown in Fig. 3.4(b).

The intermolecular distance along the column axis of $C6PcH_2$ was calculated to be 4.8–5.0 Å, which also agreed with the results of single-crystal structure analysis. The tilt angle of the normal vector of the Pc core from the column axis was calculated to be 35–42°. The tilt angle of the Pc cores of $C6PcH_2$ β-type crystals was calculated to be 40.78° by single-crystal structure analysis; therefore, the tilt angle of the Pc cores in the thin films was equal to that of the $C6PcH_2$ β-type crystals. The schematic diagram of $C6PcH_2$ in the thin film is shown in Fig. 3.4(b).

In the case of $C10PcH_2$, the intermolecular distance along the column axis was calculated to be approximately 5.0 Å, and the tilt angle of the normal vector of the Pc core from the column axis was calculated to be 35–42°. Preparation of single-crystals of $C10PcH_2$ was difficult because of the low crystallinity caused by the long alkyl-chain; thus, the detailed crystal structure of $C10PcH_2$ is still not clarified by single-crystal X-ray structure analysis. However, in this study, the rough molecular packing structure can be determined by using powder and thin film X-ray

structure analysis.

The periodic interval of the molecular stacking along the column axis means that the lattice constant b of $C5PcH_2$ and $C6PcH_2$, and lattice constant c of $C10PcH_2$; therefore, the value of the lattice constant b of $C5PcH_2$ and $C6PcH_2$ were determined to be 4.8 and 4.8–5.0 Å, respectively, and the value of the lattice constant c of $C10PcH_2$ was determined to be 5.0 Å. In general, the density of the organic materials was considered to be approximately 1 g/cm^3, and the densities of $C5PcH_2$, $C6PcH_2$, and $C10PcH_2$ were calculated to be approximately 1.20, 1.08, and 1.12 g/cm^3 by using the lattice parameters, respectively. Hence, the calculated molecular packing can be considered to be reasonable.

The degree of orientation in the thin films were calculated by the XRD patterns (Fig. 3.3). Figures 3.5(a) and 3.5(b) show the rocking curves of the (002) plane of $C5PcH_2$ and $C6PcH_2$ and the rocking curves of the (100), (010), and (110) planes of $C10PcH_2$ as a function of the tilt angle from the normal vector of substrate, respectively. The intensity of the rocking curves of the (002) plane in the $C5PcH_2$ and $C6PcH_2$ films was calculated by the integration of the intensity of the XRD pattern in the ranges of $|Q| = 3.0$–4.0 and 3.3–4.3 nm^{-1}, respectively. The intensity of the rocking curves of the (100), (010), and (110) planes in the $C10PcH_2$ film was calculated by the integration of the intensity of the XRD pattern in the ranges of $|Q| = 2.4$–3.1, 3.1–3.7, and 4.0–4.7 nm^{-1}, respectively.

In Fig. 3.5(a), the XRD pattern exhibited two diffraction peaks at 0 and approximately 60°, which correspond to the (002) and (101) plane, respectively. The peak intensity derived from the (002) plane was higher than that derived from the (101) plane. The intensity at the tilt angle of 0° cannot be measured because of the low incident angle, and the half width at half maximum cannot be calculated. However, the distribution at the direction of the tilt angle was estimated to be approximately 10°.

In Fig. 3.5(b), the peaks derived from the (100) plane of $C10PcH_2$ were detected at approximately 0, 35, and 50°. The peaks at 35 and 50° corresponded to the peaks at (1.53, 2.27) and (2.00, 1.73) (nm^{-1}), respectively. The peaks derived from the (010) plane of $C10PcH_2$ were also detected at approximately 0, 35, and 50°. The peaks at 35 and 50° corresponded to the peaks at (1.80, 2.80) and (2.47, 2.13) (nm^{-1}), respectively. Furthermore, the peaks derived from the (110) plane of $C10PcH_2$ were also detected at approximately 0 and 12°. The peaks at 0 and 12° corresponded to the peaks at (0.13, 4.33) and (0.80, 4.20) (nm^{-1}), respectively. The peaks

around 0° appeared in all cases, and the reason for this has been described in Section 3.3.3.

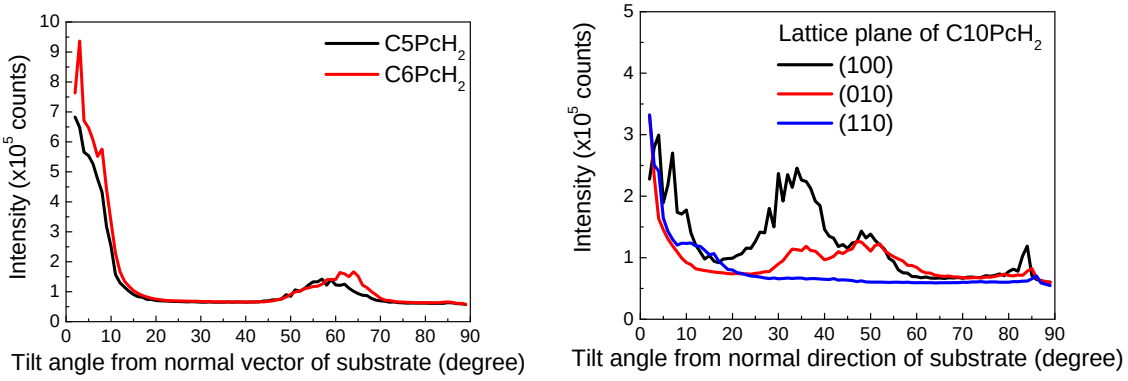

(a) (b)

Fig. 3.5 (a) Rocking curve of the (002) plane of $C5PcH_2$ and $C6PcH_2$ and (b) rocking curve of the (100), (010), and (110) planes of $C10PcH_2$ as a function of the tilt angle from the normal vector of substrate. The intensities are calculated based on Fig. 3.3.

In this section, the molecular packing structures and molecular orientation of $C5PcH_2$, $C6PcH_2$, and $C10PcH_2$ in the thin films prepared by spin-coating were investigated by the GIWAXS method and X-ray rocking curve. The column structures of $C5PcH_2$, $C6PcH_2$, and $C10PcH_2$ were maintained in the spin-coated films, and the direction of the column axis was parallel to the substrate, i.e., planar orientation. Planar orientation of the columnar LC materials in the film prepared by spin-coating has been reported [65]. The driving force of the planar orientation was considered to be the surface free energy at the interface between air and solution. For the control of molecular orientation in a thin film, control of the surface free energy was considered to be important. Additionally, there is no azimuthal dependence in the thin film prepared by spin-coating, and the column structure were maintained in the thin film. These results show that the planar oriented poly-crystals existed in the spin-coated films of $C5PcH_2$, $C6PcH_2$, and $C10PcH_2$.

3.3.3 Simulation of diffraction patterns

The assumed molecular packing structures of $C5PcH_2$, $C6PcH_2$, and $C10PcH_2$ in the thin film shown in Fig. 3.4 were confirmed by Fourier analysis. Figure 3.6 shows Fourier conversion images of the modeled molecular packing structure in spin-coated films in the direction of the column axis, as shown in Figs. 3.4(a), (c), (e), and (f). Miller indices are also shown in the

Fourier conversion images.

Many peaks appeared, and the position of the peaks was similar to the simulated results shown in Table (3.2)–(3.4). Moreover, no peaks appeared at the position of the lattice plane, which satisfied the systematic absence of reflection. From these results, the Fourier conversion images of the molecular packing structures in the spin-coated films well coincided with the measured XRD patterns.

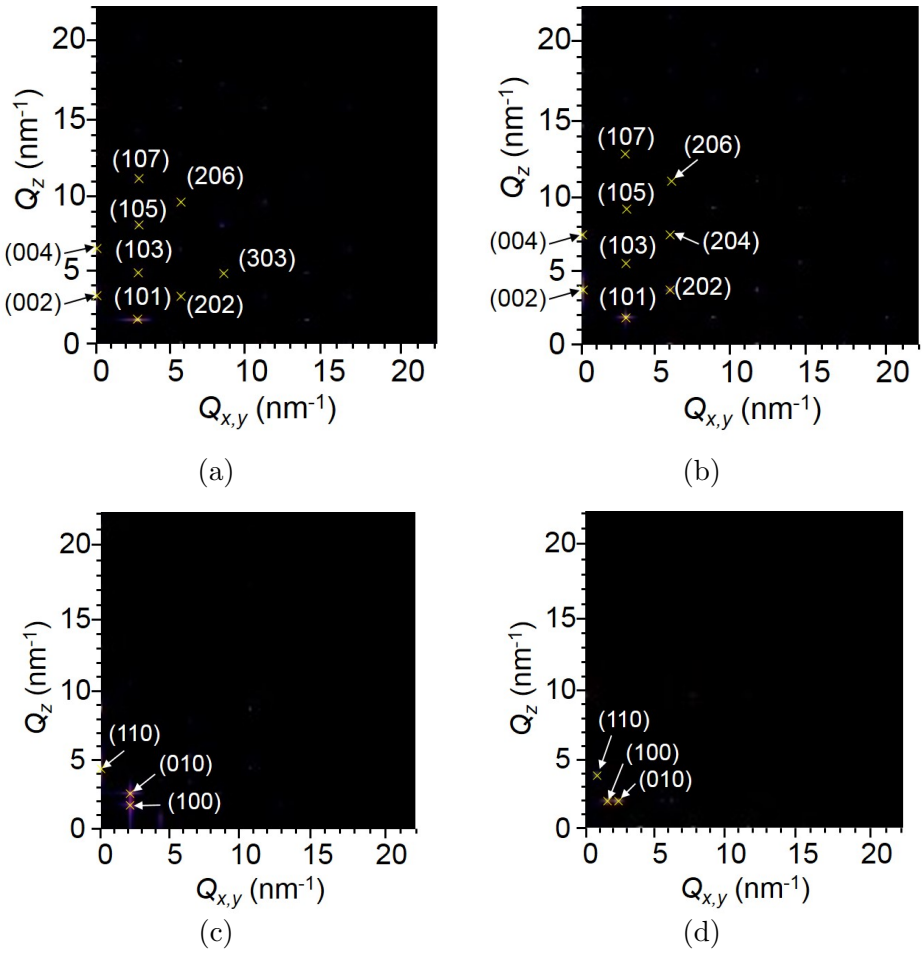

Fig. 3.6 Fourier conversion images of the modeled molecular packing structure in spin-coated films of (a) C5PcH$_2$, (b) C6PcH$_2$, and (c)–(d) C10PcH$_2$ in the direction of the columnar axis as shown in Figs. 3.4(a), (c), (e), and (f), respectively. Cross marks in the Fourier conversion images show the peak positions.

Besides, molecular stacking periodicity was also confirmed by Fourier analysis. Figures 3.7(a) and 3.7(b) show the schematic diagrams, in which the Pc cores were tilted in the same and alternating directions, respectively. The tilt angle and stacking periodicity of the Pc cores were presumed to be the same as the molecular packing structure of C6PcH$_2$ shown in Fig.

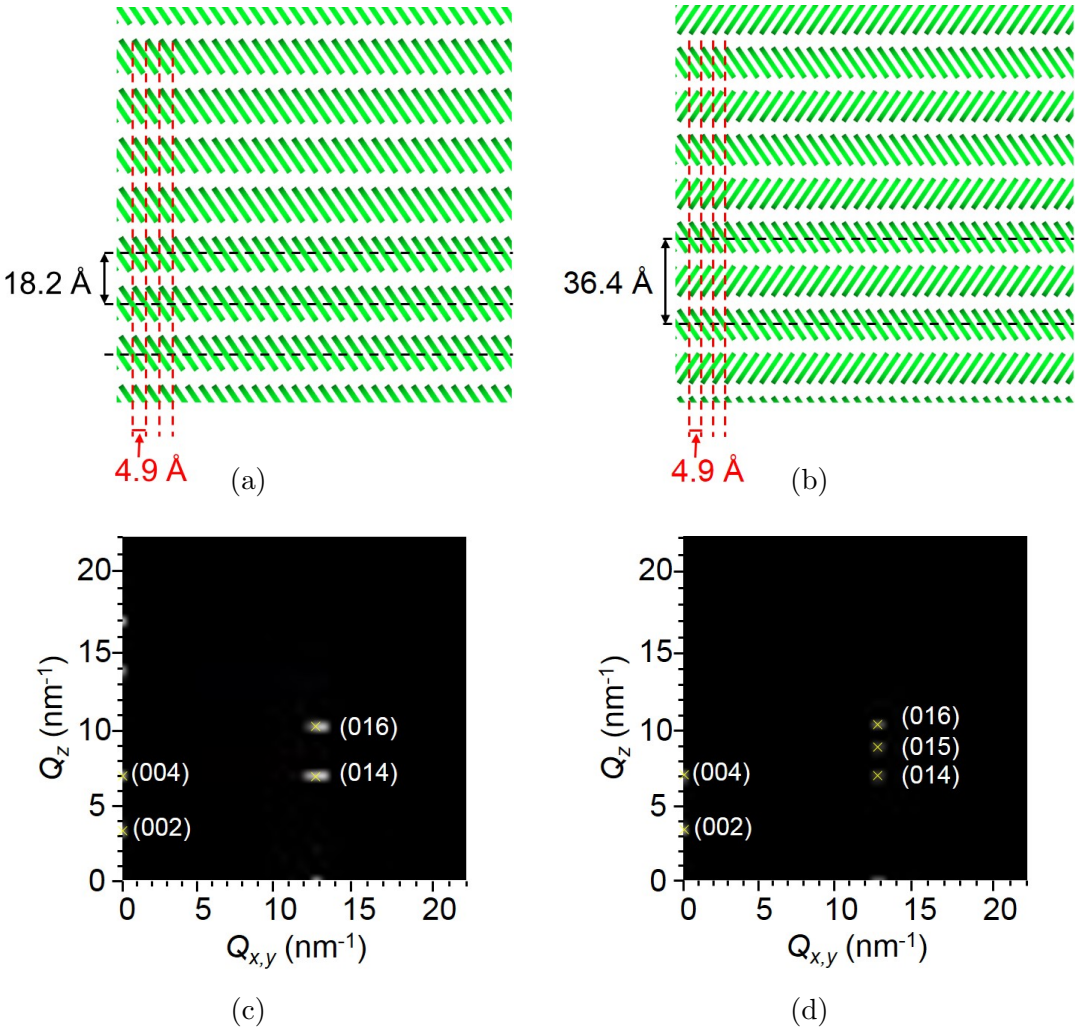

Fig. 3.7 Schematic of (a) monoclinic and (b) herringbone structures and Fourier conversion images of (c) monoclinic and (d) herringbone structures as shown in Figs. 3.6(a), (b), respectively. The tilt angle and stack periodicity of the molecules are the same as the molecular packing structure of C6PcH$_2$ shown in Figs. 3.4(c),(d).

3.4(d). The Fourier conversion images of Figs. 3.7(a) and 3.7(b) are shown in Figs. 3.7(c) and 3.7(d), respectively. The (002) and (004) planes of C6PcH$_2$ were detected at the normal direction of the substrate. The direction of the (002) plane was parallel to the normal direction of the substrate in both the schematic diagrams shown in Figs. 3.4(c) and 3.4(d); therefore, the XRD peaks based on the (002) plane appeared in both the cases of the Fourier conversion images shown in Figs. 3.6 and 3.7. Therefore, the XRD peak based on the (002) plane was detected regardless of the molecular orientation in the spin-coated film. Hence, the peak intensity of the (002) plane was higher than that of the (101) plane, and the result agrees with the X-ray rocking data shown in Fig. 3.5(a).

Considering the high-wavenumber domain, two peaks were detected at ($Q_{x,y}$, Q_z) = (12.8, 6.9) and (12.8, 10.4) (nm^{-1}) in Fig. 3.7(c), while three peaks were detected at ($Q_{x,y}$, Q_z) = (12.8, 6.9), (12.8, 8.6) and (12.8, 10.4) (nm^{-1}) in Fig. 3.7(d). These peaks were based on the molecular stacking periodicity, and the peaks at ($Q_{x,y}$, Q_z) = (12.8, 6.9), (12.8, 8.6) and (12.8, 10.4) (nm^{-1}) corresponded with the (014), (015), and (016) planes of $C6PcH_2$, respectively. The periodic interval of the intercolumn distance shown in Fig. 3.7(a) is 18.2 Å, while that shown in Fig. 3.7(b) is 36.4 Å; therefore, the peak based on the (015) plane disappeared in Fig. 3.7(c) because it satisfies the systematic absence of reflection. Moreover, no peak based on the stacking period of $C6PcH_2$ along the column axis existed in Fig. 3.7(b), which was also consistent with the XRD pattern. Consequently, the crystal structure determined by XRD analysis was ascertained to be consistent with that calculated by Fourier analysis.

3.4 Conclusions

The molecular packing structure and molecular orientational order of $C5PcH_2$, $C6PcH_2$, and $C10PcH_2$ in spin-coated films were studied by using the GIWAXS measurement. The column structures of $C5PcH_2$, $C6PcH_2$, and $C10PcH_2$ were maintained in the spin-coated films. The molecular packing structures of $C5PcH_2$ and $C6PcH_2$ in the thin film were determined to be the centered rectangular structure, while that of $C10PcH_2$ was determined to be a rectangular structure. The lattice constants of $C5PcH_2$, $C6PcH_2$, and $C10PcH_2$ were (a, b, c) = (19.8, 4.8, 31.4), (20.3, 4.8–5.0, 36.4), and (24.2, 19.8, 5.0) (Å), respectively. The molecular packing structures of $C5PcH_2$ and $C6PcH_2$ were similar to the β-type crystals measured by single-crystal X-ray analysis. Additionally, the tilt angle of the Pc core in the column axis was determined. The column axes of $C5PcH_2$, $C6PcH_2$, and $C10PcH_2$ were parallel to the substrate plane, i.e., planar oriented polycrystals existed in the spin-coated films of $C5PcH_2$, $C6PcH_2$, and $C10PcH_2$. The crystal structures determined by XRD analysis were ascertained to be consistent with those calculated by Fourier analysis.

Chapter 4.

Molecular alignment control and molecular packing structure in thin film

4.1 Introduction

The columnar liquid-crystalline (LC) semiconductor, C6PcH$_2$, exhibits high carrier mobility along the column axis. For realizing device applications with high performance, the control of the molecular alignment must be important. For the device configuration of the field-effect transistor (FET), the column axis of C6PcH$_2$ should be parallel to the channel direction of FET, i.e., uniaxially planar alignment in thin films is necessary. In contrast, for conventional solar cells, homeotropically molecular orientation must be there in thin-film active layers.

Uniaxially planar oriented thin films of C6PcH$_2$ have been realized by unique techniques such as heated spin-coating [66], [67] and contact freezing method utilizing the supercooled state [68], [69]. These fabrication processes were carried out at the temperature of the LC phase of C6PcH$_2$, and undesired cracks generated in the films in the cooling process because of the volumetric shrinkage, which is a crucial problem for the FET application. To avoid the thermal shrinkage, the process must be conducted at room temperature. Moreover, it is expected that molecular oriented thin films can be realized by controlling the speed and direction of the crystal growth. Uniaxial planar alignment of columnar LC materials in thin films have been reported using a printing method such as the zone-casting method [32]. In this study, a bar-coating method was used as a candidate method for fabricating uniaxially planar oriented thin films of C6PcH$_2$ [70].

Homeotropic alignment of C6PcH$_2$ in a conventional sandwich-cell structure with two glass plates, used for LC display devices, has been reported by thermal annealing through the LC

phase [71], [72]. This homeotropic alignment process has been used to investigate the unique properties of columnar LC materials, in which the homeotropic alignment is induced in the LC phase without the air interface [65]. However, the sandwich-cell structure with two glass plates might restrict the processability of mass production of the columnar LC materials. Solution-processed homeotropically oriented thin films of columnar LC materials utilizing the polymer layer instead of the glass substrate have been proposed [73], and they seem to be available for the homeotropic alignment of C6PcH$_2$. In this study, fabrication of homeotropically oriented thin films of C6PcH$_2$ was carried out by applying the reported method for C6PcH$_2$.

The carrier transport properties in the thin films are strongly related with the molecular packing structure; thus, analysis of the molecular packing structure in the thin film is important for discussing electrical conduction. Though the molecular packing structure in the uniaxially planar oriented thin films must be ordered three-dimensionally (3-D) like a single-crystal, the analysis method for the molecular packing structure in the 3-D oriented thin film is yet to be established. As explained in Section 1.3.2, the 3-D periodic structure has 3-D information in the reciprocal lattice space, such as the plane interval, tilt angle, and azimuthal angle. However, it is difficult to detect all XRD peaks by the general GIWAXS technique even if the two-dimensional (2-D) detector was used. The modified GIWAXS method is needed for determining the 3-D periodic structure in the thin film.

In this study, the GIWAXS technique with sample rotation was proposed as a modified GIWAXS method for clarifying the 3-D periodic structure in a molecularly oriented thin film. Using the modified analysis method, 3-D information of the reciprocal lattice points could be obtained as with the single-crystal X-ray structure analysis, and details of the molecular packing structure in the thin films could be determined. The 3-D molecular packing structure in the molecularly oriented thin film is discussed by simulating the diffraction pattern by using the single-crystal structure of C6PcH$_2$ discussed in Chapter 2.

4.2 Fabrication of uniaxially planar oriented thin films

4.2.1 Materials and sample fabrication method

The $C6PcH_2$ thin films were fabricated in the following manner. Glass substrates were cleaned with water, chloroform, acetone, and isopropyl alcohol by ultrasonication and then treated with UV-ozone. The $C6PcH_2$ thin films were fabricated on the glass substrate by the bar-coating method. A schematic diagram of the bar-coating process is shown in Fig. 4.1. A 9.6-mm-diameter coating bar, around which a 0.05-mm-diameter metal wire was wound, was fixed on the glass substrate. $C6PcH_2$ was dissolved in *p*-xylene at a concentration of 60 g/L, and the solution was added dropwise onto the coating bar, and then the glass substrate was moved in the horizontal direction at a speed of 30 µm/s. A small amount of the solution passed through the space between the wound metal wire and the glass substrate, resulting in the formation of a uniform film with a thickness of approximately 170 nm.

The film thickness and surface morphology of the thin film were observed by an atomic force microscope (AFM) (KEYENCE VN-8000 and Digital Instruments Nanoscope IIIA). Polarizing optical microscopy images and polarized absorption spectra of the thin film were obtained with a polarized optical microscopy system (Nikon Eclipse LV 100 POL) and an attached spectrometer (Hamamatsu PMA-11).

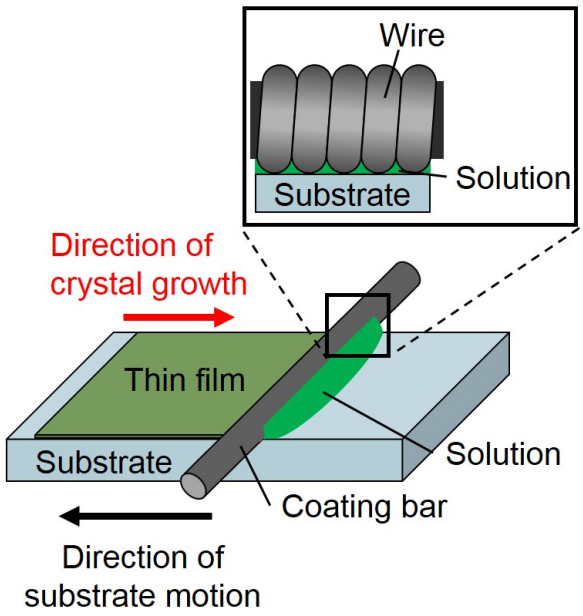

Fig. 4.1 Schematic diagram of the bar coating process.

4.2.2 Optical anisotropy and surface morphology

Figure 4.2 shows the typical polarized optical microscopy images of the bar-coated C6PcH$_2$ thin film observed with the crossed polarizers. Some striations perpendicular to the direction of the crystal growth, which were considered to be caused by a mismatch between the crystal growth rate and sweep speed, were observed. The results indicated that the thin film consisted of poly-crystals. These images were uniformly bright and dark at the diagonal and extinction positions, respectively, which indicates that a uniform and uniaxial molecular oriented thin film was obtained with an area of approximately 1 mm^2. The polarized absorption spectra of the thin film are shown in Fig. 4.3. When the polarization direction of the incident light was parallel or perpendicular to the crystal growth direction, the absorbance based on the Q-band of phthalocyanine was minimum or maximum, respectively. The absorbance should be maximum if the polarization direction of the incident light is parallel to the in-plane direction of the phthalocyanine core. Therefore, it is considered that the column axis was parallel to the crystal growth direction.

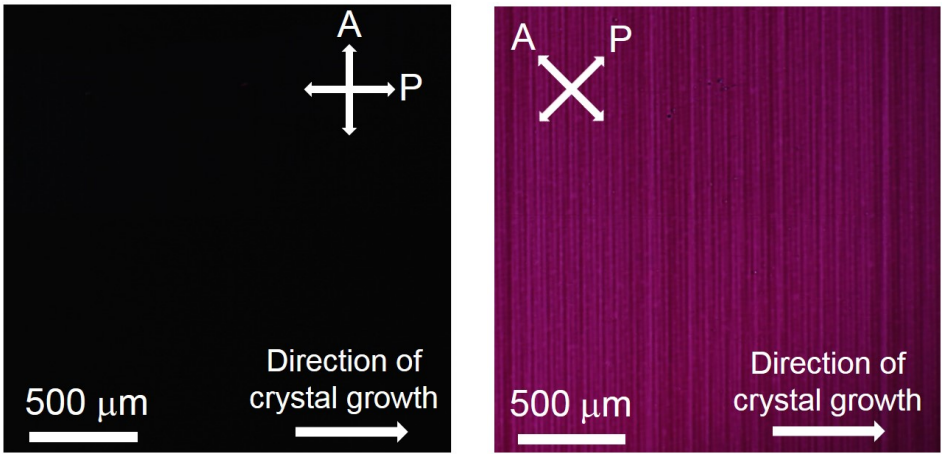

(a) (b)

Fig. 4.2 Polarized optical microscopic images of the thin film observed with crossed polarizers in (a) extinction and (b) diagonal position.

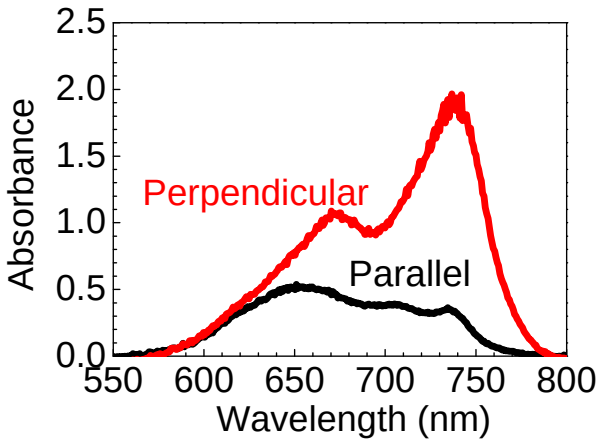

Fig. 4.3 Polarized absorption spectra of the aligned thin film. The incident light was parallel (black line) or perpendicular (red line) to the crystal growth direction.

Figure 4.4 shows an AFM image and surface profile of the thin film. Terraces and steps with a height of 2 nm, which corresponded to the lattice spacing of the (002) plane in the C6PcH$_2$ β-type crystal, were observed. This result implies that the crystal growth occurred during the film formation by the bar-coating method; moreover, the lattice vector of the (002) plane was perpendicular to the substrate.

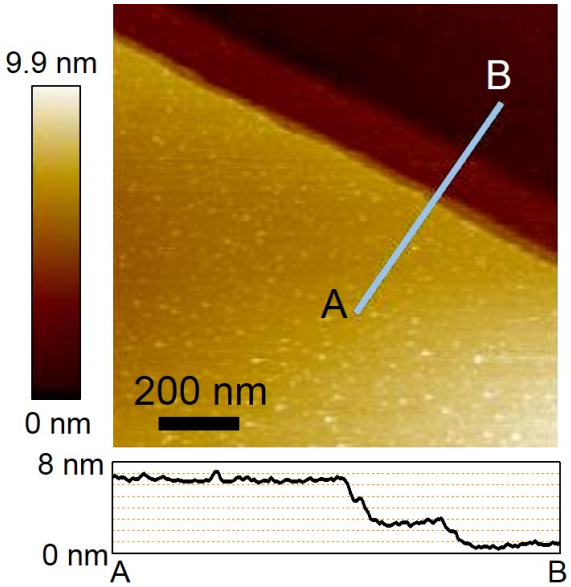

Fig. 4.4 AFM image and surface profile of the aligned thin film. The profile corresponds to the white line in the image.

4.3 Crystal structure analysis in uniaxially planar oriented thin films

4.3.1 Measurement setups

The GIWAXS measurement of a thin film was carried out at room temperature in the BL46XU beamline at SPring-8. The schematic diagram of the GIWAXS measurement setup is shown in Fig. 1.7. The X-ray diffraction was detected with a two-dimensional (2-D) position-sensitive detector (Dectris PILATUS 300K) equipped on a Huber eight-axis diffractometer. The wavelength of the X-ray was 1.0 Å and the incident angle was 0.12°. The GIWAXS measurement was carried out, while the thin film was rotated counterclockwise at a speed of 24°/min.

4.3.2 Theoretical analysis method

The calibration method of the XRD pattern in a $Q_{x,y}$–Q_z plane has been already described using Eqs. (3.1)–(3.3). The GIWAXS measurement with the fixed sample can be obtained a 2-D XRD pattern in the $Q_{x,y}$–Q_y plane, while the GIWAXS measurement with the sample rotated can be obtained a 3-D XRD pattern. That is, the XRD pattern in a Q_x–Q_y plane can be calculated as well as that in a $Q_{x,y}$–Q_z plane, and the XRD patterns can be evaluated in the azimuthal direction. Assuming $Q_z = 0$, a Q_x–Q_y plane in a polar coordinate system can be calculated as follows,

$$|Q_{x,y}| = \frac{2\sqrt{2}\pi}{\lambda}\sqrt{1-\cos\left(\tan^{-1}\frac{L_x}{L_{\rm det}}\right)}, \tag{4.1}$$

$$\varphi = \tan^{-1}\frac{1-\cos\left(\tan^{-1}\frac{L_x}{L_{\rm det}}\right)}{\sin\left(\tan^{-1}\frac{L_x}{L_{\rm det}}\right)} + \varphi_{\rm sam}, \tag{4.2}$$

where, $|Q_{x,y}|$ is the distance from the origin of the reciprocal space, i.e., $|Q_{x,y}| = \sqrt{Q_x^2 + Q_y^2}$; φ is a angle from the $|Q_x|$ axis, L_x is the distance in the plane direction from the position of the direct beam on the 2-D detector, and $\varphi_{\rm sam}$ is the angle of sample rotation.

The simulation of the XRD patterns was also carried out in the following manner. In the simulation, the analyzed data of the β-type C6PcH$_2$ single-crystal, which has a monoclinic structure with a space group $P2_1/n$, a = 20.7430, b = 9.7984, c = 36.0961 Å, α = 90, β = 93.8750, and γ = 90° as shown in Table. 2.1, were used.

The peak positions were simulated in the following manner. The reciprocal lattice vector $\boldsymbol{G}$

was calculated by

$$\boldsymbol{G} = h\boldsymbol{a}^* + k\boldsymbol{b}^* + l\boldsymbol{c}^*, \tag{4.3}$$

where, h, k, and l are Miller indices, and $\boldsymbol{a}^*$, $\boldsymbol{b}^*$, and $\boldsymbol{c}^*$ are basic reciprocal lattice vectors. The coordinates of the reciprocal lattice points (G_x, G_y, G_z) were calculated by

$$G_x = 2\pi\frac{h}{a}, \tag{4.4}$$

$$G_y = 2\pi\left[\frac{h}{a}(-\cot\gamma) + \frac{k}{b}(\sin\gamma)^{-1}\right], \tag{4.5}$$

$$G_z = \frac{2\pi}{u\sin\gamma}\left[\frac{h}{a}(\cos\alpha\cos\gamma - \cos\beta) + \frac{k}{b}(\cos\beta\cos\gamma - \cos\alpha) + \frac{l}{c}\sin^2\gamma\right], \tag{4.6}$$

where, a, b, c, α, β, and γ are the unit-cell parameters, and $u = (2\cos\alpha\cos\beta\cos\gamma - \cos^2\alpha - \cos^2\beta + \sin^2\gamma)^{1/2}$ [74]. Intersection points of the reciprocal lattice vector and Ewald sphere were calculated by

$$\varphi = \cos^{-1}\frac{\lambda\left(G_x^2 + G_y^2 + G_z^2\right)}{4\pi\sqrt{G_x^2 + G_y^2}} - \tan^{-1}\frac{G_x}{G_y}, \tag{4.7}$$

where, φ is the rotation angle of the measured sample. From these equations, the positions of the XRD peaks can be calculated. The peak intensity was calculated by Eqs. (1.8)–(1.12) and confirmed by using the RIGAKU PDXL 2.6 software. Relative factor R_{F} was calculated to evaluate the difference between observed and measured peak intensities, and R_{F} is calculated by

$$R_{\mathrm{F}} = \frac{\sum||F_{\mathrm{O}}| - |F_{\mathrm{C}}||}{\sum|F_{\mathrm{O}}|} \times 100, \tag{4.8}$$

where, F_{O} and F_{C} are the observed and calculated value of the peak intensity, respectively.

4.3.3 Determination of molecular orientation

Figure 4.5(a) shows the XRD patterns when the incident X-ray was parallel to the crystal growth direction in the bar-coating method. $Q_{x,y}$ and Q_z are the wavenumbers in the in-plane and out-of-plane directions of the bar-coated thin film, respectively, and Q_y is the wavenumber in the

direction parallel to the sweep direction. Wavenumbers Q were given by the equation,

$$Q = 2\pi/d, \tag{4.9}$$

where, d is the lattice spacing. Spotty XRD patterns were detected because the C6PcH$_2$ molecules were aligned on the glass substrate. Periodic XRD peaks were detected at $Q_{x,y}$ = 3.10 nm^{-1} (20.2 Å) in the in-plane direction. The periodic structures in the in-plane direction correspond to the lattice constant a (20.7 Å) of β-type C6PcH$_2$ as shown in Fig. 4.5(b). Moreover, a strong XRD peak, which corresponds to the (002) plane of β-type C6PcH$_2$ (18.0 Å), was detected at Q_z = 3.52 nm^{-1} (17.8 Å) in the out-of-plane direction. The measured lattice intervals were coincident with the lattice parameters of β-type C6PcH$_2$; therefore, the molecular packing structure in the bar-coated thin film was similar to that of the C6PcH$_2$ β-type single-crystal, and the molecular stacking was parallel to the crystal growth direction.

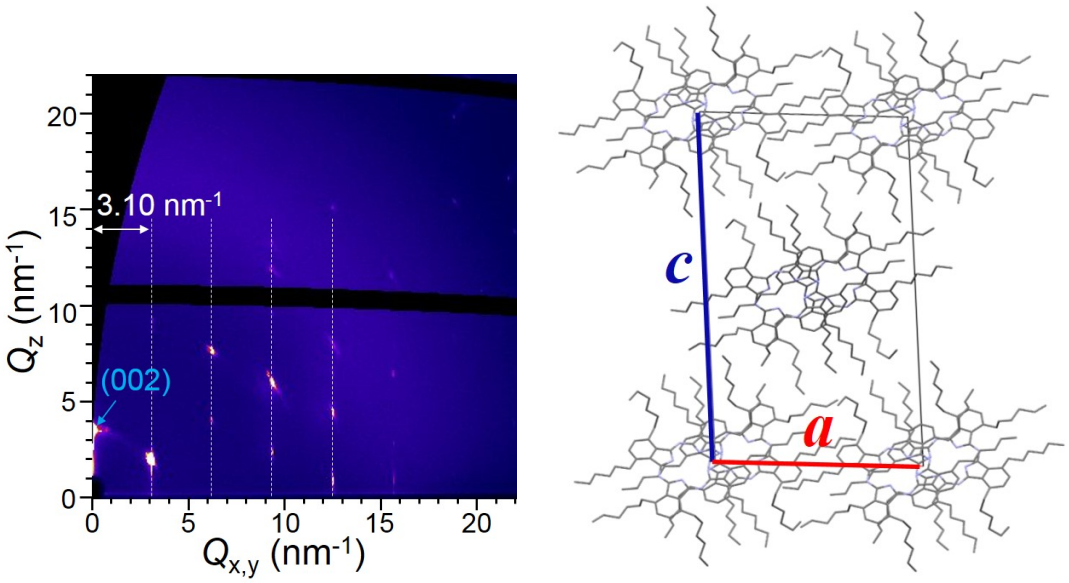

(a) (b)

Fig. 4.5 (a) XRD patterns of the thin film when the incident X-ray was parallel to the crystal growth direction of the bar coating method. (b) Molecular packing structure of C6PcH$_2$ in the direction of the crystal growth direction of the bar coating method.

Figure 4.6(a) shows the azimuthal dependence of the XRD pattern, obtained by integrating the XRD patterns for the in-plane direction while the thin film was rotated by 360°. Using the GIWAXS technique involving sample rotation, it was possible to determine the azimuthal

distribution in the film, which is not possible using the conventional GIWAXS technique with a fixed sample. A spotty XRD was clearly obtained owing to the small azimuthal distribution based on the high orientational order in the thin film. The XRD peaks with the periods of 3.13 nm^{-1} (20.1 Å) and 6.26 nm^{-1} (10.0 Å) were detected, which almost corresponded to the lattice constants a (20.7 Å) and b (9.80 Å) of β-type C6PcH$_2$, as shown in Fig. 4.5(b).

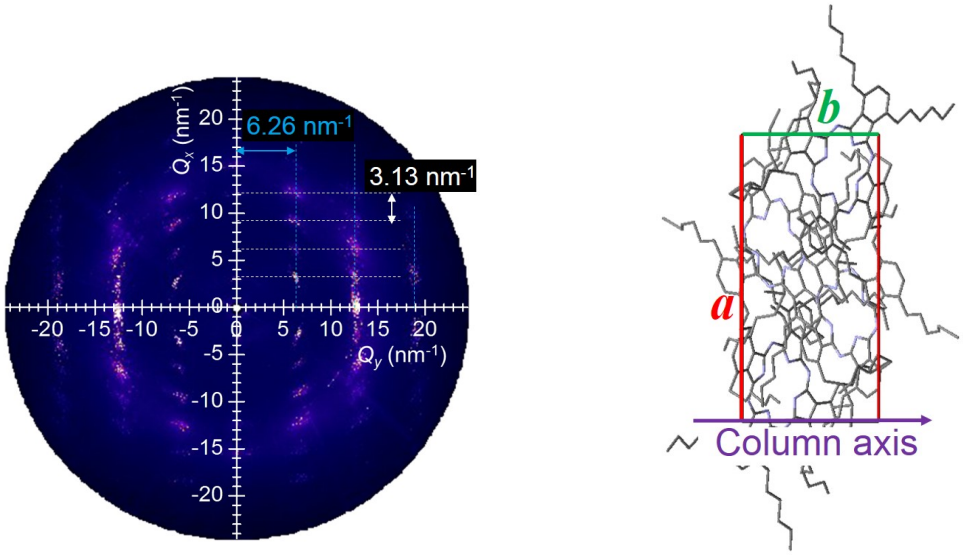

(a) (b)

Fig. 4.6 (a) Azimuthal dependence of the XRD patterns of the thin film. (b) Molecular packing structure of C6PcH$_2$ viewing from directly above the position.

From these results, molecular packing structure and molecular alignment direction in the bar-coated thin films were clarified. The column axis of C6PcH$_2$ in the bar-coated thin film was clarified to be parallel to the sweep direction of the wire-bar. This result could be discussed based on the crystal growth rate. The β-type C6PcH$_2$ crystals were needle-like, as shown in Fig. 2.3(d), and the crystal growth rate along the column axis is relatively high. In the bar-coating technique, the sweep direction is parallel to the crystal growth direction; therefore, the direction of the high crystal growth rate was considered to be parallel to the sweep direction.

The molecular orientation distribution in the azimuthal direction was evaluated by the X-ray rocking curve. Figure 4.7 shows the rocking curves of the (101) plane of β-type C6PcH$_2$ in the bar-coated thin film. The intensity was calculated by the integration of intensity in the area around the peak position of the (101) plane, which is $(Q_{x,y}, Q_z) = (3.13, 2.07)$ (nm^{-1}). Many peaks appeared at the sample rotation angles of 169–178° and 349–358°. The reciprocal

lattice points of the (101) plane existed on the Q_x–Q_z plane, and the sample rotation angles satisfying the diffraction conditions were calculated to be 178.6 and 358.6° by Eq. (4.7), i.e., the calculated results almost coincided with the measured ones. The peak width of the XRD peak was approximately 8–9°, and the number of XRD peaks were 7. The peak width of the XRD peak represents the distribution in the azimuthal direction, and the irradiation area of X-rays were approximately 40 μm×1 cm; therefore, the distribution in the azimuthal direction in the thin film fabricated by bar-coating was considered to be approximately 8–9° in the area of 40 μm×1 cm. The number of peaks represents the number of domains with the different orientation; therefore, at least seven domains existed in the area of 40 μm×1 cm.

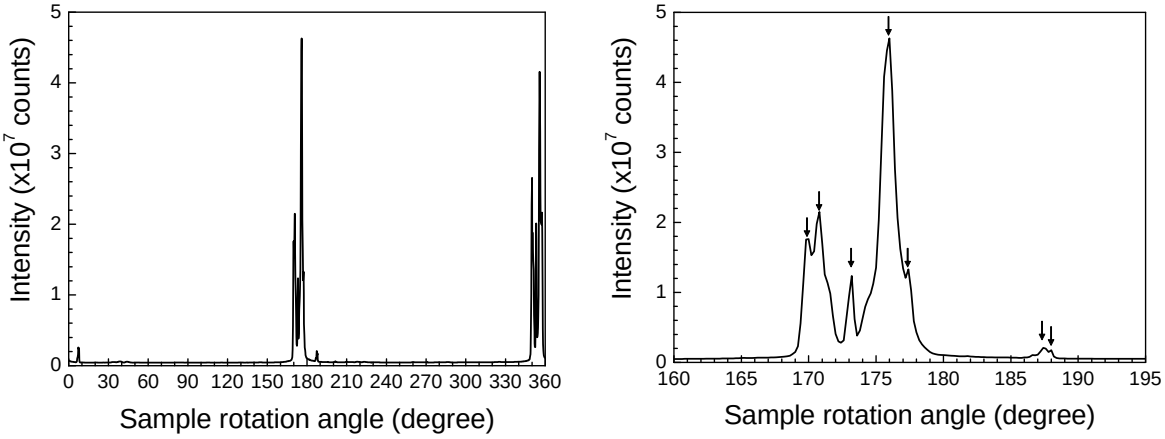

Fig. 4.7 Rocking curve of the (101) plane of β-type C6PcH$_2$ in the bar-coated thin film. Sample rotation angles were in ranges (a) 0–360° and (b) 160–195°. The intensity was calculated by integration of the intensity in the area around the peak position of (101) plane, which is ($Q_{x,y}$, Q_z) = (3.13, 2.07) (nm^{-1}). Arrows in Fig. 4.7(b) represent the diffracted peaks.

4.3.4 Three-dimensional molecular packing structure

Figure 4.8 shows the XRD patterns measured by the GIWAXS method when the thin film was rotated counterclockwise by 0, 30, 60, 90, 120, and 150°. The spotty XRD patterns in the longitudinal direction can be clearly observed because the Miller index l is independent of the azimuthal ($Q_{x,y}$) direction. The values of $Q_{x,y}$ at the XRD peaks and the sample rotation angle fulfilling the Bragg's diffraction qualification depended on the Miller indices h and k. The values of Q_z at the XRD peaks mainly depended on the Miller index l. The Miller indices estimated by using the single crystal structure are shown in Fig. 4.8.

Strong peaks based on the (12l) (l = -7, -6, -5, 5, 6) planes were detected at ($Q_{x,y}$, Q_z) = (13.2, 9–12) (nm^{-1}), as shown in Figs. 4.8(c) and 4.8(d), because these diffraction surfaces almost correspond to the periodic surfaces based on the inter-core distance of C6PcH$_2$. Furthermore, these results were in agreement with the XRD patterns of spin-coated films as shown in Fig. 3.3.

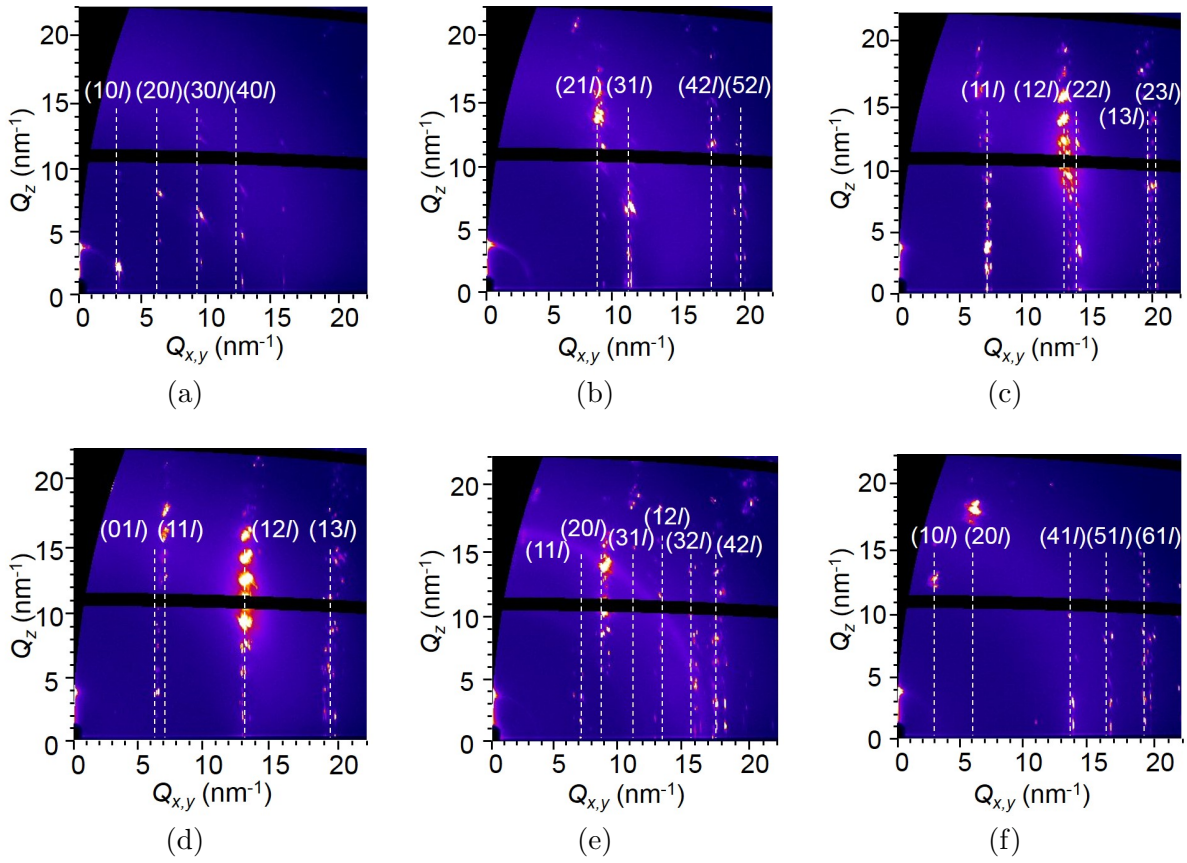

Fig. 4.8 XRD patterns and Miller indices of the thin film when the thin film rotated counterclockwise by (a) 0, (b) 30, (c) 60, (d) 90, (e) 120, and (f) 150°. Here, the angle when the incident X-ray was parallel to the crystal growth direction of the bar coating method was set to be 0°.

4.3.5 Simulation of diffraction patterns

Figure 4.9 show the XRD patterns simulated using the data for C6PcH$_2$ single crystals when the thin film was rotated counterclockwise by 0, 30, 60, 90, 120, and 150°. The simulation was carried out assuming that the (002) plane was parallel to the Q_z direction. The shape of the peak in the simulation was postulated to possess a normal distribution, the standard deviation of which was assumed to be 0.01 nm^{-1} in the out-of-plane and in-plane directions and 2° in the azimuthal

direction. Comparison of Figs. 4.8 and 4.9 shows that the simulated peak positions reproduced the observed ones. Table 4.1 show the observed and simulated relative peak intensities in Figs. 4.8 and 4.9, respectively. By comparing the observed peak intensities with the simulated ones, R_F was evaluated to be 0.48 by Eq. (4.8), which was higher than the typical value obtained by single crystal analysis; however, this value was similar to the reported value of a previous study by using the highly oriented thin film [74]. The quality of the crystal in the bar-coated thin film was inferior to the single crystal; however, the highly oriented polycrystalline thin films could be fabricated. It is considered that such uniform and uniaxially oriented thin films were obtained because of the properties of C6PcH$_2$, such as high solubility, high crystallinity, and uniaxial crystal growth along the molecular packing direction. The uniaxially oriented thin film is expected to be used in electronic device applications, such as organic thin film transistors.

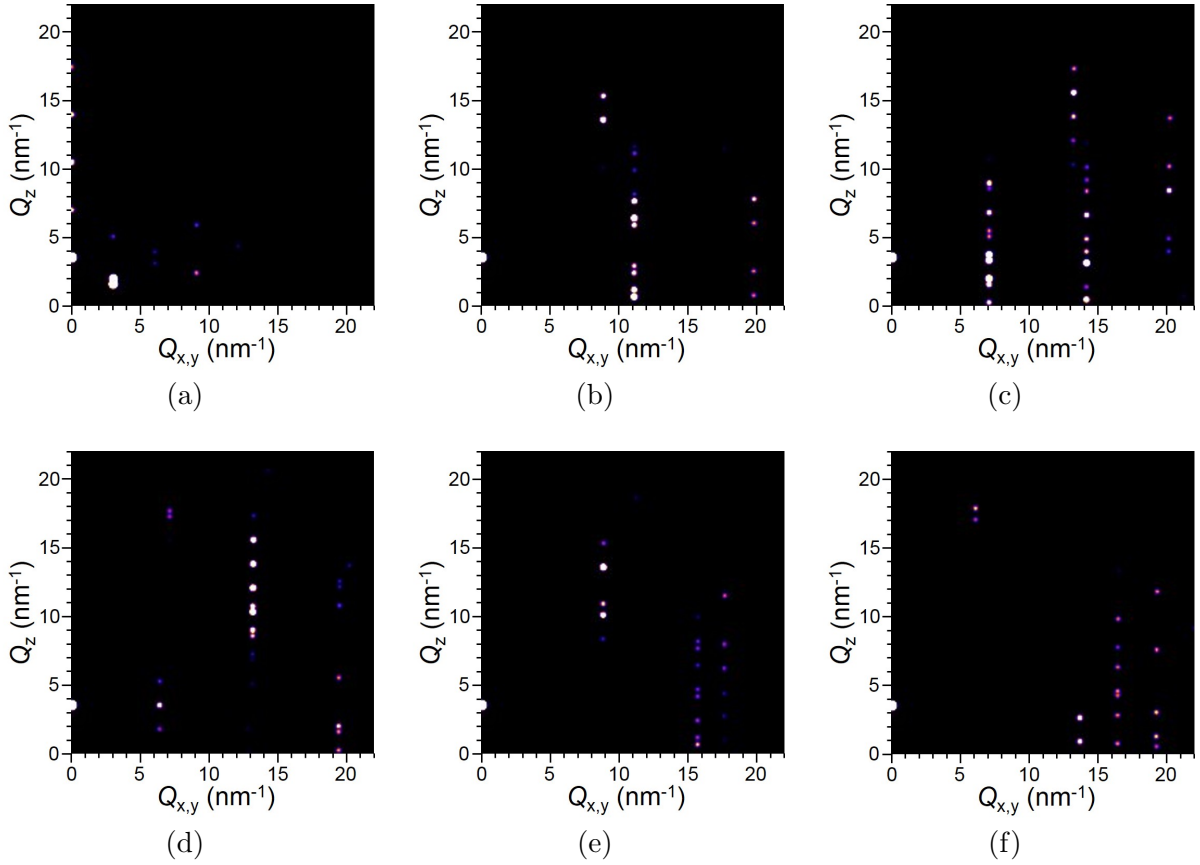

Fig. 4.9 Simulated patterns of the thin film by using the data of C6PcH$_2$ single crystal when the angles between the direction of the incident X-ray and the a axis of C6PcH$_2$ were (a) 0, (b) 30, (c) 60, (d) 90, (e) 120, and (f) 150°.

Table 4.1 Observed and simulated relative peak intensities in Figs. 4.8 and 4.9, respectively. The peak intensity based on the (002) plane was assumed to be 100. Simulated peak intensities were calculated by the single-crystal structure.

Miller index	$(10\bar{3})$	(011)	$(20\bar{2})$	(110)	(202)	$(11\bar{1})$	(012)	(111)	$(11\bar{2})$	(112)
Measurement	1.62	0.13	0.07	0.16	0.11	0.49	1.84	1.15	1.07	1.54
Simulation	1.4	0.2	0.1	0.3	0.1	0.7	1.9	3.3	2.6	2.2
Miller index	(013)	(210)	(202)	$(21\bar{1})$	(113)	$(10\bar{5})$	$(21\bar{2})$	(301)	(014)	(204)
Measurement	0.97	0.18	0.11	0.61	1.17	0.14	0.14	0.62	0.30	0.63
Simulation	0.7	0.4	0.4	0.1	0.9	0.5	0.5	1.0	0.4	0.3
Miller index	$(11\bar{4})$	$(21\bar{3})$	(213)	(303)	$(21\bar{4})$	(310)	$(31\bar{1})$	(311)	(115)	$(31\bar{2})$
Measurement	1.50	0.28	0.78	1.98	0.15	0.85	0.67	0.32	1.80	0.31
Simulation	0.5	0.1	0.7	1.6	0.3	1.9	0.9	0.3	1.8	0.2
Miller index	(214)	$(21\bar{5})$	$(30\bar{5})$	$(40\bar{2})$	(313)	$(31\bar{4})$	(020)	(402)	(021)	(120)
Measurement	0.21	0.72	0.99	0.92	0.93	2.89	1.78	1.03	0.21	0.45
Simulation	0.2	1.0	0.4	0.4	0.4	3.0	0.4	1.2	0.6	0.1
Miller index	$(12\bar{1})$	(022)	(121)	(314)	$(12\bar{2})$	$(40\bar{4})$	(122)	(410)	$(41\bar{1})$	(023)
Measurement	0.87	0.28	0.95	1.54	0.16	0.35	0.29	0.91	1.26	2.21
Simulation	1.2	0.1	0.6	1.0	0.1	0.1	0.1	1.0	1.5	0.9
Miller index	(411)	$(41\bar{2})$	$(12\bar{3})$	(220)	(404)	$(22\bar{2})$	(024)	$(30\bar{7})$	$(12\bar{4})$	$(22\bar{3})$
Measurement	1.22	0.83	1.39	1.17	0.60	3.44	2.73	1.80	1.11	0.47
Simulation	2.5	1.2	1.5	1.2	0.3	3.4	0.4	1.0	0.4	0.4
Miller index	(413)	(124)	$(22\bar{4})$	$(12\bar{5})$	(414)	(125)	(225)	(027)	$(12\bar{7})$	
Measurement	0.36	2.50	1.75	3.41	0.26	8.92	1.10	6.74	6.29	
Simulation	0.1	1.0	1.3	2.1	0.1	6.6	0.5	1.0	2.5	

4.4 Homeotropically oriented thin film

4.4.1 Sample fabrication method and measurement setups

Glass substrates were cleaned with an alkaline solution (Furuuchi Chemical Semico Clean 56) and water by ultrasonication, and then treated with UV-ozone. C6PcH$_2$ was dissolved in chloroform at a concentration of 60 g/L, and the solution was spin-coated onto the glass substrates at a speed of 500 rpm, as shown in Fig. 4.10(a). The film thickness was estimated to be approximately 450 nm by the optical absorption measurement of spectrophotometry (Shimadzu UV-3150). PVP (Aldrich Mw 25,000) was dissolved in methanol at a concentration of 40 g/L, and the solution was spin-coated onto the C6PcH$_2$ layer at a speed of 3000 rpm, as shown in Fig. 4.10(b). Figure 4.11 shows the molecular structure of PVP. The film thickness was estimated to be approximately 160 nm by a surface profilometer (Veeco DEKTAK 150). The sample was heated to 175 °C in the isotropic phase of C6PcH$_2$ at a rate of 20 °C/min, and cooled down to room temperature

at a rate of 10 °C/min. The homeotropic alignment of C6PcH$_2$ as shown in Fig. 4.10(c) was expected in this study.

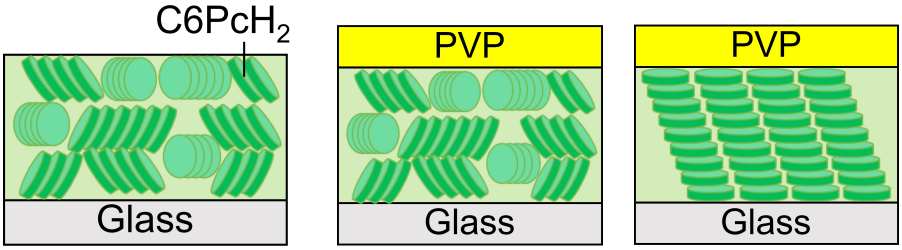

(a) (b) (c)

Fig. 4.10 Schematic diagrams of (a) the C6PcH$_2$ spin-coated thin film as grown, (b) the C6PcH$_2$ thin film covered with the PVP layer, and (c) the C6PcH$_2$ thin film covered with the PVP layer after thermal treatment at 175 °C.

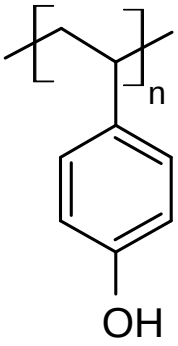

Fig. 4.11 Molecular structure of PVP.

The polarizing optical microscopy (POM) images were obtained with a polarized optical microscopy system (Nikon Eclipse LV100 POL). Molecular alignment in the thin films was investigated by a GIWAXS technique, which was carried out in the BL46XU and BL18B2 beamline at SPring-8 with the approval of JASRI (No. 2016A1776 and 2017B1745). The wavelength of the X-ray was 1.0 Å and the incident angle was 0.12°. A 2-D position-sensitive detector (Dectris PILATUS 300K) was used as an X-ray detector. The GIWAXS measurement was carried out at room temperature under atmospheric pressure or at 160 °C under a pressure of approximately 10^{-3} Pa.

4.4.2 Molecular orientation in homeotropic alignment process

In the GIWAXS measurement of the C6PcH$_2$ thin films, characteristic XRD patterns, as shown in Fig. 4.12, were observed in a four-step-fabrication process: (i) the film state spin-coated as grown, (ii) covered with the PVP layer, (iii) heated to 175 °C and then set at 160 °C, and (iv) cooled down to set at room temperature. The XRD pattern of the C6PcH$_2$ thin film prepared by spin-coating in the first step is shown in Fig. 4.12(a). Many arc-shaped pattens were observed in the diffraction image. In general, a spot-like diffraction pattern appears from a single crystal or a highly oriented condensed matter, while a circular diffraction pattern appears from a randomly oriented substance, such as a powder sample, because of the averaging of the diffracted intensity at each scattering angle. Therefore, this figure seems to indicate that phthalocyanine molecules were slightly aligned in the thin film prepared by spin-coating. Two strong peaks were detected at ($Q_{x,y}$, Q_z) = (0.00, 3.60) and (2.80, 2.00) (nm^{-1}), from which the plane intervals were calculated to be 17.5 and 18.3 Å, respectively. These two strong peaks in Fig. 4.12(a) seem to originate from the intercolumn distance, which are correspond to the (002) and (101) planes of C6PcH$_2$ β-type crystal, respectively. Strong peaks at ($Q_{x,y}$, Q_z) = (12.87, 8.47) and (12.93, 11.33) (nm^{-1}) were observed, the plane intervals of which were estimated to be 4.08 and 3.65 Å, respectively, and they were interpreted to be based on the intermolecular distance, and corresponding to the (125) and (12$\overline{6}$) planes of C6PcH$_2$, respectively. Therefore, the direction of the c axis of C6PcH$_2$ was clarified to be perpendicular to the substrate.

In the second step, the XRD pattern of a C6PcH$_2$ layer covered with a PVP layer is shown in Fig. 4.12 (b). The pattern was almost similar to that in Fig. 4.12(a), which indicates that the molecular packing structure and molecular alignment in the C6PcH$_2$ layer remained after coating the PVP layer, and that the diffraction originating from the PVP layer was too weak to recognize.

When the sample was heated up to 175 °C in the isotropic phase and then cooled down to 160 °C in the LC phase (the third step), the XRD pattern changed markedly, as shown in Fig. 4.12(c). The arc-shaped patterns as shown in Figs. 4.12(a) and 4.12(b) disappeared, and a sharp and circular XRD pattern was detected at $|Q|$ = 3.59 nm^{-1} (17.5 Å), which corresponds to the intercolumn distance, and a broad XRD pattern was detected at $|Q|$ = 17.13 nm^{-1} (3.67 Å), which corresponds to the intermolecular distance. Here, $|Q|$ is the wavenumber calculated

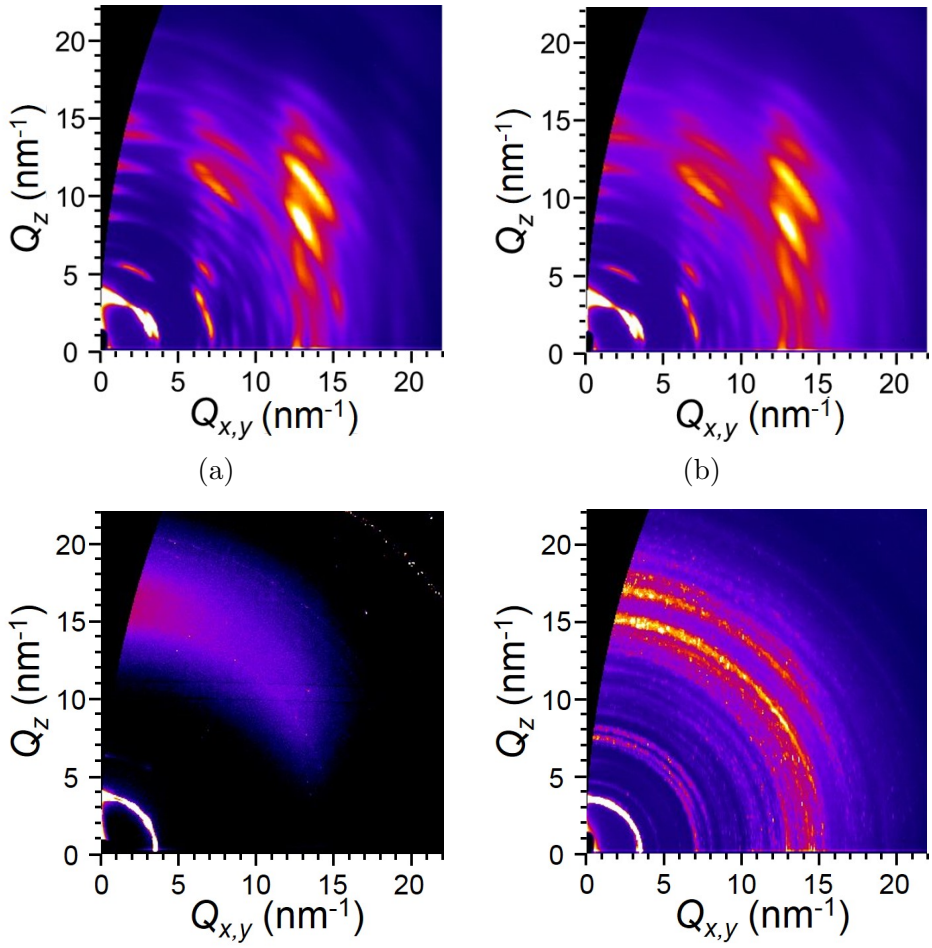

Fig. 4.12 XRD patterns of (a) the C6PcH$_2$ spin-coated thin film as grown, (b) the C6PcH$_2$ thin film covered with a PVP layer, (c) the C6PcH$_2$ thin film covered with the PVP layer at 160 °C, and (d) the C6PcH$_2$ thin film covered with the PVP layer after thermal treatment at 175 °C. The cooling rate from 175 °C to room temperature was 10 °C/min, and the measurements for (a), (b), and (d) were carried out at room temperature.

by the equation, $|Q| = \sqrt{Q_{x,y}^2 + Q_z^2}$. The broad XRD pattern indicates the disordered molecular stacking distance in the LC phase and the homeotropic alignment induced between the PVP layer and glass substrate. According to a previous study, C6PcH$_2$ forms a pseudo-disordered columnar mesophase in the LC phase [23]. Assuming the pseudo-disordered columnar mesophase of C6PcH$_2$, the column interval was calculated to be $17.5 \times 2/\sqrt{3} = 20.2$ Å, which coincided with the reported value [23].

Cooling down to room temperature in the crystal phase as the final step, the marked change could be also found in the XRD pattern, as shown in Fig. 4.12(d). The circular XRD pattern,

which is completely different from those of Figs. 4.12(a)–(c), appeared. The circular XRD pattern implies the low molecular orientation order in the thin film. The strong diffraction at $|Q| = 3.60$ nm^{-1} (17.4 Å), based on the intercolumn direction and corresponds to the (002) plane of the C6PcH$_2$ β-type crystal, was detected. The diffraction for the intermolecular direction was detected at $|Q| = 15.24$ nm^{-1} (4.12 Å) and 17.31 nm^{-1} (3.63 Å), which corresponds to the (125) and (12$\overline{6}$) planes of the C6PcH$_2$ β-type crystal, respectively. The diffraction intensity based on the intermolecular interval in the out-of-plane direction was much higher than that in the in-plane direction; that is, the homeotropic alignment of C6PcH$_2$ molecules in the thin film still remained in the final step via phase transition from the LC to crystal phase. Therefore, the homeotropic alignment in the thin film was induced in the LC phase of the third step and was maintained after the cooling process involving the phase transition.

4.4.3 Cooling rate dependence of molecular orientation

Figure 4.13 shows the cooling rate dependence of the XRD patterns of the films. Some peaks were obtained with the low cooling rate. When the films consist of small domains of C6PcH$_2$, diffraction from each domain is weak; therefore, XRD patterns without any strong peak are obtained. however, for the films comprising of large domains, diffraction from each domain is strong; therefore, XRD patterns with peaks are obtained. These XRD patterns imply that the domain sizes of C6PcH$_2$ increased with decreasing cooling rates. For the cooling rates of 2 and 1 °C/min, some peaks were detected at $Q_{x,y}$ = 12–13 nm^{-1} and Q_z = 9–12 nm^{-1}. The peak positions were almost the same as for those based on the intermolecular distance in the film prepared by spin-coating, as shown in Fig. 4.12(a). The results indicate that the planar orientations tend to form with decreasing cooling rates.

The details of the molecular alignment in the thin film was investigated by the X-ray rocking curve. Figure 4.14 shows the XRD intensity based on the molecular stacking distance of C6PcH$_2$ as a function of the tilt angle from the normal direction of the substrate. The intensity at various tilt angles was evaluated by integrating the intensity in $|Q|$ = 14–19 nm^{-1} in Fig. 4.13. The XRD peak at 0° must indicate the homeotropic alignment of C6PcH$_2$ in the thin film. The signal around the tilt angle of 0° cannot be measured because of the fixed incident angle of X-rays.

For the cooling rate of 10 °C/min, the XRD intensity monotonously decreased as the tilt angle increased, i.e., homeotropic alignment was induced. The XRD patterns changed as the

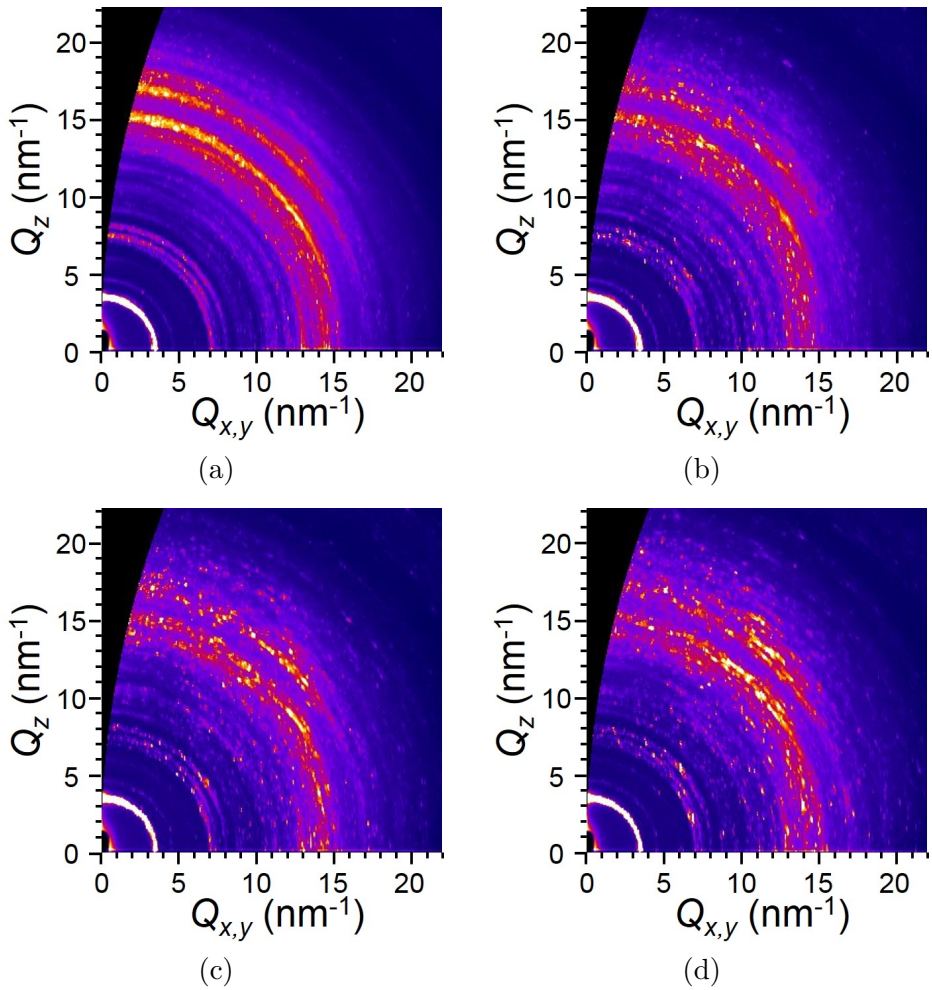

Fig. 4.13 XRD images of the C6PcH$_2$ thin film covered with the PVP layer after thermal treatment at 175 °C. The cooling rates from 175 °C to room temperature are (a) 10, (b) 5, (c) 2, and (d) 1 °C/min.

cooling rate decreased, and for the cooling rate of 1 °C/min, the XRD peak appeared around the tilt angle of 50°. The peaks were based on the stacking periodicity of the planar alignment of C6PcH$_2$; therefore, planar orientation tends to be induced with decreasing cooling rates.

The domain size of C6PcH$_2$ in the films was observed by POM. Figure 4.15 shows the cooling rate dependence of the POM images of C6PcH$_2$ layers covered with PVP layers after thermal annealing, as shown in Fig. 4.10(c). The domain size of C6PcH$_2$ increased with decreasing cooling rates. The results agreed with the XRD patterns as shown in Fig. 4.13.

The molecular alignment in the thin films was discussed by considering the domain shape. The domain size of C6PcH$_2$ increased, and planar alignment was induced with decreasing cooling rates. In the case of small domains, the crystal growth occurred at various points in the films,

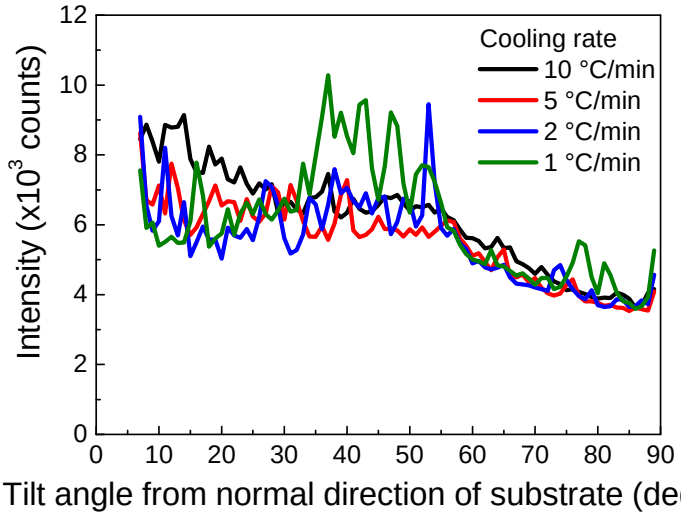

Fig. 4.14 XRD intensity based on the molecular stacking distance of C6PcH$_2$ as a function of the tilt angle from the normal direction of the substrate. The intensity was integrated from the intensity of $|Q| = 14$–19 nm^{-1} in the XRD pattern, as shown in Fig. 4.13.

.

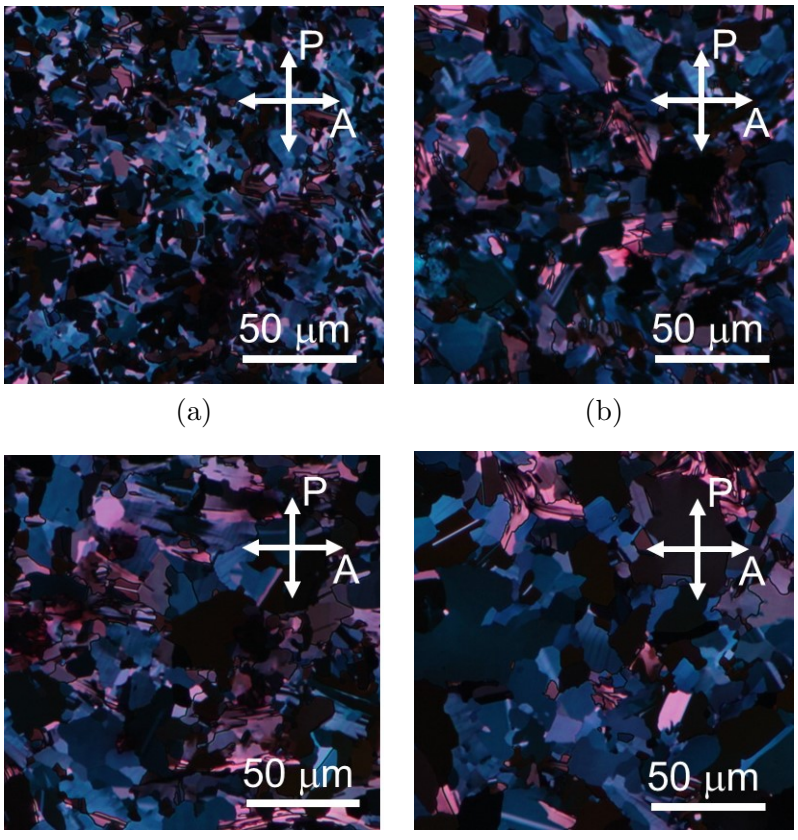

Fig. 4.15 POM images of the C6PcH$_2$ thin film covered with the PVP layer after thermal treatment at 175 °C. The cooling rates from 175 °C to room temperature are (a) 10, (b) 5, (c) 2, and (d) 1 °C/min.

and the crystal growth parallel to the substrate was suppressed because of the domain boundary. In the case of large domains, the crystals can grow in the direction parallel to the substrate. The crystals of $C6PcH_2$ were needle-like, and the crystal growth rate along the molecular stacking direction of $C6PcH_2$ is larger than that along the intercolumn direction. Thus, in the case of a low cooling rate, large domains were formed, and the crystal growth parallel to the substrate occurred, and the column axis tends to be parallel to the substrate, i.e., planar alignment was induced.

4.5 Discussion

The X-ray rocking curve measurement is a well-known evaluation method for the oriented thin films. The peak width of the rocking curve shows the orientation distribution in the thin film. In this study, the oriented thin film was evaluated by the GIWAXS measurement with sample rotation, and the difference between the measured and calculated peak intensities in the XRD patterns, i.e., R_{F} was calculated. R_{F} shows the difference between the modeled and effective positions of the atoms in the crystal lattice. Therefore, R_{F} can indicate the degree of certainty of the modeled crystal structure. In this section, the calculation technique of the detailed molecular packing structure was proposed by using R_{F}.

As an ideal XRD analysis for the thin films, it is desired that the details of the molecular packing structure in the thin films should be determined only from the XRD patterns without clarifying the single-crystal structure. However, it is logically difficult because of the phase problem. The XRD patterns express time-averaged X-ray diffraction, and phase information of the X-ray could not be extracted. Since both the intensity and phases of X-rays are needed for the calculation of the molecular packing structures, the problem could not be solved. However, XRD patterns are easily calculated from the data of the molecular packing structure as shown in this study.

In a previous study, the details of the molecular packing structure in the thin film prepared by thermal evaporation were determined from the XRD pattern [74]. The schematic diagrams of the simulation process are shown in Fig. 4.16. This simulation process consists of four steps. Firstly, the molecular packing structure in the film is assumed. Secondly, the XRD pattern is calculated from the assumed molecular packing structure. Thirdly, the simulated XRD pattern is compared with the measured one, and R_{F} is calculated as discussed in Section 4.3.5. Finally,

this process is repeated by using various kinds of assumed molecular packing structures, and the minimum R_F can be obtained. In the case of the minimum R_F, the assumed molecular packing structure is considered to be close to the real molecular packing structure.

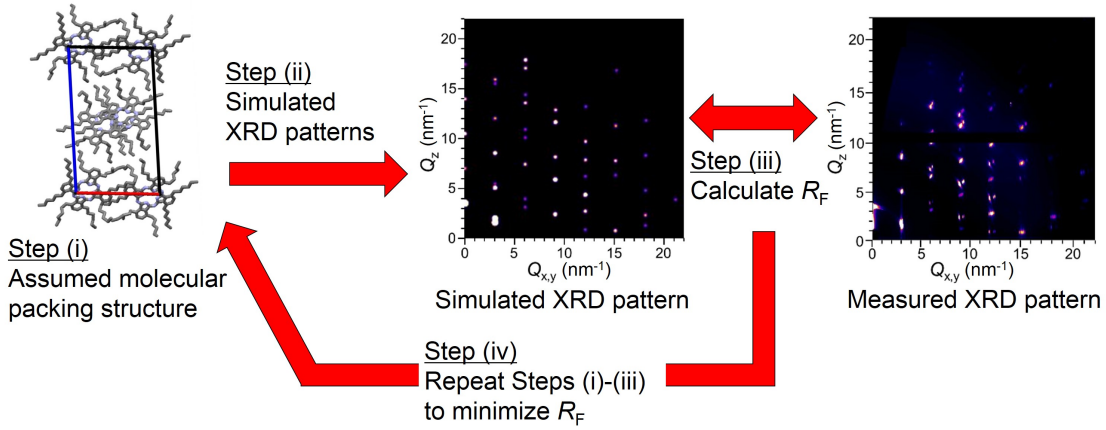

Fig. 4.16 Schematic diagram of the simulation procedure to determine the detailed molecular packing structure in the thin film by the GIWAXS technique.

The simulation procedure is considered to be suitable for the 3-D oriented films, such as the uniaxially planar oriented thin films in this study. In thin films with the 3-D periodic structures like a single-crystal, the azimuthal dependence of the XRD pattern should be obtained. The unit lattice can be easily determined because the XRD peaks can be clearly splitted. For example, in this study, Q_x, Q_y, and Q_z axes almost corresponded to the a, b, and c axes of the C6PcH$_2$ β-type crystal, respectively. For films with ramdom orientation in the azimuthal direction, all XRD peaks overlapped in the $Q_{x,y}$–Q_z plane, and the determination of the unit cell becomes difficult, resulting in low accuracy. By rotating samples in the GIWAXS measurement, the XRD peaks can be distinguished, and peak intensity with high precision can be calculated. For these reasons, the simulation procedure utilizing the 3-D oriented films is considered to be effective for the determination of the molecular packing structure in the films.

4.6 Conclusions

The uniaxially planar orineted thin films of C6PcH$_2$ were fabricated by the bar-coating method, and its 3-D crystal structure was investigated by the GIWAXS method with a sample rotation. The fabricated thin film exhibited optical anisotropy in a large area and possessed molecular-size steps on the surface. From the analysis of the XRD patterns and the results of GIWAXS

measurement and by comparison with the simulations, it was clarified that the molecular packing structure in the thin film three-dimensionally coincided with that of the C6PcH$_2$ single crystal and that the molecular stacking was parallel to the crystal growth direction.

Moreover, the XRD patterns were simulated by using the molecular packing structure obtained by single-crystal X-ray structure analysis, and R_{F} was calculated. The simulation process of the detailed molecular packing structure in a uniaxially planar oriented thin film by using R_{F} was proposed, and the effectiveness of the GIWAXS measurement utilizing a uniaxially planar oriented thin film was indicated.

The homeotropic alignment of C6PcH$_2$ in the thin film was realized by the thermal treatment of the C6PcH$_2$ thin film covered with the PVP layer, and the molecular alignment in the thin film was investigated by the GIWAXS method. The homeotropic alignment was induced in the LC phase, and the molecular alignment was maintained at room temperature in the crystal phase. Moreover, the molecular alignment direction depended on the cooling rate from the LC phase of C6PcH$_2$, and the homeotropic alignment in the thin films was indicated to be induced in the case of the rapid cooling.

Chapter 5.

Carrier transport properties of molecularly oriented thin films and device applications

5.1 Introduction

Generally, columnar LC semiconductors exhibit a high carrier mobility along the column axis. Electrical anisotropy of a columnar LC semiconductor, hexa-perihexabenzocoronene (HBC) derivatives, have been reported [32], [41]. Oriented thin films of HBC derivatives have been fabricated by zone casting or solution casting on substrates with the pre-oriented poly(tetrafluoroethylene) films, and FETs utilizing oriented thin films were developed. The mobilities parallel and perpendicular to the column axis were 5×10^{-3} and 1.0×10^{-5} cm^2/Vs, respectively, i.e., the mobility parallel to the column axis was two orders of magnitude higher than that perpendicular to the column axis.

C6PcH$_2$ is also predicted to exhibit a high carrier mobility along the column axis by the density functional theory (DFT) calculation as mentioned in Chapter 2; however, the electrical anisotropy has not been experimentally clarified yet. In the previous works, the electrical anisotropy of HBC was obtained by the FET measurement; thus, the FET measurement was an effective method for clarifying electrical anisotropy. However, the transistor devices utilizing C6PcH$_2$ films have not been reported. This chapter discusses the fabrication of the FETs utilizing the uniaxially planar oriented thin films by bar-coating, as described in Chapter 4. The electrical anisotropy of C6PcH$_2$ was investigated by the transistor measurement. The carrier mobility is discussed by taking the simulated mobility by the DFT calculation into consideration.

Solar cells utilizing molecular oriented thin films are also discussed in this chapter. The solar cells with a bulk hetero-junction of C6PcH$_2$ and 1-(3-methoxycarbonyl)-propyl-(6,6)C61

(PCBM) have been studied, and the fabrication conditions such as the buffer layer [75], phase separation structure [76], [77], [78] , and kinds of acceptor materials [79] were optimized. However, solar cells utilizing the molecularly oriented thin films have not been reported. Considering the device configuration of conventional organic thin-film solar cells, the homeotropic alignment in the thin film should be developed because of the efficient carrier transport along the column axis of $C6PcH_2$. In this chapter, the fabrication of the bulk heterojunction solar cells utilizing the aligned $C6PcH_2$ by thermal treatment through the LC phase is discussed as with Chapter 4, and the solar cell performance was measured. The photovoltaic properties are discussed by taking the carrier mobility into consideration.

5.2 Field effect transistors utilizing planar oriented thin films

5.2.1 Sample fabrication method

Figure 5.1(a) shows the schematic structure of a typical bottom gate and top contact type FET, which consists of six parts: the gate electrode, insulating layer, surface modifying layer, carrier transport layer, hole injection layers, and source/drain electrodes. In this section, the surface modifying layer, carrier transport layer, and hole injection layers were optimized.

Surface modifying layers were prepared in the following manner. Surface of an n^+ Si substrate covered with a 300-nm-thick SiO_2 layer was cleaned with an alkaline solution (Semico Clean 56, Furuuchi Chemical) and water by ultrasonication and then treated with UV-ozone. Polyimide (JSR AL1254), hexamethyldisilazane (HMDS), or decyltrichlorosilane (DTS) was used as a surface preparation agent, and the surface modifying layer was fabricated onto the SiO_2/Si substrate. The molecular structures of polyimide, HMDS, and DTS are shown in Fig. 5.2. A several-nm-thick polyimide layer was formed on the SiO_2/Si substrate by spin-coating the 20-times-diluted solution with γ-butyrolactone. In general, a rubbed polyimide layer is used as an alignment layer in LC studies, but the rubbing process was not carried out here. HMDS and DTS layers were formed by vapor deposition at 130 and 150 °C for 2 h in a hermetic container under nitrogen atmosphere, respectively, and then excess surface preparation agents were cleaned with toluene by ultrasonication.

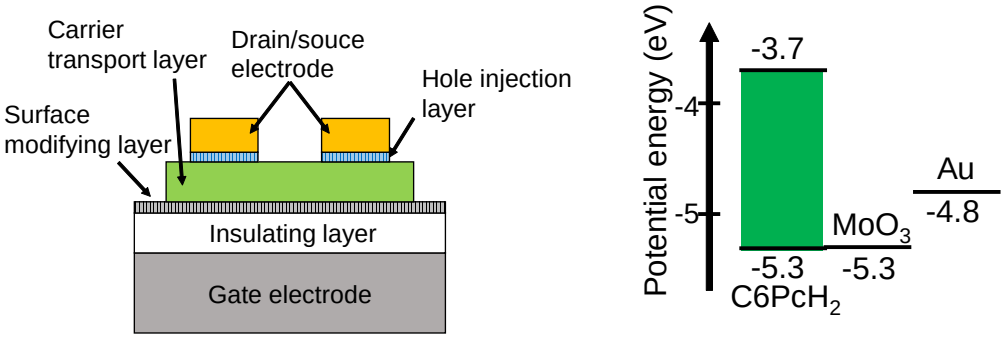

(a) (b)

Fig. 5.1 (a) Schematic structure of a typical bottom gate and top contact type FET. (b) Energy levels of $C6PcH_2$, MoO_3 and Au.

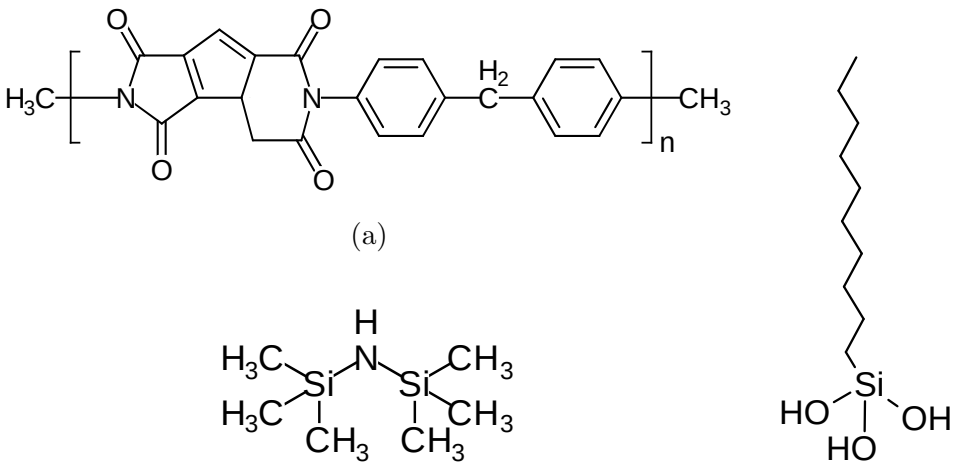

(a) (b) (c)

Fig. 5.2 Molecular structures of (a) polyimide, (b) HMDS, and (c) DTS.

Molecularly oriented films of $C6PcH_2$ were used as carrier transport layers, which were prepared by the following manner. $C6PcH_2$ thin films were fabricated onto the surface modifying layers by a bar-coating technique under air atmosphere. The substrate temperature was maintained at 40 °C. A 9.6-mm-diameter coating-bar, around which a 0.05-mm-diameter metal wire was wound, was fixed on the substrate. $C6PcH_2$ was dissolved in *p*-xylene at a concentration of 10, 20, 40, and 60 g/L, and the solution was added dropwise onto the coating-bar, and then the coating-bar was moved in the horizontal direction at a speed of 30, 120, or 200 μm/s.

A MoO_3 film was deposited onto the $C6PcH_2$ thin film by thermal evaporation at a thickness of 10, 15, 20, 25, or 30 nm as a hole injection layer, and then a 40-nm-thick Au film was deposited

onto the MoO_3 layer by thermal evaporation as a source/drain electrode, and then the devices were completed as shown in Fig. 5.1(a). Thrmal evaporation was carried out under a pressure of approximately 10^{-4} Pa. Figure 5.1(b) shows the energy levels of $C6PcH_2$, MoO_3, and Au. The HOMO level of $C6PcH_2$ is almost equivalent to the work function of MoO_3 [25]. The channel length (L) and channel width (W) were 100 µm and 2 µm, respectively. The channel direction of the FETs was parallel or perpendicular to the sweep direction of the wire-bar.

5.2.2 Measurement setups

The surface free energies of the surface-modified SiO_2/Si and glass substrates were measured by the following manner. First, 4 µL of water or diiodomethane was dropped onto the modified substrate, and the contact angle was measured using the half-angle technique. The surface free energy was calculated by the Owens-Wendt method [80],

$$\gamma_L(1+\cos\theta) = 2\sqrt{\gamma_{\mathrm{S}}^d\gamma_{\mathrm{L}}^d} + 2\sqrt{\gamma_{\mathrm{S}}^h\gamma_{\mathrm{L}}^h}, \tag{5.1}$$

where, γ_{S} and γ_{L} are surface free energies of a modified substrate and solvent, respectively, and superscripts d and h refer to the dispersion force and hydrogen bonding components, respectively. Table 5.1 shows the components of surface free energies of water and diiodomethane [80].

Table 5.1 Components of surface free energy for water and diiodomethane.

	Surface free energy (mN/m)		
	γ_{L}^d	γ_{L}^h	γ_{L}
Water	22.1	50.7	72.8
Diiodomethane	44.1	6.7	50.8

The film thickness of $C6PcH_2$ films was estimated by surface profile measurement with atomic force microscopy (AFM; Keyence VN-8000) and optical absorption measurement by spectrophotometry (Shimadzu UV-3150). Polarizing optical microscopy images and the surface morphology of the thin films were obtained with a polarized optical microscope system (Nikon Eclipse LV100 POL) and an AFM system (Shimadzu Digital Instruments Nanoscope IIIA), respectively.

Transfer and output characteristics of the FETs were measured using a semiconductor pa-

rameter analyzer (Agilent 4155C) under a pressure of approximately 1 Pa at room temperature. The field effect mobility of the C6PcH$_2$ film was evaluated from the transfer characteristics of the FETs by Eq. (1.3).

5.2.3 Surface preparation agent

Table 5.2 summarizes the contact angles of water and diiodomethane on the modified substrates, and surface free energy was calculated using contact angles. The surface free energy of the SiO$_2$/Si substrate without surface modification was the highest at 73.52 mN/m, and that of a polyimide layer was determined to be 57.43 mN/m. In the case of a SiO$_2$/Si substrate without surface modification, the hydrogen bonding component was higher than the dispersion force component; in contrast, for a polyimide layer, the dispersion force component was higher than the hydrogen bonding component. The wettability depends on the surface free energy of the substrate and solvent and was enhanced when the surface free energy of the substrate was close to that of the solvent. The hydrogen bonding component of water is higher than the dispersion force component; therefore, water exhibited good wettability on a SiO$_2$/Si substrate without surface modification, and the dispersion force component of diiodomethane is higher than the hydrogen bonding component; therefore, diiodomethane exhibited good wettability on a polyimide layer.

The surface free energies of the SiO$_2$/Si substrate modified by HMDS and DTS were 33.89 and 35.13 mN/m, respectively, which were lower than those of a SiO$_2$/Si substrate without surface modification or polyimide layer. Water and diiodomethane exhibited poor wettability on the SiO$_2$/Si substrate modified by HMDS and DTS because of the low surface free energy. The surface energy depends on the surface condition of the SiO$_2$/Si substrate, and the terminal functional group of HMDS and DTS is a methyl group. Therefore, the surface free energy of HMDS was considered to be close to that of DTS.

Wettability of the modified substrates was tested for the C6PcH$_2$ films fabricated by the bar-coating method. Figure 5.3 shows the photographs of the C6PcH$_2$ films on various kinds of substrates prepared by bar-coating. The green region represents the C6PcH$_2$ films, and the blue region represents the SiO$_2$/Si substrates. That is, C6PcH$_2$ films could be fabricated on the SiO$_2$/Si substrates without surface modification and modified by a polyimide layer; however, it could not be fabricated on the SiO$_2$/Si substrates modified by DTS and HMDS. As

Table 5.2 Contact angle of water and diiodomethane on modified substrates and components of surface free energy.

	Contact angle (°)		Surface free energy (mN/m)		
	Water	Diiodomethane	γ_S^d	γ_S^h	γ_S
Silicon dioxide	0	37.85	28.93	44.59	73.52
Polyimide	52.94	13.89	41.96	15.48	57.43
HMDS	79.84	55.89	27.20	6.69	33.89
DTS	92.28	48.49	33.96	1.18	35.13

mentioned above, the surface free energy of the SiO_2/Si substrates without surface modification and modified by a polyimide layer was higher than that of the SiO_2/Si substrates modified by DTS and HMDS. Generally, the low surface free energy of the substrate causes poor wettability and suppression of nucleations [81]. In the bar-coating method, the nucleation occurred at the start point of film formation, and crystals grew from the crystalline nucleus. In the case of the SiO_2/Si substrates modified by DTS and HMDS, the nucleation was suppressed, and the C6PcH_2 films cannot be fabricated. The surface state of the SiO_2/Si substrates without surface modification was considered to be unstable because it was difficult to keep the surface clean after ozone cleaning [82]. Therefore, a PVP layer was considered to be suitable as a surface preparation agent, and used as a surface preparation agent in this study.

(a) (b) (c) (d)

Fig. 5.3 Photographs of the samples prepared by bar-coating C6PcH_2 solution on SiO_2/Si substrates (a) without surface modification and modified by (b) polyimide, (c) DTS, and (d) HMDS layers.

5.2.4 Film fabrication conditions

The film thickness depends on the condition of the bar-coating method, such as used solvent, substrate temperature, sweep rate of the wire bar, and concentration of solution. The molecular orientation depends on the film thickness owing to the surface free energy of the substrate [83]. Moreover, the film thickness is considered to affect the carrier transport properties, which can be explained as follows. In the case of a bottom gate and top contact type FET, charge carriers are injected from the electrodes, and transported in the carrier transport layer near a SiO_2 layer. Thus, the carrier transport from the top side to the bottom side of the carrier transport layer, i.e., the carriers were transported in the thickness direction. C6PcH$_2$ tends to form a columnar structure, and uniaxially high carrier transport properties were observed along the column axis. Assuming uniaxially planar oriented thin films of C6PcH$_2$, the column axis of which is parallel to the channel direction of an FET, the channel direction is parallel to the column axis when the thickness direction is perpendicular to the column axis. The carrier transport properties were considered to be limited by the conduction along the thickness direction. Therefore, thin and uniaxially oriented films of C6PcH$_2$ are suitable for FET application.

In this study, C6PcH$_2$ films with various film thicknesses were fabricated by controlling the film fabrication conditions, such as sweep rate of the wire bar and concentration of solution. Figure 5.4 shows solution concentration dependence of the film thickness of C6PcH$_2$. The film thickness linearly increased depending on the solution concentration at any sweep rate, and the proportionality factors between the film thickness and the solution concentration were calculated to be 2.92, 0.71, and 0.44 nmL/g for the sweep rates of 30, 120, and 200 mm/s, respectively. The proportionality factors were inversely proportional to the sweep rate of the wire bar, i.e., the film thickness is proportional to the fabrication time.

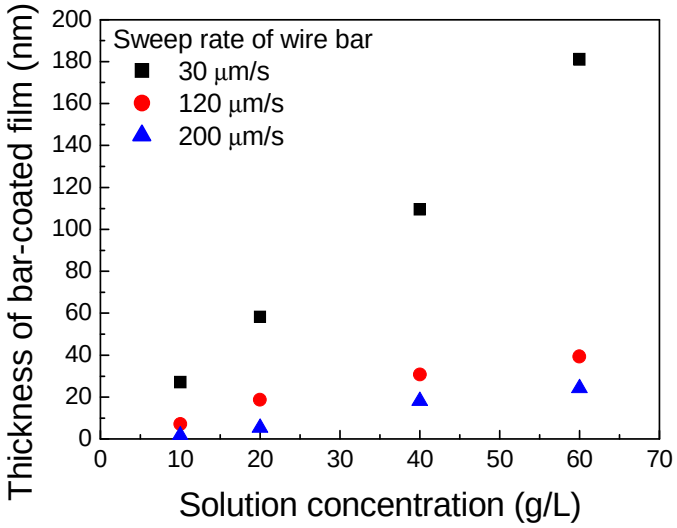

Fig. 5.4 Solution concentration dependence of the film thickness of C6PcH$_2$ at various sweep rates of the wire-bar.

Molecular alignment in the film was investigated by polarized optical and atomic force microscopy. The uniaxially planar oriented thin films of C6PcH$_2$ were obtained when the film was thicker than 20 nm; the detailed data are given in the Appendix. As mentioned above, thin and uniaxially oriented films of C6PcH$_2$ are suitable for the FET application; therefore, a solution concentration of 60 g/L and a sweep rate of 200 mm/s are appropriate conditions for FET application.

Figure 5.5 shows the typical polarized optical microscopy images of the thin film prepared by bar-coating, which were observed with crossed polarizers. These images were uniformly dark and bright at the extinction and diagonal positions, respectively, which indicates that a uniform and uniaxial molecular oriented thin film was obtained in an area of approximately 1 mm^2. As shown in the bright image at the diagonal position, some lines almost parallel to the coating-bar sweep direction were observed. The lines were considered to be caused by the domain boundaries, resulting in the sub-mm-wide domains in the thin films. In the domains, short-line patterns perpendicular to the coating-bar sweep direction were also observed. It is considered that these line patterns were formed by the volumetric shrinkage along the column axis during solvent evaporation.

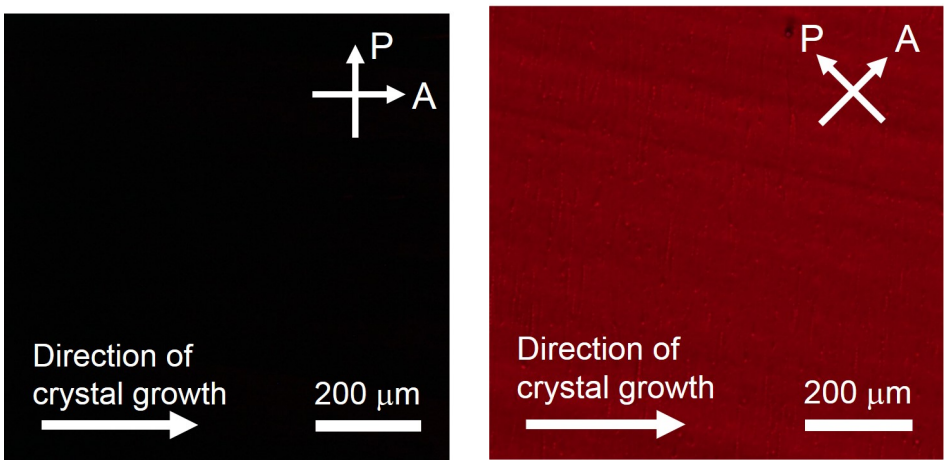

(a) (b)

Fig. 5.5 Polarized optical microscopy images of the thin film observed with crossed polarizers in (a) extinction and (b) diagonal positions.

The AFM image and surface profile of the C6PcH$_2$ thin film are shown in Fig. 5.6(a). The bright and dark regions existed in the AFM image, and each surface seems to be flat in the profile. That is, the terrace and step morphology appeared on the film surface. A similar surface structure was reported for the single crystals of organic molecules [64]. In order to estimate the step height, the statistical distribution of the height value was analyzed from Fig. 5.6(a). As shown in Fig. 5.6(b), two peaks, which should correspond to the upper and lower terraces, could be found, and the average step height was evaluated to be approximately 1.71 nm. The value of the average step height corresponded to the lattice spacing of the (002) plane (1.80 nm) in β-type C6PcH$_2$, which agreed with the molecular packing structure in the bar-coated thin film measured by the GIWAXS technique, as shown in Fig. 4.5.

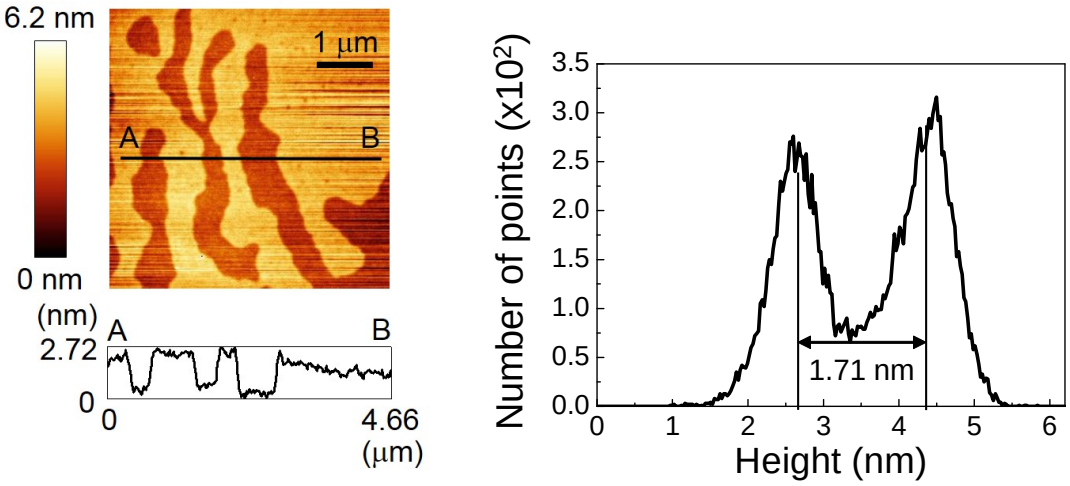

(a) (b)

Fig. 5.6 (a) AFM image and surface profile of the thin film of $C6PcH_2$. The profile corresponds to the black line in the image. (b) Statistical distribution of height value for Fig. 5.6 (a).

5.2.5 Hole injection layer

The thickness of the hole injection layer was optimized by the FET measurement. The channel direction of the FETs was parallel to the sweep direction. Figures 5.7(a)–(c) show the output and transfer characteristics of the FETs with various thicknesses of the MoO_3 layer. For the FET without any MoO_3 layer, the transfer and output characteristics could not be measured because of the high energy barrier between the Au electrodes and $C6PcH_2$ layer as shown in Fig. 5.1(b).

In the transfer characteristics, the value of the square root of the drain current (I_D) at -50 V of drain voltage (V_D) was plotted against the various gate voltage, while the drain current at -50 V of gate voltage (V_G) was plotted against the various drain voltage in the output characteristics. As shown in Fig. 5.7(a), the drain current was saturated at approximately -30 V, regardless of the thickness of MoO_3. The linear characteristics of I_D-V_D at a low drain voltage were obtained owing to the low energy barrier between the $C6PcH_2$ and MoO_3 layers as shown in Fig. 5.1(b). The saturation characteristics implied typical behaviors of p-channel FETs in the accumulation mode. The saturated drain currents at -50 V were -0.39, -0.85, -1.21, -0.99, and -0.67 μA when the thickness of the MoO_3 layer were 10, 15, 20, 25, and 30 nm, respectively, i.e., the highest drain current was observed when the thickness of the MoO_3 layer was 20 nm.

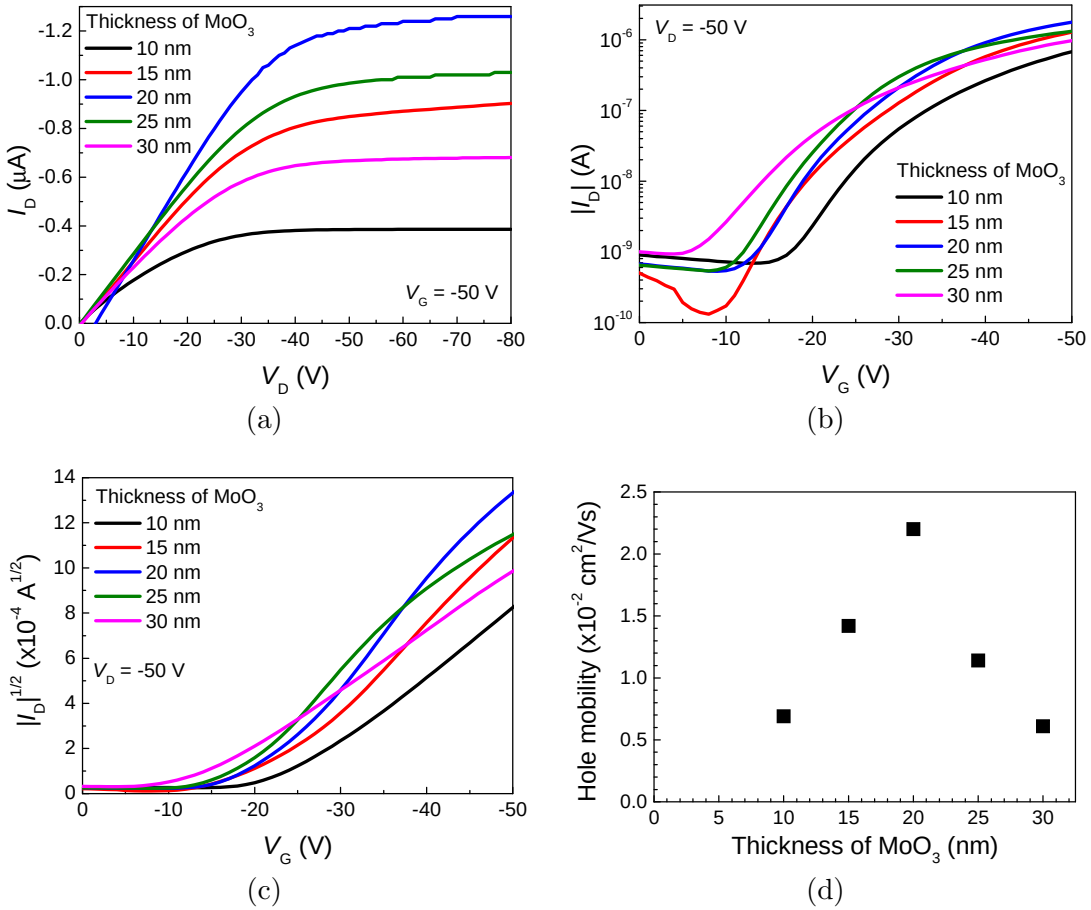

Fig. 5.7 MoO_3 thickness dependence of (a) output and transfer characteristics of FETs on (b) a semi-log scale and (c) square root of the same data on a liner scale. (d) Hole mobilities of FETs with the uniaxially planar oriented thin films of C6PcH$_2$ as a function of MoO_3 thickness.

As shown in Fig. 5.7, the drain current increased as the gate voltage increased. The on/off current ratio was estimated to be 10^2–10^3, and the hole threshould voltages were determined to be -22.6, -21.3, -20.5, -17.2, and -12.3 V when the thicknesses of the MoO_3 layer were 10, 15, 20, 25, and 30 nm, respectively, i.e., the hole threshould voltage decreased as the thickness of the MoO_3 layer increased. The result indicated that smooth hole injection from the electrode occurred as the thickness of the MoO_3 layer increased.

Figure 5.7(d) shows the hole mobilities of FETs with the uniaxially planar oriented thin films of C6PcH$_2$ as a function of MoO_3 thickness calculated by Eq. (1.3). The hole mobilities were calculated to be 6.9×10^{-3}, 1.4×10^{-2}, 2.2×10^{-2}, 1.1×10^{-2}, and 6.1×10^{-3} cm^2/Vs when the thicknesses of the MoO_3 layer were 10, 15, 20, 25, and 30 nm, respectively, i.e., the highest hole mobility was observed when the thickness of the MoO_3 layer was 20 nm. The resistance of

MoO_3 increased as the thickness of the MoO_3 layer increased, and the carrier mobility of FET was estimated to be lower than the essential mobility of the thin film. As mentioned above, the increase in the thickness of MoO_3 induced smooth hole injection from the electrode. Therefore, the suitable thickness of MoO_3 was determined to be 20 nm

5.2.6 Measurement of electrical anisotropy

The relationship between the hole transport and structural anisotropy in the C6PcH_2 films was investigated. Figure 5.8 shows the POM image of FET observed with crossed polarizers in the diagonal position. The channel direction is perpendicular to the crystal growth direction of C6PcH_2. Uniform color of the planar oriented films was observed, which indicated that uniformly oriented thin films were fabricated. Figure 5.9 shows the output and transfer characteristics of the FETs, the channel direction of which was parallel or perpendicular to the column axis of C6PcH_2. In the transfer characteristics, the value of the square root of the drain current at -50 V of the drain voltage was plotted against different gate voltages, while the drain current at -50 V of the gate voltage was plotted against various drain voltages in the output characteristics. As shown in Fig. 5.9(a), the drain currents parallel and perpendicular to the column axis were saturated at approximately -40 V and -30 V of the drain voltages, respectively. Both FETs exhibited linear characteristics of I_D-V_D at the low drain voltage because of smooth hole injection from the source electrode owing to the low hole barrier as shown in Fig. 5.1(b). The saturation characteristics of both devices implied typical behaviors of p-channel FETs in the accumulation mode. As shown in 5.9(b), the drain current increased as the gate voltage swept from 0 V to -50 V regardless of the direction of the molecular orientation, which indicates the typical p-type behavior of FET. The on/off current ratio was estimated to be more than 10^3 and the hole threshold voltage of the two devices was approximately -20 V.

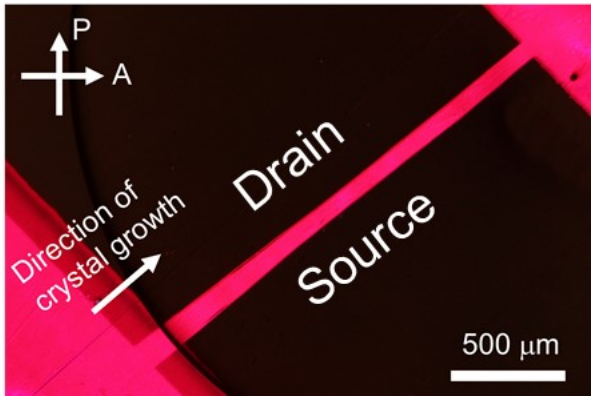

Fig. 5.8 Polarized optical microscopy image of the transistor observed with crossed polarizers in diagonal position. The channel direction is perpendicular to the crystal growth direction of C6PcH$_2$.

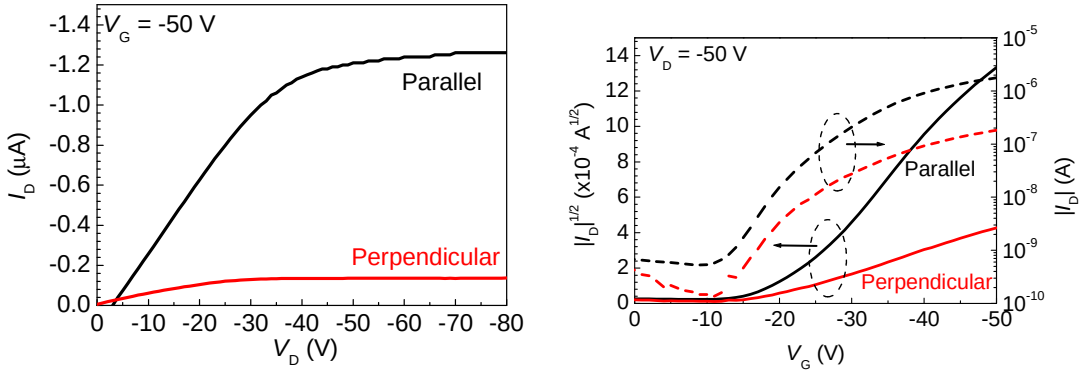

(a) (b)

Fig. 5.9 (a) Output characteristics of FETs. (b) Transfer characteristics of FETs on a semi-log scale (dotted line) and the square root of the same data on a liner scale (solid line). The channel direction was parallel (black line) or perpendicular (red line) to the column axis of C6PcH$_2$.

Similar measurements were carried out for 18 and 23 transistors, the channel directions of which were parallel and perpendicular to the column axis of C6PcH$_2$, respectively, and the field effect mobility was calculated by Eq. (1.3). Figure 5.10 shows the histogram plots of the field effect mobility parallel and perpendicular to the column axis. 95% confidence intervals of the mobilities parallel and perpendicular to the column axis were $(1.54 \pm 0.24) \times 10^{-2}$ and $(2.10 \pm 0.23) \times 10^{-3}$ cm^2/Vs, respectively. The hole mobility parallel to the column axis in the molecular oriented thin films was approximately 7 times higher than that perpendicular to the column axis. According to the single crystal X-ray structure analysis of β-type C6PcH$_2$ at 273

K, as shown in Figs. 2.4(c) and (d), the intermolecular distance along the column axis is 3.644 Å and the intercolumn distance is approximately 20 Å. Therefore, the π-π interaction parallel to the column axis of $C6PcH_2$ is expected to be stronger than that perpendicular to the column axis.

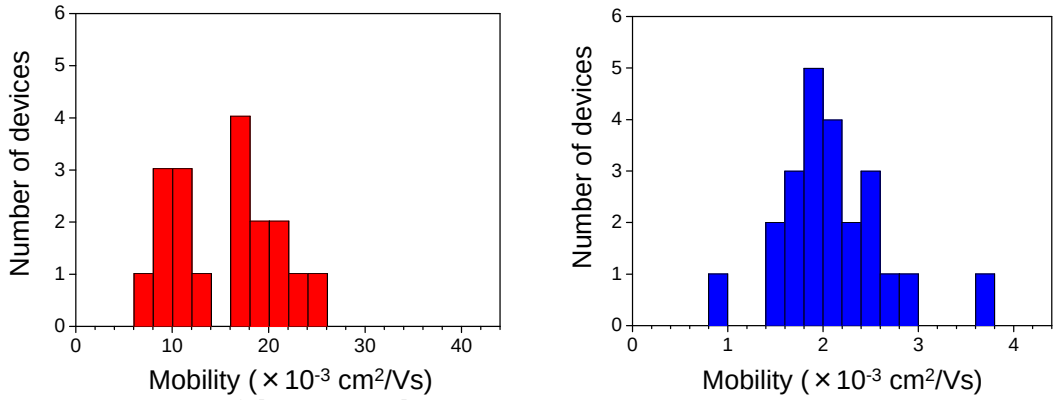

(a) (b)

Fig. 5.10 Histgram plots of the field effect mobility (a) parallel and (b) perpendicular to the column axis of $C6PcH_2$ for 18 and 23 transistors, respectively.

The electrical anisotropy of HBC derivatives, which are discotic LC materials, has been reported, and the mobility parallel to the column axis was two orders of magnitude higher than that perpendicular to the column axis [32], [41]. That is, the electrical anisotropy of HBC derivatives was higher than that of $C6PcH_2$. The alkyl chains and intercolumn distance of HBC derivatives were longer than those of $C6PcH_2$; therefore, the π-π interaction along the intercolumn direction of HBC derivatives is considered to be weaker than that of $C6PcH_2$.

5.3 Solar cells utilizing homeotropically oriented thin films

5.3.1 Sample fabrication method

A solar cell with the molecularly oriented thin film was fabricated by the following way. An indium-tin-oxide (ITO)-coated glass substrate was cleaned with an alkaline solution and water by ultrasonication and then treated with UV-ozone. A 6-nm-thick MoO_3 film was thermally evaporated onto an ITO-coated glass substrate at a rate of 0.1 Å/s as a hole transport layer under a vacuum of about 10^{-4} Pa. $C6PcH_2$ of 42.8 mg and PCBM (Frontier carbon) of 3.64 mg were dissolved in 1mL chloroform, which indicates that the molar ratio of $C6PcH_2$:PCBM was

9:1. Figure 5.11 shows the molecular structure of PCBM. In the sandwich-cell type solar cells with the C6PcH_2:PCBM bulk heterojunction layer, the highest power conversion efficiency was obtained at the same molar ratio of C6PcH_2:PCBM [72]. The C6PcH_2:PCBM mixed solution was spin-coated onto the MoO_3 layer in a glove-box filled with nitrogen gas. The film thickness was estimated to be approximately 400 nm by the surface profilometer. A 160-nm-thick PVP layer was spin-coated onto a C6PcH_2:PCBM layer. The sample was annealed at 165 °C in the isotropic phase of a blended film of C6PcH_2 and PCBM for 1 min, and then rapidly cooled down to room temperature. In order to remove the PVP layer completely, methanol was spin-casted four times onto a sample at the speed of 3000 rpm. An 80-nm-thick aluminum layer as a counter electrode to the ITO electrode was deposited onto the active layer through a shadow mask by thermal evaporation under a pressure of approximately 10^{-4} Pa. The active areas of the solar cells were 2×2 mm^2.

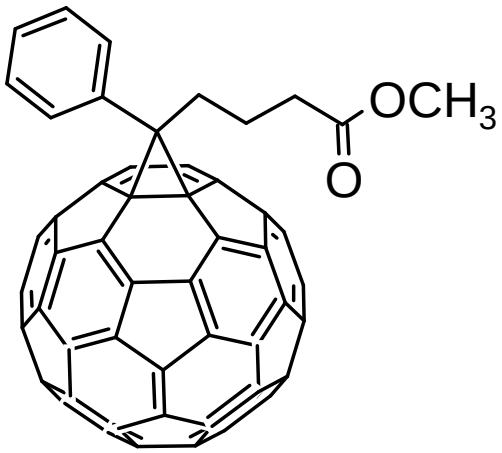

Fig. 5.11 Molecular structure of PCBM.

5.3.2 Measurement setups

The charge carrier mobility in the solar cells was determined by a photo-induced charge carrier extraction by linearly increasing the voltage (Photo-CELIV) in a vacuum at room temperature. The synchronized beam of a Q-switched Nd:YAG pulsed laser (CryLaS FTSS355-50) was irradiated from the ITO-layer side of the solar cells. The wavelength, pulse width, and pulse repetition rate of the laser were 355 nm, 1 ns, and 20 Hz, respectively. Triangle pulses in reverse bias were

applied between the electrodes using a function generator (Hewlett Packard 8112A). The delay time between the laser radiation and voltage impression was 4 µs, and the magnitude of the applied voltage changed from 0 to 3 V in 10 µs. The generated transit current was recorded using a digital oscilloscope (Teledyne LeCroy HDO4054). The carrier mobility μ was calculated using the following equation [84].

$$\mu = \frac{2d^2}{3At_{\max}^2\left[1 + 0.18\frac{\Delta J}{J(0)}\right]}, \tag{5.2}$$

where, d is the thickness of the active layer, A is the voltage rise speed, $t_{\max}$ is the time to reach the extraction current maximum, $J(0)$ is the capacitive displacement current, and ΔJ is difference between the maximum current and $J(0)$. The delay time between the laser radiation and voltage impression was changed from 0.2 µs to 14 µs and the charge recombination rate during transport of the solar cell was also estimated. The number of collected charges $n(t)$ was calculated by using the effective bimolecular lifetime τ_B as follows [85], [86],

$$n(t) = \frac{n(0)}{(1 + t/\tau_B)^{\gamma}}, \tag{5.3}$$

where, γ is a time-independent parameter.

The absorbance spectrum was measured using a spectrophotometer (Shimadzu UV-3150). The current density-voltage characteristics (J-V) were measured using a source meter (KEITHLEY 2400) and full spectrum solar simulator (Bunkoukeiki OTENTO-SUN IIIP2) at a 100 mW/cm^2 irradiation intensity (AM1.5G). The external quantum efficiency (EQE) spectra were measured using a photosensitivity measurement system (Bunkoukeiki SM-250NA) with xenon lamp light passing through a monochromator as a light source. The J-V characteristics and EQE spectrum were measured in vacuum at room temperature.

5.3.3 Carrier transport properties

In order to investigate the effect of the homeotropic alignment for the electrical properties, the carrier mobility in the C6PcH$_2$:PCBM blended thin films of the solar cell structures was estimated by using the photo-CELIV method. Figure 5.12 shows the transient current wave forms of the C6PcH$_2$:PCBM blended thin films with and without the homeotropic alignment process.

The typical transient current in the photo-CELIV method, which consisted of a capacitive component and a photo-generated component, was observed. In the case without the homeotropic alignment process, the time to reach the extraction current maximum t_{max} was 3.02 µs, and the carrier mobility was calculated to be 1.16×10^{-3} cm^2/Vs by using Eq. (5.2). In contrast, t_{max} was 0.60 µs with the homeotropic alignment process, and the carrier mobility was calculated to be 4.31×10^{-2} cm^2/Vs. The carrier mobility in the thin film enhanced by 37 times through the homeotropic alignment process. For the device configuration used in this study, the carrier transport properties perpendicular to the substrate could be measured by the photo-CELIV method; therefore, it is considered that the mobility enhancement was based on the carrier transport along the column axis of $C6PcH_2$.

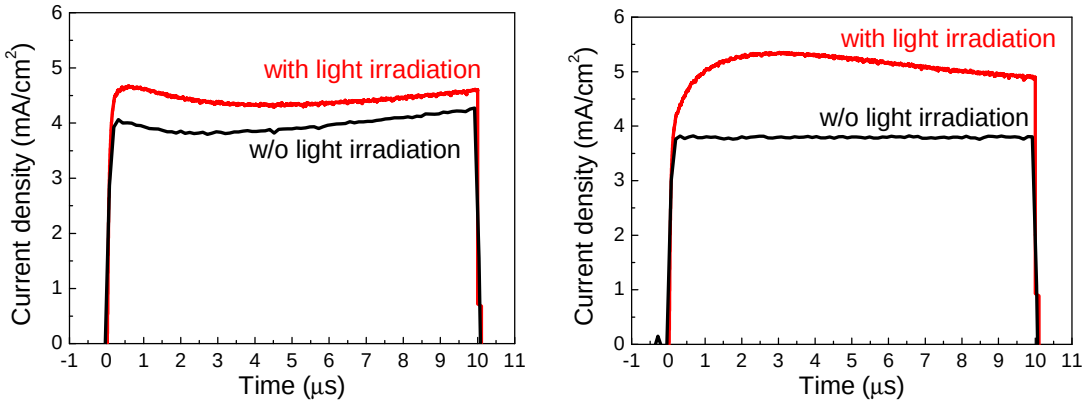

Fig. 5.12 Photo-CELIV curves of the solar cells (a) with and (b) without the homeotropic alignment process. The red and black lines represent the transient current density waveforms with and without light irradiation, respectively.

The life time of the carriers was also measured by the photo-CELIV method. Figure 5.13 shows the number of collected charges as a function of the delay time between the laser radiation and voltage impression of the solar cells with and without the homeotropic alignment process. The number of collected charges was estimated by integration of the difference between the transient current of the $C6PcH_2$:PCBM blended thin films, with and without light pulse. The plots indicated the measurement results with and without the homeotropic alignment process. In the case with the homeotropic alignment process, $n(0)$, τ_B, and γ in Eq. (5.3) were calculated to be 1.79×10^{15} cm^{-3}, 2.63 µs, and 1.07 by the least squares method, respectively. In the case without the homeotropic alignment process, $n(0)$, τ_B, and γ were calculated to be 3.48×10^{15}

cm^{-3}, 5.31 μs, and 1.14, respectively. The fitting lines were displayed as solid lines in Fig. 5.13, and show good agreement with the experimental data.

The number of the collected charges in the case with the homeotropic alignment process was lower than that without the homeotropic alignment process. This can be explained by the low exciton dissociation efficiency. The $C6PcH_2$:PCBM blended thin films were annealed at the temperature of the LC phase in the homeotropic alignment process. Large domains of $C6PcH_2$ are formed in the LC phase, and decrease the domain boundary. Charge carriers were generated at the domain boundary between $C6PcH_2$ and PCBM. As described in Section 1.2.5, probability of the arrival of the exciton at the boundary between the donor and acceptor materials depend on the area of the boundary, and the probability affect the number of the charge carriers. Therefore, the low generated charge carriers were obtained in the case with the homeotropic alignment process.

Life time in the case with the homeotropic alignment process was shorter than that without the homeotropic alignment process. The life time of carriers largely depend on the carrier diffusion length, and carrier diffusion length (L) can be calculated by the equation $L = \sqrt{k_B T \mu \tau_B / q}$; k_B and q are Boltzmann's constant and elementary charge, respectively. From this equation, the carrier diffusion length was determined to be proportional to the square root of the carrier mobilities; therefore, short life time in the case with the homeotropic alignment was considered to be caused by the high carrier mobility.

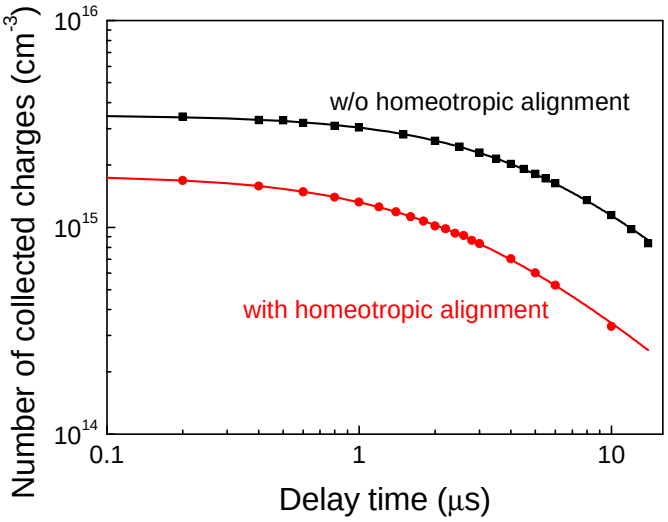

Fig. 5.13 Number of collected charges as a function of the delay time between the laser radiation and voltage impression of the solar cells. The red and black plots indicate the measurement results in the cases with and without the homeotropic alignment process, respectively. The red and black lines indicate the fitting lines of the red and black plots by Eq. (5.3), respectively.

5.3.4 Photovoltaic properties

Figure 5.14 shows the absorption spectra of the C6PcH$_2$:PCBM blended films with and without the homeotropic alignment process. The absorption peaks in the wavelength ranges of 300-400 and 600-800 nm, called B and Q band, respectively, were similar to those of the conventional non-substituted Pcs [87]. Without the homeotropic alignment process, the absorption spectrum almost coincides with that of the C6PcH$_2$:PCBM blended film reported previously. The absorption spectrum of the C6PcH$_2$:PCBM blended film after the homeotropic alignment process exhibited a slight difference from that without the homeotropic alignment process. The shoulders around 400 and 760 nm, corresponding to the absorption edges of the B and Q bands, respectively, appeared, and the spectral shapes of the B and Q bands became broader. Such a spectral change, which must be caused by the directional changes of the molecular plane or column axis of C6PcH$_2$, is one of the effects of the optical properties.

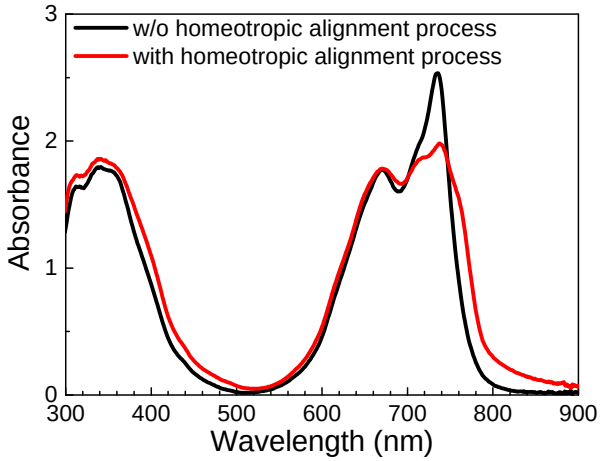

Fig. 5.14 Absorption spectra of C6PcH$_2$:PCBM blended spin-coated thin films. The red and black lines indicate the cases with and without the homeotropic alignment process, respectively.

Figure 5.15 (a) shows the J-V characteristics of the solar cells with and without the homeotropic alignment process. Without the homeotropic alignment process, the device performance seemed to be low, and the short-circuit current density (J_{sc}) and fill factor (FF) were especially quite low at 0.11 mA/cm^2 and 0.116, respectively. Using the homeotropic alignment process, the device performance markedly enhanced. That is, the J_{sc} and FF values increased to be 1.07 mA/cm^2 and 0.345, respectively, and the power conversion efficiency was calculated to be 0.30% owing to the open-circuit voltage of 0.816 V. In the spectra of the external quantum efficiency as shown in Fig. 5.15 (b), the efficiency not only enhanced, but the spectral width also became broader. Since the shoulders around the absorption edges for the B and Q bands appeared as shown in Fig. 5.14, the photo-current generated by light irradiation at the corresponding wavelengths of around 400 and 760 nm markedly enhanced. The enhancement in J_{sc} could be explained by the improved efficiency due to the increased carrier mobility and the broadened wavelength range for photo-sensitivity. Although the carrier mobility seems easy to understand, the detailed mechanism is still not clear at this stage, because the carrier species, holes or electrons, could not be distinguished in the mobility measurement. It is supposed, however, that the carrier balance of the holes and electrons might be improved by considering the mobility enhancement in the solar cells.

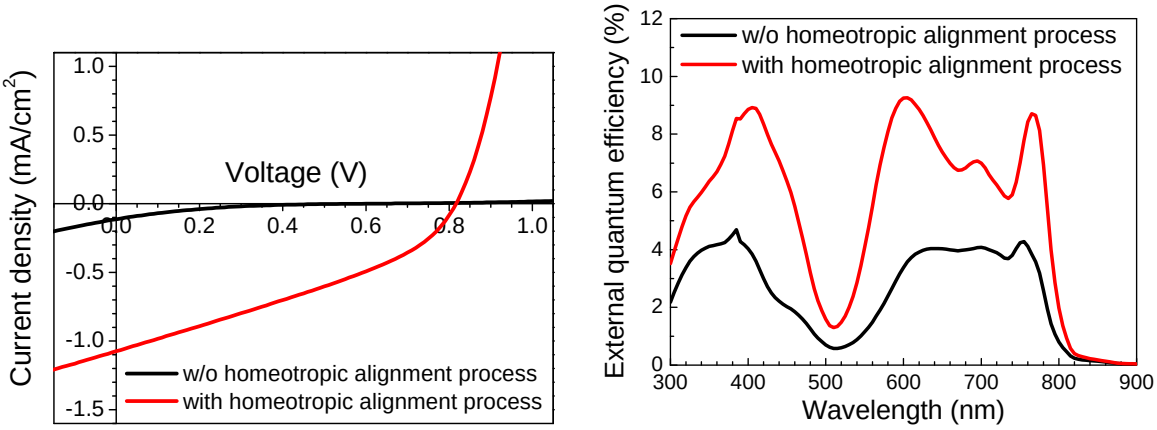

(a) (b)

Fig. 5.15 (a) Current density-voltage characteristics of solar cells under the AM1.5G (100 mW/cm^2) solar-illuminated condition and (b) EQE spectra of the solar cells. The red and black lines indicate the cases with and without the homeotropic alignment process, respectively.

5.4 Discussion

The electrical anisotropy of C6PcH$_2$ was clarified by the FET measurement. The mobility values parallel and perpendicular to the column axis were estimated to be (1.54±0.24)×10^{-2} and (2.10±0.23)×10^{-3} cm^2/Vs, respectively. In the films prepared by bar-coating, the β-type crystals were fabricated. The mobility parallel and perpendicular to the column axis of C6PcH$_2$ β-type crystals was simulated to be 1.486, 3.8×10^{-5} cm^2/Vs by the DFT calculation, as mentioned in Chapter 2. Besides, hole mobility of 1.4 cm^2/Vs was evaluated by the time-of-flight (TOF) measurement [23].

The marked electrical anisotropy of C6PcH$_2$ was found by the transistor measurement as mentioned above; however, the field effect mobility along the column axis was approximately 10^2 times lower than the mobility obtained by the DFT calculation and TOF measurement, which is a problem to be solved. For the DFT calculation, the ideal hopping conduction along the column axis was assumed. Furthermore, in the case of the TOF measurement, the arrival time of the charge carrier to the counter electrode was measured when the fastest carrier path was measured. In the case of the FET measurement, the current density was strongly related with the mobility, but the average charge mobility in the FET devices was measured. Hence, the carrier mobility of FETs was affected by various factors, such as injection resistance from the electrode to organic layer, and structural defects. In the micrograph shown in Fig. 5.5(b),

many short-line patterns exist. These patterns in the thin film might be structural defects such as cracks, which may disturb the carrier transport parallel to the column axis. The cracks were considered to be caused by a mismatch between the crystal growth rate and sweep speed; therefore, the optimization of the film fabrication conditions was considered to be essential.

The field effect mobility perpendicular to the column axis was approximately 10^2 times higher than the simulated mobility. An orientational disorder of $C6PcH_2$ might occur around the interface between the polyimide and the $C6PcH_2$ layer, and the entire column axis of $C6PcH_2$ was not completely perpendicular to the channel direction, resulting in the carrier transport route between the electrodes.

The effects of homeotropic alignment of $C6PcH_2$ in the thin film should be useful for the solar cell applications, and were actually exhibited in the optical and electrical properties as mentioned above. At this stage, the power conversion efficiency of the solar cell with the homeotropically oriented thin film was still low, which is also a problem to be solved. One of the reasons for this phenomenon the blend ratio of $C6PcH_2$:PCBM. The optimized molar ratio of PCBM for the $C6PcH_2$-based bulk-heterojunction solar cells was reported to be about 40 mol% [52]. Though the annealing temperature dependence of the photovoltaic properties was also reported at the blend ratio of 40 mol% [78], the device performance deteriorated in the annealing process at higher than 75 °C due to excessive phase separation resulting from the large domain formation. Moreover, in the case of 40 mol%, the LC phase could not be found in the thermal measurement of a mixture of $C6PcH_2$ and PCBM, such as differential scanning calorimetry, unlike the case of 10 mol% [72], [88]; therefore, the thermal treatment at 165 °C disordered the molecular alignment instead. At the PCBM molar ratio of 10 mol% adopted in this study, the LC phase appears between 135 and 153 °C in the cooling process, and the molecular alignment was maintained in the fast cooling process as mentioned above; however, the balance of the hole and electron mobilities should be improved.

For realizing the high performance of the $C6PcH_2$-based thin-film solar cells with the homeotropic alignment, control of the phase separation of the donor and acceptor materials is essential. Interpenetrating heterojunction type organic solar cells might be one of the ways to control the phase separation [89], [90], [91]. Two types of materials, which exhibit high and low solubility in an organic solvent, are needed for the fabrication of interpenetrating heterojunction films. $C6PcH_2$ exhibits low solubility in diiodeoctane (DIO) solvent, while PCBM exhibits high solubil-

ity; therefore, interpenetrating heterojunction films of C6PcH$_2$ and PCBM should be fabricated. By using this process, the phase separation in the C6PcH$_2$ thin film is controlled, and the solar cell properties is assumed to be enhanced.

5.5 Conclusions

FETs with the molecularly oriented thin film of C6PcH$_2$ were fabricated, and the electrical anisotropy of C6PcH$_2$ was investigated. Fabrication conditions of the FETs, such as surface modifying layers, carrier transport layers, and hole injection layers, were optimized. The uniform thin film of C6PcH$_2$ prepared by the bar-coating technique exhibited uniaxially optical properties in an area of approximately 1 mm^2, and step-terrace structures were found on the film surface. The field effect mobility parallel and perpendicular to the column axis of C6PcH$_2$ were determined to be $(1.54\pm0.24)\times10^{-2}$ and $(2.10\pm0.23)\times10^{-3}$ cm^2/Vs, respectively, and it was clearly demonstrated that the hole transport along the column axis of C6PcH$_2$ was predominant in the thin film. The carrier mobility of C6PcH$_2$ was compared with the simulated carrier mobility by DFT calculation, and the electrical anisotropy was ascertained to be consistent with the experimental results.

The homeotropic alignment of C6PcH$_2$ in the thin film was realized by the thermal treatment of the C6PcH$_2$:PCBM blended thin film covered with the PVP layer. The bulk-heterojunction solar cell utilizing the homeotropically oriented thin film was fabricated, and the carrier transport and photovoltaic properties were investigated. Introducing the homeotropic alignment process, the carrier mobility in the thin film and the solar cell properties were enhanced. The homeotropic alignment process was effective for C6PcH$_2$-based solar cell applications.

Chapter 6.

Conclusions

In this dissertation, the molecular alignment control of the columnar liquid-crystalline (LC) materials, $C6PcH_2$, and crystal structure analysis in the molecularly oriented thin films were investigated. The important realizations from each chapter can be summarized as follows.

Chapter 2 describes the fabrication of the single-crystals of $C5PcH_2$, $C6PcH_2$, and $C6TBTAPH_2$ and the crystal structure was clarified by the single-crystal X-ray structure analysis. Two types of crystal polymorph of $C5PcH_2$, $C6PcH_2$, and $C6TBTAPH_2$, called α-type and β-type crystals, were clarified to exist, and the thermal phase transition from the α-type to β-type crystals was observed. The stability of the crystal polymorphs was discussed by taking the Gibbs' free energy into consideration, and the selective crystal growth of the crystal polymorphs was realized. Moreover, the carrier mobility was simulated by the density functional theory calculation, and it was clarified that α-type crystals of $C5PcH_2$ and $C6PcH_2$ exhibit high carrier mobility. Though devices utilizing the α-type crystals of $C5PcH_2$ and $C6PcH_2$ have not been reported, the high device performance is predicted by using the α-type crystals of $C5PcH_2$ and $C6PcH_2$.

In Chapter 3, molecular packing structures in the spin-coated thin films of $C5PcH_2$, $C6PcH_2$, and $C10PcH_2$ were investigated by the grazing incidence wide-angle X-ray scattering (GIWAXS) technique. The column structures of $C5PcH_2$, $C6PcH_2$, and $C10PcH_2$ were maintained in the spin-coated films, and the planar orientation of the columns was induced in the spin-coated films. The molecular packing structures of $C5PcH_2$ and $C6PcH_2$ were determined to be a centered rectangular structure, and that of $C10PcH_2$ was determined to be a rectangular structure. Additionally, the lattice constants and tilt angles of the Pc cores in the columns of $C5PcH_2$, $C6PcH_2$, and $C10PcH_2$ were determined. The assumed molecular packing structures were ascertained to be consistent with those calculated by Fourier analysis.

In Chapter 4, the molecular alignment control of $C6PcH_2$ in the thin films was investigated.

First, the uniaxially planar oriented thin films of C6PcH$_2$ were fabricated by the bar-coating method, and uniaxially planar orientation in the thin films was confirmed by the polarized and atomic force microscopy. Additionally, its three-dimensional crystal structure was clarified by the GIWAXS technique with a sample rotation. The molecular packing structure in the thin film coincided with that of the β-type C6PcH$_2$ single-crystal, and the column axis of C6PcH$_2$ was clarified to be parallel to the crystal growth direction. Moreover, the XRD patterns were simulated by the crystal structure obtained by single-crystal X-ray analysis, and the difference between the measurement and simulated result was calculated. The simulation process of the detailed molecular packing structure utilizing the difference was proposed and the effectiveness of the GIWAXS measurement utilizing a uniaxially oriented thin film was indicated.

Secondly, a C6PcH$_2$ film was covered with a polymer layer, and the homeotropic alignment of C6PcH$_2$ in the thin films was induced by the thermal treatment through the LC phase. Additionally, the molecular alignment in the thin film was clarified by the GIWAXS technique. The homeotropic alignment was induced in the LC phase, and the molecular alignment was maintained at room temperature in the crystal phase.

In Chapter 5, field-effect transistors (FETs) and solar cells utilizing the molecular oriented thin films of C6PcH$_2$ were fabricated, and the carrier transport and solar cell properties were investigated. First, the fabrication conditions of the FETs, such as surface modifying, carrier transport and hole injection layers, were optimized, and FETs utilizing the uniaxially planar oriented thin films were fabricated, and the electrical anisotropy of C6PcH$_2$ was investigated. The field effect mobilities, parallel and perpendicular to the column axis of C6PcH$_2$ were determined to be $(1.54\pm0.24)\times10^{-2}$ and $(2.10\pm0.23)\times10^{-3}$ cm^2/Vs, respectively, and the hole transport along the column axis of C6PcH$_2$ was indicated to be predominant in the thin film. Secondly, solar cells utilizing the homeotropically oriented thin films was fabricated, and the carrier transport and solar cell properties were investigated. The carrier mobility and solar cell properties were enhanced by inducing the homeotropic alignment, and homeotropic alignment process was effective for the C6PcH$_2$-based solar cell applications.

The molecular orientation control was carried out by using the unique properties of the columnar LC materials. For the fabrication of the uniaxially planar orientated thin film, the relatively high crystal growth rate along the column axis was used, and the column axis was parallel to the crystal growth direction. For the fabrication of the homeotropically oriented thin

film, the homeotropic alignment in the LC phase was used, and the molecular alignment was maintained after the cooling process. Owing to clarification of the molecular packing structure in these highly oriented thin films, development of an analysis process for the detailed three-dimensional (3-D) molecular packing structure is essential. The detailed 3-D molecular packing structure in the highly oriented thin films was determined by the GIWAXS technique with a sample rotation.

In conclusion, molecular alignment control in the thin films utilizing columnar LC semiconductors and clarification of the detail crystal structure in the molecularly oriented thin films were realized.

Acknowledgements

First of all, I would like to express my greatest gratitude to my supervisor Professor Masanori Ozaki, for his invaluable advice, guidance, and support during my Ph.D study. My Ph.D. dissertation would not have been completed without his guidance. Many thanks are also due to Associate Professor Akihiko Fujii, who has always instructed and guided me in my research area and he always gave me many useful suggestions. I could not have carried out my research without his support. I am also thankful to Assistant Professor Hiroyuki Yoshida for his perceptive comments and advice.

I would also like to extend my gratitude to all of the professors at the Division of Electrical, Electronic and Information Engineering Osaka University. I especially thank Professor Yusuke Mori and Associate Professor Norimitsu Tohnai for reviewing this dissertation. I am also grateful to Professor Toshimichi Ito, Professor Mitsuhiro Katayama, Professor Ryuji Katayama, Professor Masahiko Kondow, Professor Nobuya Mori, and Professor Tetsuya Yagi for serving on my dissertation committee.

I also would like to extend my gratitude to Associate Professor Hirotake Kajii and Assistant Professor Hitoshi Kubo of Osaka university; Dr. Makoto Yoneya and Dr. Yuji Yoshida at the National Institute of Advanced Industrial Science and Technology (AIST); Prof. Itaru Osaka in Hiroshima University; Prof. Yo Shimizu and Prof. Masakazu Nakamura in Nara Institute of Science and Technology; Dr. Tomoyuki Koganezawa in Japan Synchrotron Radiation Research Institute (JASRI), and temporary staffs Dr. Toshiya Kamikado and Mr. Hiromichi Itani.

I would also like to thank Ozaki Laboratory members and alumni Dr. Giichi Shibuya, Dr. Tetsuro Hori, Dr. Quang Duy Dao, Dr. Gilles De Romeo Banoukepa, Dr. Takuya Higashi, Dr. Junji Kobashi, Mr. Taishi Kumada, Mr. Takashi Uno, Mr. Ramananarivo Mihary Fiderana, Mr. Kento Fujita, Mr. Dai Nakagawa, Ms. Chika Nakano, Mr. Toshiki Usui, Mr. Koki Imamura, Mr. Mitsuhiro Nakatani, and Mr. Yuki Nishikawa for their kind assistance in experiments and for making my everyday life in the laboratory easy.

In addition, I thank the laboratory members who made the laboratory comfortable to live

in and study, graduate students Mr. Yusaku Anzai, Mr. Takuma Ohkawa, Mr. Yuya Nakata, Mr. Kanta Sunami, Mr. Ken Watanabe, and Mr. Shohei Yamano, Mr. Takahiro Kitagawa, Mr. Masaru Ono, Mr. Tomohiro Ouchi, and Ms. Misaki Takahashi; undergraduates Mr. Ryo Ishiura, Mr. Taiga Hiroshima, Mr. Masaya Kurokawa, Mr. Ryota Yabuuchi, and Mr. Kensuke Matsui and current and former secretaries Ms. Mitsuko Matsumoto and Ms. Chieko Nishikawa.

I also would like to extend my gratitude to the Japanese Society for the Promotion of Science (JSPS) for the grant they awarded me as a Research Fellow. Their financial support helps me to continue my study.

Finally, I appreciate my family for allowing me to continue studying so far and in the future.

Bibliography

[1] 宇佐美徳隆, 石原照也, 中島一雄 訳, 太陽電池の物理 Physics of Solar Cells, 丸善株式会社, (2010).

[2] Y. Diao, L. Shaw, Z. Bao, and S. C. Mannsfeld, "Morphology control strategies for solution-processed organic semiconductor thin films", *Energy Environ. Sci*, **7**(7), 2145–2159 (2014).

[3] J. Peet, J. Y. Kim, N. E. Coates, W. L. Ma, D. Moses, A. J. Heeger, and G. C. Bazan, "Efficiency enhancement in low-bandgap polymer solar cells by processing with alkane dithiols", *Nat. Mater.*, **6**(7), 497–500 (2007).

[4] T. Hasegawa and J. Takeya, "Organic field-effect transistors using single crystals", *Sci. Technol. Adv. Mater.*, **10**(2), 024314 (2009).

[5] C. H. Cheng, J. Wang, G. T. Du, S. H. Shi, Z. J. Du, Z. Q. Fan, J. M. Bian, and M. S. Wang, "Organic solar cells with remarkable enhanced efficiency by using a CuI buffer to control the molecular orientation and modify the anode", *Appl. Phys. Lett.*, **97**(8), 186 (2010).

[6] J. Soeda, T. Uemura, T. Okamoto, C. Mitsui, M. Yamagishi, and J. Takeya, "Inch-size solution-processed single-crystalline films of high-mobility organic semiconductors", *Appl. Phys. Express*, **6**(7), 076503 (2013).

[7] H. Iino, T. Usui, and J. Hanna, "Liquid crystals for organic thin-film transistors", *Nat. Commun.*, **6** (2015).

[8] K. Yoshino, S. Nakajima, H. B. Gu, and R. Sugimoto, "Absorption and emission spectral changes in a Poly (3-alkylthiophene) solution with solvent and temperature", *Jpn. J. Appl. Phys.*, **26**(12A), L2046 (1987).

[9] O. D. Jurchescu, J. Baas, and T. T. Palstra, "Effect of impurities on the mobility of single crystal pentacene", *Appl. Phys. Lett.*, **84**(16), 3061–3063 (2004).

[10] J. Takeya, M. Yamagishi, Y. Tominari, R. Hirahara, Y. Nakazawa, T. Nishikawa, T. Kawase, T. Shimoda, and S. Ogawa, "Very high-mobility organic single-crystal transistors with in-crystal conduction channels", *Appl. Phys. Lett.*, **90**(10), 102120 (2007).

[11] A. Braun and J. Tcherniac, "Phthalocyanines: Synthesis", *Ann. Ber*, **40**, 2709–2718 (1907).

[12] C. W. Tang, "Two-layer organic photovoltaic cell", *Appl. Phys. Lett.*, **48**(2), 183–185 (1986).

[13] K. Sakai and M. Hiramoto, "Efficient Organic p-i-n Solar Cells Having Very Thick Codeposited i-Layer Consisting of Highly Purified Organic Semiconductors", *Mol. Cryst. Liq. Cryst.*, **491**(1), 284–289 (2008).

[14] L. Li, Q. Tang, H. Li, X. Yang, W. Hu, Y. Song, Z. Shuai, W. Xu, Y. Liu, and D. Zhu, "An Ultra Closely π-Stacked Organic Semiconductor for High Performance Field-Effect Transistors", *Adv. Mater.*, **19**(18), 2613–2617 (2007).

[15] N. B. McKeown, I. Chambrier, and M. J. Cook, "Synthesis and characterisation of some 1, 4, 8, 11, 15, 18, 22, 25-octa-alkyl-and 1, 4, 8, 11, 15, 18-hexa-alkyl-22, 25-bis (carboxypropyl) phthalocyanines", *J. Chem. Soc., Perkin Trans.*, **1**(4), 1169–1177 (1990).

[16] A. Cammidge, M. Cook, S. Haslam, R. Richardson, and K. Harrison, "Mesomorphic properties of some 1, 4, 8, 11, 15, 18, 22, 25-octa-alkoxymethylphthalocyanines", *Liq. Cryst.*, **14**(6), 1847–1862 (1993).

[17] C. Piechocki, J. Simon, A. Skoulios, D. Guillon, and P. Weber, "Annelides. 7. Discotic mesophases obtained from substituted metallophthalocyanines. Toward liquid crystalline one-dimensional conductors", *J. Am. Chem. Soc.*, **104**(19), 5245–5247 (1982).

[18] A. Cherodian, A. Davies, R. Richardson, M. Cook, N. McKeown, A. Thomson, J. Feijoo, G. Ungar, and J. Harrison, "Mesogenic Behaviour of some 1, 4, 8, 11, 15, 18, 22, 25-Octa-alkylphthalocyanines", *Mol. Cryst. Liq. Cryst.*, **196**(1), 103–114 (1991).

[19] J. Simmerer, B. Glüsen, W. Paulus, A. Kettner, P. Schuhmacher, D. Adam, K.-H. Etzbach, K. Siemensmeyer, J. H. Wendorff, H. Ringsdorf, and D. Haarer, "Transient photoconductivity in a discotic hexagonal plastic crystal", *Adv. Mater.*, **8**(10), 815–819 (1996).

[20] P. G. Schouten, J. M. Warman, M. P. De Haas, J. F. Van der Pol, and J. W. Zwikker, "Radiation-induced conductivity in polymerized and nonpolymerized columnar aggregates of phthalocyanine", *J. Am. Chem. Soc.*, **114**(23), 9028–9034 (1992).

[21] H. Iino, J. Hanna, R. J. Bushby, B. Movaghar, B. J. Whitaker, and M. J. Cook, "Very high time-of-flight mobility in the columnar phases of a discotic liquid crystal", *Appl. Phys. Lett.*, **87**(13), 132102 (2005).

[22] H. Iino, Y. Takayashiki, J. Hanna, and R. J. Bushby, "Fast ambipolar carrier transport and easy homeotropic alignment in a metal-free phthalocyanine derivative", *Jpn. J. Appl. Phys.*, **44**(10L), L1310 (2005).

[23] Y. Miyake, Y. Shiraiwa, K. Okada, H. Monobe, T. Hori, N. Yamasaki, H. Yoshida, M. J. Cook, A. Fujii, M. Ozaki, and Y. Shimizu, "High carrier Mobility up to 1.4 $cm^2 \cdot V^{-1} \cdot s^{-1}$ in Non-Peripheral Octahexyl Phthalocyanine", *Appl. Phys. Express*, **4**(2), 021604 (2011).

[24] Q.-D. Dao, T. Saito, S. Nakano, H. Fukui, T. Kamikado, A. Fujii, Y. Shimizu, and M. Ozaki, "Alkyl substituent length dependence of octaalkylphthalocyanine bulk heterojunction solar cells", *Appl. Phys. Express*, **6**(12), 122301 (2013).

[25] Q.-D. Dao, T. Hori, K. Fukumura, T. Masuda, T. Kamikado, A. Fujii, Y. Shimizu, and M. Ozaki, "Effects of processing additives on nanoscale phase separation, crystallization and photovoltaic performance of solar cells based on mesogenic phthalocyanine", *Org. Electron.*, **14**(10), 2628–2634 (2013).

[26] D. Nakagawa, C. Nakano, M. Ohmori, H. Itani, Y. Shimizu, A. Fujii, and M. Ozaki, "Miscibility and carrier transport properties in binary blend system of non-peripherally octahexyl-substituted phthalocyanine analogues", *Org. Electron.*, **44**, 67–73 (2017).

[27] I. Chambrier, M. J. Cook, M. Helliwell, and A. K. Powell, "X-ray crystal structure of a mesogenic octa-substituted phthalocyanine", *J. Chem. Soc., Chem. Commun.*, (5), 444–445 (1992).

[28] T. Hori, Y. Miyake, T. Masuda, T. Hayashi, K. Fukumura, H. Yoshida, A. Fujii, Y. Shimizu, and M. Ozaki, "Dependence of alkyl-substituent length for bulk heterojunction solar cells

utilizing 1, 4, 8, 11, 15, 18, 22, 25-octaalkylphthalocyanine", *J. Photonics Energy*, **2**(1), 021004–1 (2012).

[29] S. Heutz, S. Bayliss, R. Middleton, G. Rumbles, and T. Jones, "Polymorphism in phthalocyanine thin films: Mechanism of the $\alpha \rightarrow \beta$ transition", *J. Phys. Chem. B*, **104**(30), 7124–7129 (2000).

[30] W.-Q. Deng and W. A. Goddard, "Predictions of hole mobilities in oligoacene organic semiconductors from quantum mechanical calculations", *J. Phys. Chem. B*, **108**(25), 8614–8621 (2004).

[31] S.-H. Wen, A. Li, J. Song, W.-Q. Deng, K.-L. Han, and W. A. Goddard III, "First-principles investigation of anistropic hole mobilities in organic semiconductors", *J. Phys. Chem. B*, **113**(26), 8813–8819 (2009).

[32] W. Pisula, A. Menon, M. Stepputat, I. Lieberwirth, U. Kolb, A. Tracz, H. Sirringhaus, T. Pakula, and K. Müllen, "A zone-casting technique for device fabrication of field-effect transistors based on discotic hexa-peri-hexabenzocoronene", *Adv. Mater.*, **17**(6), 684–689 (2005).

[33] H. Minemawari, T. Yamada, H. Matsui, J. Tsutsumi, S. Haas, R. Chiba, R. Kumai, and T. Hasegawa, "Inkjet printing of single-crystal films", *Nature*, **475**(7356), 364 (2011).

[34] R. D. Deegan, O. Bakajin, T. F. Dupont, G. Huber, S. R. Nagel, and T. A. Witten, "Capillary flow as the cause of ring stains from dried liquid drops", *Nature*, **389**(6653), 827 (1997).

[35] J. Kim, N. Yamasaki, T. Hayashi, M. Katayama, H. Yoshida, H. Moritake, A. Fujii, and M. Ozaki, "Effect of column disorder on carrier transport in columnar discotic liquid crystal evaluated by applying precisely controlled shear stress", *Jpn. J. Appl. Phys.*, **52**(10R), 101701 (2013).

[36] S. A. Casalnuovo, K.-C. Lim, and A. J. Heeger, "Reversible optical anisotropy and induced rigidity in polydiacetylene films", *Makromol. Chem., Rapid Communications*, **5**(2), 77–81 (1984).

[37] M. Onoda, Y. Manda, and K. Yoshino, "Anisotropy of absorption and photoluminescence spectra of stretched poly (3-alkylthiophene)", *Jpn. J. Appl. Phys.*, **29**(8R), 1490 (1990).

[38] S. Nagamatsu, W. Takashima, K. Kaneto, Y. Yoshida, N. Tanigaki, K. Yase, and K. Omote, "Backbone arrangement in " friction-transferred " regioregular poly (3-alkylthiophene) s", *Macromolecules*, **36**(14), 5252–5257 (2003).

[39] N. Van Aerle, M. Barmentlo, and R. Hollering, "Effect of rubbing on the molecular orientation within polyimide orienting layers of liquid-crystal displays", *J. Appl. Phys.*, **74**(5), 3111–3120 (1993).

[40] J. C. Wittmann and P. Smith, "Highly oriented thin films of poly (tetrafluoroethylene) as a substrate for oriented growth of materials", *Nature*, **352**(6334), 414–417 (1991).

[41] A. M. van de Craats, N. Stutzmann, O. Bunk, M. M. Nielsen, M. Watson, K. Müllen, H. D. Chanzy, H. Sirringhaus, and R. H. Friend, "Meso-Epitaxial Solution-Growth of Self-Organizing Discotic Liquid-Crystalline Semiconductors", *Adv. Mater.*, **15**(6), 495–499 (2003).

[42] H. Monobe, K. Kiyohara, N. Terasawa, M. Heya, K. Awazu, and Y. Shimizu, "Anisotropic Change of Liquid-Crystal Domains by Polarized Infrared Pulse Laser Irradiation for a Columnar Mesophase", *Adv. Funct. Mater.*, **13**(12), 919–924 (2003).

[43] I. O. Shklyarevskiy, P. Jonkheijm, N. Stutzmann, D. Wasserberg, H. J. Wondergem, P. C. Christianen, A. P. Schenning, D. M. de Leeuw, Ž. Tomović, J. Wu, K. Müllen, and J. C. Maan, "High anisotropy of the field-effect transistor mobility in magnetically aligned discotic liquid-crystalline semiconductors", *J. Am. Chem. Soc.*, **127**(46), 16233–16237 (2005).

[44] K. Nakayama, Y. Hirose, J. Soeda, M. Yoshizumi, T. Uemura, M. Uno, W. Li, M. J. Kang, M. Yamagishi, Y. Okada, E. Miyazaki, Y. Nakazawa, A. Nakao, K. Takimiya, and J. Takeya, "Patternable Solution-Crystallized Organic Transistors with High Charge Carrier Mobility", *Adv. Mater.*, **23**(14), 1626–1629 (2011).

[45] Y. Matsuo, Y. Sato, T. Niinomi, I. Soga, H. Tanaka, and E. Nakamura, "Columnar structure in bulk heterojunction in solution-processable three-layered pin organic photovoltaic devices

using tetrabenzoporphyrin precursor and silylmethyl [60] fullerene", *J. Am. Chem. Soc.*, **131**(44), 16048–16050 (2009).

[46] 工藤一浩 編, 有機トランジスタ-評価と応用技術-, シーエムシー出版, (2010).

[47] K. Yoshino, K. Tada, A. Fujii, E. M. Conwell, and A. A. Zakhidov, "Novel photovoltaic devices based on donor-acceptor molecular and conducting polymer systems", *IEEE Trans. Electron Devices*, **44**(8), 1315–1324 (1997).

[48] J. Goodisman, "Force Calculation with Hartree—Fock Wavefunctions", *J. Phys. Chem.*, **39**(9), 2397–2398 (1963).

[49] 早稲田嘉夫, 松原英一郎 著, X 線構造解析 原子の配列を決める, 内田老鶴圃, (1998).

[50] H. Yoshida, K. Inaba, and N. Sato, "X-ray diffraction reciprocal space mapping study of the thin film phase of pentacene", *Appl. Phys. Lett.*, **90**(18), 181930 (2007).

[51] 液晶便覧編集委員会 編, 液晶便覧, 丸善株式会社, (2000).

[52] T. Hori, Y. Miyake, N. Yamasaki, H. Yoshida, A. Fujii, Y. Shimizu, and M. Ozaki, "Solution processable organic solar cell based on bulk heterojunction utilizing phthalocyanine derivative", *Appl. Phys. Express*, **3**(10), 101602 (2010).

[53] J. C. Swarts, E. H. Langner, N. Krokeide-Hove, and M. J. Cook, "Synthesis and electrochemical characterisation of some long chain 1, 4, 8, 11, 15, 18, 22, 25-octa-alkylated metal-free and zinc phthalocyanines possessing discotic liquid crystalline properties", *J. Mater. Chem.*, **11**(2), 434–443 (2001).

[54] A. Fujii, H. Itani, K. Watanabe, Q.-D. Dao, L. Sosa-Vargas, Y. Shimizu, and M. Ozaki, "Improved synthesis of non-peripherally alkyl-substituted tetrabenzotriazaporphyrins", *Mol. Cryst. Liq. Cryst.*, **653**(1), 22–26 (2017).

[55] A. Fujii, S. Nakano, H. Fukui, T. Saito, M. Ohmori, Y. Shimizu, and M. Ozaki, "Ambipolar carrier mobility in binary blend thin film of non-peripheral alkylphthalocyanines", *J. Phys. Conf. Ser.*, **704**(1), 012006 (2016).

[56] A. N. Cammidge, I. Chambrier, M. J. Cook, D. L. Hughes, M. Rahman, and L. Sosa-Vargas, "Phthalocyanine Analogues: Unexpectedly Facile Access to Non-Peripherally Substituted

Octaalkyl Tetrabenzotriazaporphyrins, Tetrabenzodiazaporphyrins, Tetrabenzomonoazaporphyrins and Tetrabenzoporphyrins", *Chem. Eur. J.*, **17**(11), 3136–3146 (2011).

[57] R. A. Marcus, "Electron transfer reactions in chemistry. Theory and experiment", *Rev. Mod. Phys.*, **65**(3), 599 (1993).

[58] M. Yoneya, A. Miyamoto, Y. Shimizu, M. Ohmori, A. Fujii, and M. Ozaki, "Characterization of crystal polymorphs of the organic semiconductor non-peripheral octa-hexyl phthalocyanine", *Jpn. J. Appl. Phys.*, **56**(8), 081601 (2017).

[59] G. te Velde, F. M. Bickelhaupt, E. J. Baerends, C. Fonseca Guerra, S. J. van Gisbergen, J. G. Snijders, and T. Ziegler, "Chemistry with ADF", *J. Comput. Chem.*, **22**(9), 931–967 (2001).

[60] R. Docherty, G. Clydesdale, K. Roberts, and P. Bennema, "Application of Bravais-Friedel-Donnay-Harker, attachment energy and Ising models to predicting and understanding the morphology of molecular crystals", *J. Phys. D : Appl. Phys.*, **24**(2), 89 (1991).

[61] M. Yoneya, A. Miyamoto, Y. Shimizu, A. Fujii, and M. Ozaki, "Origin of the high carrier mobilities of nonperipheral octahexyl substituted phthalocyanine", *J. Phys. Chem. C*, **119**(42), 23852–23858 (2015).

[62] S. Alexander, J. Bernasconi, W. Schneider, and R. Orbach, "Excitation dynamics in random one-dimensional systems", *Rev. Mod. Phys.*, **53**(2), 175 (1981).

[63] K. Saito, M. Ikeda, and M. Sorai, "Thermodynamic implication of the dependence of mesomorphic transition entropy on chain-length", *J. Therm. Anal. Calorim.*, **70**(2), 345–352 (2002).

[64] T. Higashi, M. Ohmori, M. F. Ramananarivo, A. Fujii, and M. Ozaki, "Single crystal growth in spin-coated films of polymorphic phthalocyanine derivative under solvent vapor", *APL Materials*, **3**(12), 126107 (2015).

[65] V. De Cupere, J. Tant, P. Viville, R. Lazzaroni, W. Osikowicz, W. R. Salaneck, and Y. H. Geerts, "Effect of interfaces on the alignment of a discotic liquid-crystalline phthalocyanine", *Langmuir*, **22**(18), 7798–7806 (2006).

[66] T. Higashi, M. F. Ramananarivo, M. Ohmori, H. Yoshida, A. Fujii, and M. Ozaki, "Polymer blend effects on fundamental properties of mesogenic phthalocyanine films fabricated by heated spin-coating method", *Jpn. J. Appl. Phys.*, **54**(4S), 04DK08 (2015).

[67] T. Higashi, M. F. Ramananarivo, M. Ohmori, H. Yoshida, A. Fujii, and M. Ozaki, "Macroscopically aligned molecular stacking structures in mesogenic phthalocyanine derivative films fabricated by heated spin-coating method", *Thin Solid Films*, **594**, 1–4 (2015).

[68] M. F. Ramananarivo, T. Higashi, M. Ohmori, K. Sudoh, A. Fujii, and M. Ozaki, "Uniaxial crystal growth in thin film by utilizing supercooled state of mesogenic phthalocyanine", *Appl. Phys. Express*, **9**(6), 061601 (2016).

[69] T. Kitagawa, M. F. Ramananarivo, A. Fujii, and M. Ozaki, "Polymer Blend Effect on Molecular Alignment Induced by Contact Freezing of Mesogenic Phthalocyanine", *Jpn. J. Appl. Phys., in press* (2018).

[70] D. Khim, H. Han, K.-J. Baeg, J. Kim, S.-W. Kwak, D.-Y. Kim, and Y.-Y. Noh, "Simple Bar-Coating Process for Large-Area, High-Performance Organic Field-Effect Transistors and Ambipolar Complementary Integrated Circuits", *Adv. Mater.*, **25**(31), 4302–4308 (2013).

[71] T. Usui, Y. Nakata, G. D. R. Banoukepa, K. Fujita, Y. Nishikawa, Y. Shimizu, A. Fujii, and M. Ozaki, "Glass-sandwich-type organic solar cells utilizing liquid crystalline phthalocyanine", *Appl. Phys. Express*, **10**(2), 021602 (2017).

[72] Y. Nakata, T. Usui, Y. Nishikawa, F. Nekelson, Y. Shimizu, A. Fujii, and M. Ozaki, "Sandwich-cell-type bulk-heterojunction organic solar cells utilizing liquid crystalline phthalocyanine", *Jpn. J. Appl. Phys.,* **57**, 03EJ03 (2018).

[73] E. Pouzet, V. D. Cupere, C. Heintz, J. W. Andreasen, D. W. Breiby, M. M. Nielsen, P. Viville, R. Lazzaroni, G. Gbabode, and Y. H. Geerts, "Homeotropic alignment of a discotic liquid crystal induced by a sacrificial layer", *J. Phys. Chem. C*, **113**(32), 14398–14406 (2009).

[74] T. Watanabe, T. Koganezawa, M. Kikuchi, C. Videlot-Ackermann, J. Ackermann, H. Brisset, I. Hirosawa, and N. Yoshimoto, "Crystal structure of oligothiophene thin films char-

acterized by two-dimensional grazing incidence X-ray diffraction", *Jpn. J. Appl. Phys.*, **53**(1S), 01AD01 (2013).

[75] G. D. R. Banoukepa, A. Fujii, Y. Shimizu, and M. Ozaki, "1, 3, 5-Tris (phenyl-2-benzimidazole)-benzene cathode buffer layer thickness dependence in solution-processable organic solar cell based on 1, 4, 8, 11, 15, 18, 22, 25-octahexylphthalocyanine", *Jpn. J. Appl. Phys.*, **54**(4S), 04DK11 (2015).

[76] Q. Duy Dao, T. Hori, K. Fukumura, T. Masuda, T. Kamikado, A. Fujii, Y. Shimizu, and M. Ozaki, "Efficiency enhancement in mesogenic-phthalocyanine-based solar cells with processing additives", *Appl. Phys. Lett.*, **101**(26), 263301 (2012).

[77] K. Fukumura, T. Hori, T. Masuda, D. Q. Duy, A. Fujii, Y. Shimizu, and M. Ozaki, "Solvent effects on solution-processable bulk heterojunction organic solar cells utilizing 1, 4, 8, 11, 15, 18, 22, 25-octahexylphthalocyanine", *Jpn. J. Appl. Phys.*, **52**(5S1), 05DB02 (2013).

[78] M. Ohmori, H. Fukui, Q.-D. Dao, T. Kumada, A. Fujii, Y. Shimizu, and M. Ozaki, "Annealing effect in bulk heterojunction organic solar cells utilizing liquid crystalline phthalocyanine", *Jpn. J. Appl. Phys.*, **53**(5S1), 05FZ02 (2014).

[79] Q.-D. Dao, H. Fukui, S. H. Lee, M. Ohmori, T. Kumada, A. Fujii, Y. Shimizu, and M. Ozaki, "Improvement of Photovoltaic Performance of Octahexylphthalocyanine-Based Bulk-Heterojunction Solar Cells Using Various Fullerene Derivatives", *Trans. Mat. Res. Soc. Japan*, **38**(3), 463–466 (2013).

[80] D. K. Owens and R. Wendt, "Estimation of the surface free energy of polymers", *J. Appl. Polym. Sci.*, **13**(8), 1741–1747 (1969).

[81] D. Turnbull, "Kinetics of heterogeneous nucleation", *J. Chem. Phys.*, **18**(2), 198–203 (1950).

[82] T. Takahagi, I. Nagai, A. Ishitani, H. Kuroda, and Y. Nagasawa, "The formation of hydrogen passivated silicon single-crystal surfaces using ultraviolet cleaning and HF etching", *J. Appl. Phys.*, **64**(7), 3516–3521 (1988).

[83] I. Bouchoms, W. Schoonveld, J. Vrijmoeth, and T. Klapwijk, "Morphology identification of the thin film phases of vacuum evaporated pentacene on SiO 2 substrates", *Synth. Met.*, **104**(3), 175–178 (1999).

[84] A. Pivrikas, N. S. Sariciftci, G. Juška, and R. Österbacka, "A review of charge transport and recombination in polymer/fullerene organic solar cells", *Prog. Photovoltaics Res. Appl.*, **15**(8), 677–696 (2007).

[85] G. Dennler, A. Mozer, G. Juška, A. Pivrikas, R. Österbacka, A. Fuchsbauer, and N. Sariciftci, "Charge carrier mobility and lifetime versus composition of conjugated polymer/fullerene bulk-heterojunction solar cells", *Org. Electron.*, **7**(4), 229–234 (2006).

[86] A. Pivrikas, H. Neugebauer, and N. S. Sariciftci, "Charge carrier lifetime and recombination in bulk heterojunction solar cells", *IEEE J. Sel. Top. Quantum Electron.*, **16**(6), 1746–1758 (2010).

[87] G. Kumar, J. Thomas, N. Unnikrishnan, V. Nampoori, and C. Vallabhan, "Optical absorption and emission spectral studies of phthalocyanine molecules in DMF", *J. Porphyrins Phthalocyanines*, **5**(05), 456–459 (2001).

[88] F. Nekelson, K. Miyamoto, Q.-D. Dao, K. Fukumura, T. Nakao, H. Yoshida, A. Fujii, M. Ozaki, and Y. Shimizu, "Self-Organized Nano-Structure and Charge Transport Property of Non-Peripheral Octahexylphthalocyanine /PCBM Binary Mixtures for Bulk Heterojunction Organic Solar Cell", *submitted to J. Mater. Chem. C.*

[89] T. Hori, T. Shibata, V. Kittichungchit, H. Moritou, J. Sakai, H. Kubo, A. Fujii, and M. Ozaki, "MoO_3 buffer layer effect on photovoltaic properties of interpenetrating heterojunction type organic solar cells", *Thin Solid Films*, **518**(2), 522–525 (2009).

[90] T. Umeda, T. Shirakawa, A. Fujii, and K. Yoshino, "Improvement of characteristics of organic photovoltaic devices composed of conducting polymer-fullerene systems by introduction of ZnO layer", *Jpn. J. Appl. Phys.*, **42**(12A), L1475 (2003).

[91] T. Hori, A. Semba, S. Lee, H. Kubo, A. Fujii, and M. Ozaki, "Active layer analysis of interpenetrating heterojunction organic thin-film solar cells by X-ray photoelectron spectroscopy", *Thin Solid Films*, **554**, 222–225 (2014).

Achievements

Publications

[1] Quang-Duy Dao, Hitoshi Fukui, Sun Hwan Lee, Masashi Ohmori, Taishi Kumada, Akihiko Fujii, Yo Shimizu, and Masanori Ozaki,

"Improvement of photovoltaic performance of octahexylphthalocyanine-based bulk-heterojunction solar cells using various fullerene derivatives",

Transactions of the Materials Research Society of Japan, Vol. 38, No. 3, pp. 463–466 (2013).

[2] Masashi Ohmori, Hitoshi Fukui, Quang-Duy Dao, Taishi Kumada, Akihiko Fujii, Yo Shimizu, and Masanori Ozaki,

"Annealing effect in bulk heterojunction organic solar cells utilizing liquid crystalline phthalocyanine",

Japanese Journal of Applied Physics, Vol. 53, No. 5S1, pp. 05FZ02–1–4 (2014).

[3] Quang-Duy Dao, Taishi Kumada, Hitoshi Fukui, Masashi Ohmori, Akihiko Fujii, Yo Shimizu, and Masanori Ozaki,

"Blend ratio dependence of photovoltaic properties in octahexylphthalocyanine-based small molecule solar cell",

Japanese Journal of Applied Physics, Vol. 53, No. 5S1, pp. 05FZ05–1–4 (2014).

[4] Takuya Higashi, Mihary Fiderana Ramananarivo, Masashi Ohmori, Hiroyuki Yoshida, Akihiko Fujii, and Masanori Ozaki,

"Polymer blend effects on fundamental properties of mesogenic phthalocyanine films fabricated by heated spin-coating method",

Japanese Journal of Applied Physics, Vol. 54, No. 4S, pp. 04DK08–1–4 (2015).

[5] Quang-Duy Dao, Lydia Sosa-Vargas, Takuya Higashi, Masashi Ohmori, Hiromichi Itani, Akihiko Fujii, Yo Shimizu, and Masanori Ozaki,

"Efficiency enhancement in solution processed small-molecule based organic solar cells

utilizing various phthalocyanine–tetrabenzoporphyrin hybrid macrocycles",
Organic Electronics, Vol. 23, pp. 44–52 (2015).

[6] Quang-Duy Dao, Takashi Uno, Masashi Ohmori, Koichi Watanabe, Hiromichi Itani, Akihiko Fujii, Yo Shimizu, and Masanori Ozaki,
"Effects of thermal-annealing and processing-additive treatment on crystallization-induced phase separation in organic solar cells utilizing octapentyl tetrabenzotriazaporphyrins",
Journal of Physics D: Applied Physics, Vol. 48, No. 38, pp. 385103–1–5 (2015).

[7] Takuya Higashi, Mihary Fiderana Ramananarivo, Masashi Ohmori, Hiroyuki Yoshida, Akihiko Fujii, and Masanori Ozaki,
"Macroscopically aligned molecular stacking structures in mesogenic phthalocyanine derivative films fabricated by heated spin-coating method",
Thin Solid Films, Vol. 594, pp. 1–4 (2015).

[8] Takuya Higashi, Masashi Ohmori, Mihary Fiderana Ramananarivo, Akihiko Fujii, and Masanori Ozaki,
"Single crystal growth in spin-coated films of polymorphic phthalocyanine derivative under solvent vapor",
Applied Physics Letters Materials, Vol. 3, No. 12, pp. 126107–1–6 (2015).

[9] Masashi Ohmori, Takuya Higashi, Akihiko Fujii, and Masanori Ozaki,
"Molecular Packing Structure of Mesogenic Octa-Hexyl Substituted Phthalocyanine Thin Film by X-ray Diffraction Analysis",
Journal of Nanoscience and Nanotechnology, Vol. 16, No. 4, pp. 3318–3321 (2016).

[10] Masashi Ohmori, Chika Nakano, Takuya Higashi, Tetsuya Miyano, Norimitsu Tohnai, Akihiko Fujii, and Masanori Ozaki,
"Single crystal growth and X-ray structure analysis of non-peripheral octahexyl phthalocyanine",
Journal of Crystal Growth, Vol. 445, pp. 9–14 (2016).

[11] Akihiko Fujii, Shohei Nakano, Hitoshi Fukui, Takashi Saito, Masashi Ohmori, Yo Shimizu, and Masanori Ozaki,

"Ambipolar carrier mobility in binary blend thin film of non-peripheral alkylphthalocyanines",
Journal of Physics: Conference Series, Vol. 704, No. 1, pp. 012006–1–7 (2016).

[12] Mihary Fiderana Ramananarivo, Takuya Higashi, Masashi Ohmori, Koichi Sudoh, Akihiko Fujii, and Masanori Ozaki,
"Uniaxial crystal growth in thin film by utilizing supercooled state of mesogenic phthalocyanine",
Applied Physics Express, Vol. 9, No. 6, pp. 061601–1–4 (2016).

[13] Masashi Ohmori, Takashi Uno, Mitsuhiro Nakatani, Chika Nakano, Akihiko Fujii, and Masanori Ozaki,
"Crystal structure analysis in solution-processed uniaxially oriented polycrystalline thin film of non-peripheral octahexyl phthalocyanine by grazing incidence wide-angle x-ray scattering techniques",
Applied Physics Letters, Vol. 109, No. 15, pp. 153302–1–5 (2016).

[14] Dai Nakagawa, Chika Nakano, Masashi Ohmori, Hiromichi Itani, Yo Shimizu, Akihiko Fujii, and Masanori Ozaki,
"Miscibility and carrier transport properties in binary blend system of non-peripherally octa-hexyl-substituted phthalocyanine analogues",
Organic Electronics, Vol. 44, pp. 67–73 (2017).

[15] Masashi Ohmori, Chika Nakano, Akihiko Fujii, Yo Shimizu, and Masanori Ozaki,
"Selective crystal growth of polymorphs and crystal-to-crystal thermal phase transition of non-peripherally alkyl-substituted phthalocyanine and tetrabenzotriazaporphyrin",
Journal of Crystal Growth, Vol. 468, pp. 804–809 (2017).

[16] Chika Nakano, Masashi Ohmori, Norimitsu Tohnai, Akihiko Fujii, and Masanori Ozaki,
"Single crystal preparation and x-ray structure analysis of non-peripherally alkyl-substituted phthalocyanine blends",
Journal of Crystal Growth, Vol. 468, pp. 810–815 (2017).

[17] Makoto Yoneya, Ayano Miyamoto, Yo Shimizu, Masashi Ohmori, Akihiko Fujii, and Masanori Ozaki,

"Characterization of crystal polymorphs of the organic semiconductor non-peripheral octahexyl phthalocyanine",
Japanese Journal of Applied Physics, Vol. 56, No. 8, pp. 081601–1–7 (2017).

[18] Masashi Ohmori, Mitsuhiro Nakatani, Hirotake Kajii, Ayano Miyamoto, Makoto Yoneya, Akihiko Fujii, and Masanori Ozaki,
"Fabrication of field effect transistor utilizing oriented thin film of octahexyl-substituted phthalocyanine and its electrical anisotropy based on columnar structure",
Japanese Journal of Applied Physics, Vol. 57, pp. 03EH10–1–5 (2018).

[19] Masashi Ohmori, Yuki Nishikawa, Akihiko Fujii, and Masanori Ozaki,
"Homeotropic alignment of non-peripheral octahexyl phthalocyanine in thin films and its photovoltaic properties",
Japanese Journal of Applied Physics, in press (2018).

[20] Masashi Ohmori, Mitsuhiro Nakatani, Masaya Kurokawa, Akihiko Fujii, and Masanori Ozaki,
"Molecular Packing Structure Analysis in Molecularly Oriented Thin Films of Non-peripheral Octahexyl Phthalocyanine",
Submitted to *Proc. of SPIE*, (2018).

International Conference Presentations

[1] Masashi Ohmori, Hitoshi Fukui, Dao Quang Duy, Taishi Kumada, Akihiko Fujii, Yo Shimizu, and Masanori Ozaki,
"Annealing Effect in Bulk Heterojunction Organic Solar Cells Utilizing Liquid Crystalline Phthalocyanine" (Poster Presentation 16p-PM3-7),
2013 JSAP-MRS Joint Symposia, Doshisha University, Kyoto, Japan, (September 16–20, 2013).

[2] Hitoshi Fukui, Masashi Ohmori, Taishi Kumada, Takashi Saito, Shohei Nakano, Dao Quang Duy, Akihiko Fujii, Yo Shimizu, and Masanori Ozaki,
"Organic Thin-Film Solar Cells Utilizing Mixed Liquid-Crystalline Alkyl-Phthalocyanine" (Poster Presentation 16p-PM3-6),

2013 JSAP-MRS Joint Symposia, Doshisha University, Kyoto, Japan, (September 16–20, 2013).

[3] Quang-Duy Dao, Hitoshi Fukui, Sung Hwan Lee, Masashi Ohmori, Taishi Kumada, Akihiko Fujii, Yo Shimizu, and Masanori Ozaki,
"Improvement of Photovoltaic Performance of Octahexylphthalocyanine-Based Bulk Heterojunction Solar Cells Using Processing Additives" (Poster Presentation 16p-PM3-3),
2013 JSAP-MRS Joint Symposia, Doshisha University, Kyoto, Japan, (September 16–20, 2013).

[4] Masashi Ohmori, Hitoshi Fukui, Dao Quang Duy, Taishi Kumada, Akihiko Fujii, Yo Shimizu, and Masanori Ozaki,
"Annealing Effect in Bulk Heterojunction Organic Solar Cells Utilizing Mesogenic Phthalocyanine" (Poster Presentation p-18),
International Symposium on nanophotonics and Nanomaterials 2014, Beijing, China, (January 15–17, 2014).

[5] Masanori Ozaki, Hitoshi Fukui, Shohei Nakano, Takashi Saito, Shigehiro Ikehara, Masashi Ohmori, Quang Duy Dao, Toshiya Kamikado, Makoto Yoneya, Yo Shimizu, and Akihiko Fujii,
"Performance Optimization of Solution Processable Solar Cell based on Binary Blends of Liquid-Crystalline Phthalocyanine" (Oral Presentation FC-O2.003),
25th International Liquid Crystal Conference, ILCC 2014, Trinity College Dublin, Dublin, Ireland, (September 8–11, 2014).

[6] Takuya Higashi, Mihary Fiderana Ramananarivo, Masashi Ohmori, HiroyukiYoshida, Akihiko Fujii, and Masanori Ozaki,
"Fabrication and Optical Anisotropy of Non-Peripheral Octahexylphthalocyanine Films with Large Mono-Domain" (Poster Presentation PS-10-15),
2014 International Conference on Solid State Devices and Materials (SSDM 2014), Tsukuba International Congress Center, Tsukuba, Ibaraki, Japan, (June 29–July 4, 2014).

[7] Quang-Duy Dao, Koichi Watanabe, Masashi Ohmori, Hiromichi Itani, Lydia Sosa-Vargas, Akihiko Fujii, Yo Shimizu, and Masanori Ozaki,

"High-Efficiency Bulk Heterojunction Organic Solar Cell Utilizing Various Hybrid Phthalocyanine-Tetrabenzopophyrin Macrocycles" (Oral Presentation U5.02),
2014 MRS Fall Meeting, Hynes Convention Center, Boston, USA, (November 30–December 5, 2014).

[8] Takuya Higashi, Masashi Ohmori, Mihary Fiderana Ramananarivo, HiroyukiYoshida, Akihiko Fujii, and Masanori Ozaki,
"Fabrication of Liquid-Crystalline Non-Peripheral Octahexylphthalocyanine Filmsby Heated Spin-Coating" (Poster Presentation Q3.32),
2014 MRS Fall Meeting, Hynes Convention Center, Boston, USA, (November 30–December 5, 2014).

[9] Masashi Ohmori, Takuya Higashi, Akihiko Fujii, and Masanori Ozaki,
"Study on Molecular Packing Structure of Mesogenic Octa-Hexyl Substituted Phthalocyanine Thin Film by X-ray Diffraction Analysis" (Poster Presentation PI-36),
11th International Conference on Nano-molecular Electronics, ICNME 2014, Kobe International Conference Center, Hyogo, Japan, (December 17–19, 2014).

[10] Takuya Higashi, Mihary Fiderana Ramananarivo, Masashi Ohmori, Hiroyuki Yoshida, Akihiko Fujii, and Masanori Ozaki,
"Polymer Blend Effects on Mesogenic Phthalocyanine Films Fabricated by Heated Spin-Coating Method" (Poster Presentation PP-70),
International Symposium on Functional π-Electron Systems, University of Washington, Washington, USA, (July 19–24, 2015).

[11] Takuya Higashi, Masashi Ohmori, Hiroyuki Yoshida, Akihiko Fujii, and Masanori Ozaki,
"Single Crystal Film Growth of a Phthalocyanine Derivative by Solvent-Vapor Treatments" (Poster Presentation),
13th European Conference on Molecular Electronics, University of Strasbourg, Strasbourg, France, (September 1–5, 2015).

[12] Masashi Ohmori, Takashi Uno, Chika Nakano, Akihiko Fujii, Makoto Yoneya, and Masanori Ozaki,
"Analyses of Crystal Structure and Carrier Mobility in Single Crystalline Thin Film of

Mesogenic Phthalocyanine by X-ray Diffraction and Density Functional Theory" (Poster Presentation M-12-7),

The International Conference on Science and Technology of Synthetic Metals in 2016, Guangzhou Baiyun International Convention Center (GZBICC), Guangzhou, China, (June 26–July 1, 2016).

[13] Masashi Ohmori, Takashi Uno, Chika Nakano, Akihiko Fujii, and Masanori Ozaki,

"Fabrication of Single Crystalline Thin Film of Non-Peripheral Hexyl-Substituted Phthalocyanine and its Crystal Structure Analysis with Grazing Incidence Wide-Angle X-ray Scattering Method" (Poster Presentation S34-P-004),

International Conference on Porphyrins and Phthalocyanines, Zhongshan Hotel, Zhongshan, China, (July 3–July 8, 2016).

[14] Masashi Ohmori, Chika Nakano, Akihiko Fujii, Yo Shimizu, and Masanori Ozaki,

"Mechanism of Selective Crystal Growth in Non-Peripheral Hexyl-Substituted Phthalocyanine and Tetrabenzotriazaporphyrin" (Poster Presentation ThP-T08-7),

The 18th International Conference on Crystal Growth and Epitaxy (ICCGE-18), Nagoya International Conference Center, Aichi, Japan, (August 7–12, 2016).

[15] Chika Nakano, Masashi Ohmori, Akihiko Fujii, Norimitsu Tohnai, and Masanori Ozaki,

"Single Crystal Preparation and X-ray Structure Analysis of Non-peripherally Alkyl-substituted Phthalocyanine Blends" (Poster Presentation ThP-T08-16),

The 18th International Conference on Crystal Growth and Epitaxy (ICCGE-18), Nagoya International Conference Center, Aichi, Japan, (August 7–12, 2016).

[16] Dai Nakagawa, Chika Nakano, Masashi Ohmori, Akihiko Fujii, Yo Shimizu, and Masanori Ozaki,

"Thermal Phase Transitions and Carrier Transport Properties in Binary Blend System of Non-Peripherally Octahexyl-Substituted Phthalocyanine Analogues" (Poster Presentation P1-1),

12th International Conference on Nano-Molecular Electronics, Kobe International Conference Center, Hyogo, Japan, (December 14–16, 2016).

[17] Masashi Ohmori, Mitsuhiro Nakatani, Hirotake Kajii, Akihiko Fujii, and Masanori Ozaki, "Fabrication and Electrical Anisotropy of Field Effect Transistors Based on Oriented Thin Films of Liquid Crystalline Phthalocyanine" (Poster Presentation P-B-009),
9th Inter Conference on Molecular Electronics and Bioelectronics (M&BE9), Ishikawa Ongakudo, Ishikawa, Japan, (June 26–28, 2017).

[18] Masashi Ohmori, Mitsuhiro Nakatani, Makoto Yoneya, Akihiko Fujii, and Masanori Ozaki, "Three-dimensional X-ray crystal structure analysis and electrical anisotropy of solution-processed oriented thin film utilizing liquid crystalline phthalocyanine" (Oral Presentation (Invited) 10555-12),
SPIE Photonics west 2018, The Moscone Center, San Francisco, California, United States, (January 27–February 1, 2018).

[19] Mitsuhiro Nakatani, Yuta Yabuchi, Masashi Ohmori, Genya Uzurano, Shusaku Nagano, Akihiko Fujii, and Masanori Ozaki,
"Selective Crystal Growth in Bar-coated Thin Film of Polymorphic Alkyl-substituted Phthalocyanine" (Poster Presentation),
27th International Liquid Crystal Conference, Kyoto International Conference Center, Kyoto, Japan, (July 22–27, 2018).

Domestic Conference Presentations

[1] 大森雅志，福井斉，Dao Quang Duy，熊田泰士，藤井彰彦，清水洋，尾崎雅則,
「液晶性フタロシアニンを用いたバルクヘテロ接合薄膜の光電変換特性における熱処理温度依存性」(口頭発表 18p-C6-16),
2013 年 第 74 回応用物理学会秋季学術講演会，同志社大学京田辺キャンパス, (2013 年 9 月 16–20 日).

[2] Quang Duy Dao，大森雅志，熊田泰士，藤井彰彦，清水洋，尾崎雅則,
「Efficiency Enhancement in Mesogenic - Phthalocyanine - Based Bulk Heterojunction Solar Cell By Using Solvent Mixtures」 (口頭発表 20p-C6-2),
2013 年 第 74 回応用物理学会秋季学術講演会，同志社大学京田辺キャンパス, (2013 年 9 月 16–20 日).

[3] 大森雅志，藤井彰彦，清水洋，尾崎雅則,
「液晶性フタロシアニン薄膜の X 線構造解析に関する研究」 (口頭発表 294-9),
第 294 回電気材料技術懇談会，大阪大学中之島センター, (2014 年 7 月 23 日).

[4] 大森雅志，藤井彰彦，清水洋，尾崎雅則,
「液晶性フタロシアニン薄膜の結晶構造における置換基種依存性」(口頭発表 18a-A2-7),
2014 年 第 75 回応用物理学会秋季学術講演会，北海道大学札幌キャンパス, (2014 年 9 月 17–20 日).

[5] 池原成拓，大森雅志，藤井彰彦，尾崎雅則,
「Photo-CELIV 法による液晶性フタロシアニンバルクヘテロ接合薄膜のキャリア移動度評価」(口頭発表 17a-A2-14),
2014 年 第 75 回応用物理学会秋季学術講演会，北海道大学札幌キャンパス, (2014 年 9 月 17–20 日).

[6] 熊田泰士，Gilles De Romeo Banoukepa，大森雅志，Quang Duy Dao，藤井彰彦，尾崎雅則,
「液晶性フタロシアニンを用いた有機薄膜太陽電池における高分子ドナー材料添加効果」(口頭発表 17a-A1-8),
2014 年 第 75 回応用物理学会秋季学術講演会，北海道大学札幌キャンパス, (2014 年 9 月 17–20 日).

[7] 東卓也，大森雅志，Mihary Fiderana Ramananarivo，吉田浩之，藤井彰彦，尾崎雅則,
「加熱スピンコート法を用いた液晶性フタロシアニン薄膜の作製及び基礎物性評価」(口頭発表 18a-A5-11),
2014 年 第 75 回応用物理学会秋季学術講演会，北海道大学札幌キャンパス, (2014 年 9 月 17–20 日).

[8] 東卓也，Mihary Fiderana Ramananarivo，大森雅志，吉田浩之，藤井彰彦，尾崎雅則,
「加熱スピンコート法による液晶性フタロシアニン配向膜の作製」(口頭発表 OME2014-41),
電子情報通信学会有機エレクトロニクス研究会，大阪大学中之島センター, (2014 年 10 月 10 日).

[9] 大森雅志，東卓也，藤井彰彦，尾崎雅則,
「Non-peripheral 型ヘキシルフタロシアニン薄膜における X 線構造解析」(ポスター発表 G6-23),

平成 26 年電気関係学会関西連合大会，奈良先端科学技術大学院大学, (2014 年 11 月 23–24 日).

[10] 大森雅志，東卓也，藤井彰彦，尾崎雅則,
「アルキル鎖長の異なる液晶性フタロシアニンの薄膜 X 線構造解析」(口頭発表 14a-D14-2),
2015 年 第 62 回応用物理学会春季学術講演会，東海大学 湘南キャンパス, (2015 年 3 月 11–14 日).

[11] 藤井彰彦，Quang Duy Dao，大森雅志，渡辺光一，井谷弘道，Lydia Sosa Vargas，清水洋，尾崎雅則,
「ベンゾトリアザポルフィリン誘導体の基礎物性とバルクヘテロ接合薄膜太陽電池における光電変換特性」(口頭発表 11a-D15-10),
2015 年 第 62 回応用物理学会春季学術講演会，東海大学 湘南キャンパス, (2015 年 3 月 11–14 日).

[12] 大森雅志，清水洋，藤井彰彦，尾崎雅則,
「液晶性フタロシアニン薄膜の結晶構造におけるアルキル鎖長依存性」(口頭発表 299-11),
第 299 回 電気材料技術懇談会，大阪大学中之島センター, (2015 年 7 月 22 日).

[13] 大森雅志，中野知佳，東卓也，藤内謙光，藤井彰彦，尾崎雅則,
「Non-peripheral 位にヘキシル基を有するフタロシアニン誘導体の単結晶作製と X 線構造解析」(口頭発表 16a-2N-2),
第 76 回応用物理学会秋季学術講演会，名古屋国際会議場, (2015 年 9 月 13–16 日).

[14] 大森雅志，中野知佳，東卓也，藤内謙光，藤井彰彦，尾崎雅則,
「Non-Peripheral 型ヘキシルフタロシアニン薄膜の分子パッキング構造と単結晶の多形構造解析」(口頭発表 6),
電子情報通信学会有機エレクトロニクス研究会，大阪大学中之島センター, (2015 年 10 月 23 日).

[15] 大森雅志，中野知佳，東卓也，藤内謙光，藤井彰彦，尾崎雅則,
「薄膜内における non-peripheral 型ヘキシルフタロシアニンの分子パッキング構造の決定」(ポスター発表 P-12),
平成 27 年電気関係学会関西連合大会，摂南大学 寝屋川キャンパス, (2015 年 11 月 14–15 日).

[16] 大森雅志，宇野貴志，中野知佳，藤内謙光，藤井彰彦，尾崎雅則,
「微小角入射広角 X 線散乱による液晶性フタロシアニン配向薄膜の結晶構造解析」(口頭発表 22a-W631-3),
2016 年第 63 回応用物理学会春季学術講演会，東京工業大学大岡山キャンパス, (2016 年 3 月 19–22 日).

[17] 宇野貴志，大森雅志，中谷光宏，藤井彰彦，尾崎雅則,
「バーコート法による液晶性フタロシアニン分子配向薄膜の作製」(口頭発表 19a-P2-21),
2016 年第 63 回応用物理学会春季学術講演会，東京工業大学大岡山キャンパス, (2016 年 3 月 19–22 日).

[18] 中野知佳，大森雅志，藤内謙光，藤井彰彦，尾崎雅則,
「Non-peripheral 型アルキル置換フタロシアニンの単結晶作製と X 線構造解析」(ポスター発表 1Pf038),
第 65 回高分子学会年次大会，神戸国際会議場, (2016 年 5 月 25–27 日).

[19] 仲川大，渡辺光一，藤田健斗，大森雅志，藤井彰彦，清水洋，尾崎雅則,
「液晶性フタロシアニン類縁体混合材料の混和性とキャリア輸送特性」(ポスター発表 3Pa075),
第 65 回高分子学会年次大会，神戸国際会議場, (2016 年 5 月 25–27 日).

[20] 臼井稔喜，Banoukepa Gilles De Romeo，大森雅志，藤井彰彦，尾崎雅則,
「1,4,8,11,15,18,22,25-オクタヘキシルフタロシアニン薄膜の光伝導における膜厚依存性」(ポスター発表 3Pa077),
第 65 回高分子学会年次大会，神戸国際会議場, (2016 年 5 月 25–27 日).

[21] 藤田健斗，Dao Quang Duy，仲川大，大森雅志，藤井彰彦，清水洋，尾崎雅則,
「液晶性フタロシアニン類縁体混合ドナー材料を用いたバルクヘテロ接合薄膜太陽電池の作製」(ポスター発表 3Pd060),
第 65 回高分子学会年次大会，神戸国際会議場, (2016 年 5 月 25–27 日).

[22] 仲川大，渡辺光一，藤田健斗，大森雅志，藤井彰彦，清水洋，尾崎雅則,
「液晶性有機半導体の混和性とキャリア移動度評価」 (口頭発表 304-11),
第 304 回電気材料技術懇談会，三菱電機 先端技術総合研究所, (2016 年 7 月 14 日).

[23] 大森雅志，中野知佳，藤井彰彦，米谷慎，清水洋，尾崎雅則,
「液晶性フタロシアニンの結晶間相転移挙動と結晶多形形成過程に関する研究」(ポスター発表 PA61),
2016 年日本液晶学会討論会，大阪工業大学大宮キャンパス, (2016 年 9 月 5 日).

[24] 仲川大，中野知佳，大森雅志，藤井彰彦，清水洋，尾崎雅則,
「フタロシアニン類縁体混合液晶における熱相転移挙動とキャリア輸送特性」(ポスター発表 PB61),
2016 年日本液晶学会討論会，大阪工業大学大宮キャンパス, (2016 年 9 月 5 日).

[25] 大森雅志，宇野貴志，中野知佳，藤井彰彦，尾崎雅則,
「塗布法によるフタロシアニン配向薄膜の作製および微小角入射広角 X 線散乱による結晶構造解析」(口頭発表 13p-B5-7),
第 77 回応用物理学会秋季学術講演会，朱鷺メッセ, (2016 年 9 月 13–16 日).

[26] 大森雅志，宇野貴志，中谷光宏，中野知佳，藤内謙光，藤井彰彦，尾崎雅則,
「溶液プロセスによるフタロシアニン誘導体配向薄膜の作製と三次元 X 線結晶構造解析」(口頭発表 3),
電子情報通信学会有機エレクトロニクス研究会，大阪大学 吹田キャンパス銀杏会館, (2016 年 9 月 30 日).

[27] 中野知佳，大森雅志，藤内謙光，藤井彰彦，尾崎雅則,
「Non-peripheral 型アルキル置換フタロシアニン単結晶における異種分子混合効果」(ポスター発表 P-12),
電子情報通信学会有機エレクトロニクス研究会，大阪大学 吹田キャンパス銀杏会館, (2016 年 9 月 30 日).

[28] 仲川大，中野知佳，大森雅志，藤井彰彦，清水洋，尾崎雅則,
「液晶性フタロシアニン類縁体混合系の熱相転移観察とキャリア移動度評価」(口頭発表 G6-2),
平成 28 年電気関係学会関西連合大会，大阪府立大学中百舌鳥キャンパス, (2016 年 11 月 22–23 日).

[29] 中野知佳，大森雅志，藤井彰彦，藤内謙光，尾崎雅則,
「Non-peripheral 型アルキル置換フタロシアニン系 2 成分混晶における分子パッキング構造」

(口頭発表 B1-O20-002),

第 26 回日本 MRS 年次大会，横浜開港記念会館, (2016 年 11 月 22–23 日).

[30] 大森雅志，中谷光宏，梶井博武，藤井彰彦，尾崎雅則,

「液晶性フタロシアニンのバーコート配向薄膜を用いた電界効果トランジスタの作製と電気的異方性」(口頭発表 16a-302-9),

第 64 回応用物理学会春季学術講演会，パシフィコ横浜, (2017 年 3 月 14–17 日).

[31] 中谷光宏，大森雅志，藤井彰彦，尾崎雅則,

「バーコート法によるフタロシアニン薄膜の作製と分子配向特性」(ポスター発表 15a-P8-15),

第 64 回応用物理学会春季学術講演会，パシフィコ横浜, (2017 年 3 月 14–17 日).

[32] 大森雅志，中谷光宏，藤井彰彦，尾崎雅則,

「微小角入射広角 x 線散乱法を用いた液晶性フタロシアニン配向薄膜の三次元構造解析」(ポスター発表 P47/J-21),

第 14 回 SPring-8 産業利用報告会，川崎市産業振興会館, (2017 年 8 月 31 日–9 月 1 日).

[33] 大森雅志，中谷光宏，梶井博武，藤井彰彦，尾崎雅則,

「アルキルフタロシアニン配向薄膜を用いた電界効果トランジスタの作製とカラムナー構造に基づく電気的異方性」(口頭発表 7a-A203-7),

第 78 回応用物理学会秋季学術講演会，福岡国際会議場, (2017 年 9 月 5–8 日).

[34] 中谷光宏，大森雅志，藤井彰彦，尾崎雅則,

「結晶多形を有するペンチルフタロシアニンのバーコート薄膜における分子配向および結晶構造評価」(口頭発表 6p-A413-1),

第 78 回応用物理学会秋季学術講演会，福岡国際会議場, (2017 年 9 月 5–8 日).

[35] 中谷光宏，大森雅志，藤井彰彦，尾崎雅則,

「結晶成長を伴うペンチルフタロシアニンのバーコート製膜における多形選択性」(口頭発表 7),

電子情報通信学会有機エレクトロニクス研究会，大阪大学中之島センター, (2017 年 11 月 17 日).

[36] 大森雅志，黒川真紗也，西川裕己，藤井彰彦，尾崎雅則,

「カラムナー液晶性半導体の薄膜中におけるホメオトロピック配向過程の評価と光電変換特

性」(口頭発表 18p-G205-6),
第 65 回応用物理学会春季学術講演会，早稲田大学西早稲田キャンパス, (2018 年 3 月 17–20 日).

[37] 大森雅志，中野知佳，米谷慎，藤井彰彦，尾崎雅則,
「アルキルフタロシアニンの結晶多形と結晶間熱相転移挙動」 (口頭発表 18a-G205-4),
第 65 回応用物理学会春季学術講演会，早稲田大学西早稲田キャンパス, (2018 年 3 月 17–20 日).

[38] 中谷光宏，大森雅志，永野修作，藤井彰彦，尾崎雅則,
「種結晶添加バーコート法により作製したペンチルフタロシアニン分子配向薄膜の結晶構造評価」(口頭発表 18a-G205-5),
第 65 回応用物理学会春季学術講演会，早稲田大学西早稲田キャンパス, (2018 年 3 月 17–20 日).

Adopted Projects

[1] 平成 27 年度日本学術振興会特別研究員 (DC1)
「新規分子配向技術を用いた液晶性有機半導体太陽電池の高性能化に関する研究」

[2] SPring-8 2016 年前期実施課題:大学院生提案型課題 (2016A1776)
「微小角入射広角 X 線散乱を用いた液晶性フタロシアニン配向薄膜の結晶構造解析」

Award

[1] 平成 26 年電気関係学会関西連合大会奨励賞 (2015 年 2 月 5 日)
「Non-peripheral 型ヘキシルフタロシアニン薄膜における X 線構造解析」

Database

[1] Crystal structure in Cambridge Structural Database (CSD)
Database identifier : SOZBUE01
Deposition number : 1440748

Appendix

Optimization of fabrication conditions for bar-coated films

Figure A.1 shows the POM images of bar-coated thin films, which were observed with crossed polarizers. A bar-coated thin film was fabricated under the following conditions; sweep rate v of 30, 120, and 200 µm/s, and the solution concentration n of 10, 20, 40, and 60 g/L. Brush-like domains in the case of (v, n) = (200 µm/s, 10 g/L), (120 µm/s, 10 g/L), and (200 µm/s, 20 g/L) were observed, which indicate that the uniaxial orientation in the thin film was not induced. The dark and bright domains in the images changed to the bright and dark ones when the polarizers were rotated by 45°, respectively, which indicated that the difference in the color of the domains was caused by the difference in the direction of the molecular orientation of C6PcH$_2$. All of these films were thinner than 20 nm, as shown in Fig. 5.4. In the other cases, uniformly dark and bright images were obtained at the extinction and diagonal position, respectively, which indicated that a uniform and uniaxial molecular oriented thin film was obtained.

Figure A.2 shows the AFM images and surface profiles of the bar-coated films, fabricated at a sweep rate of 200 µm/s and the solution concentration of 20 or 60 g/L. The island growth can be seen in Fig. A.2(a), which is the an initial state of a typical film formation process. In this cases, many nuclei were formed in the thin films, and the uniaxially oriented thin film could not be fabricated. This result must be caused by a short supply of C6PcH$_2$. In contrast, terrace and step morphology was observed on the surface of a single-crystal (Fig. A.2(b)). The results indicate that uniaxial crystal growth occurred in the thin film.

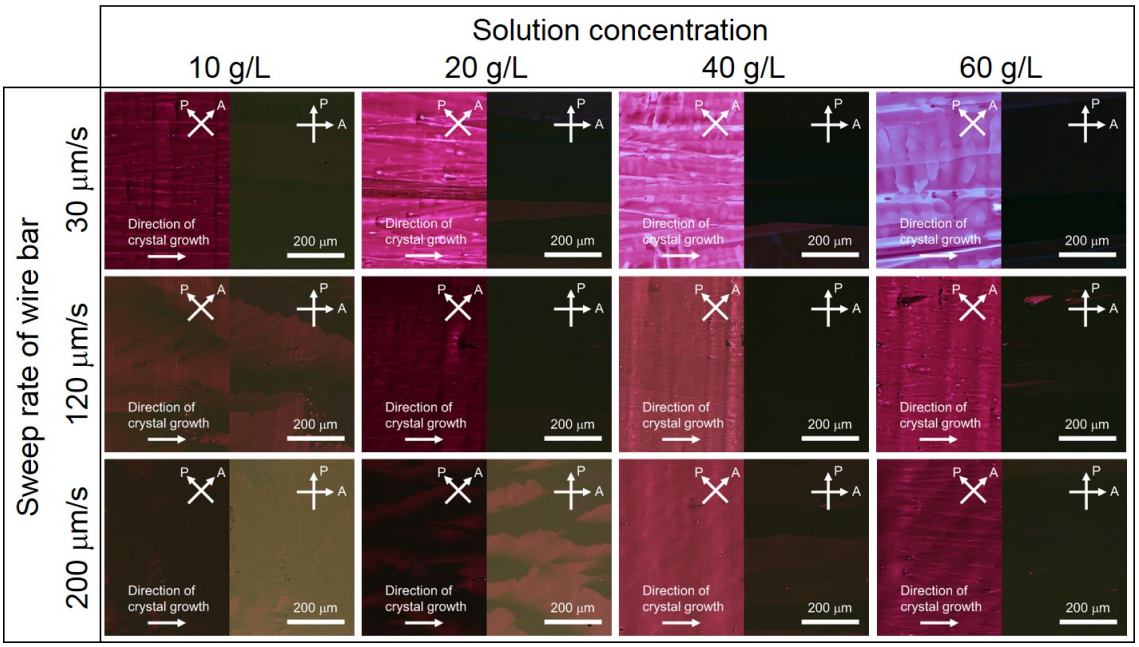

Fig. A.1 POM images of bar-coated thin films, observed with crossed polarizers. The bar-coated thin film was fabricated under the following conditions: the sweep rate of 30, 120, and 200 μm/s, and the solution concentration of 10, 20, 40, and 60 g/L.

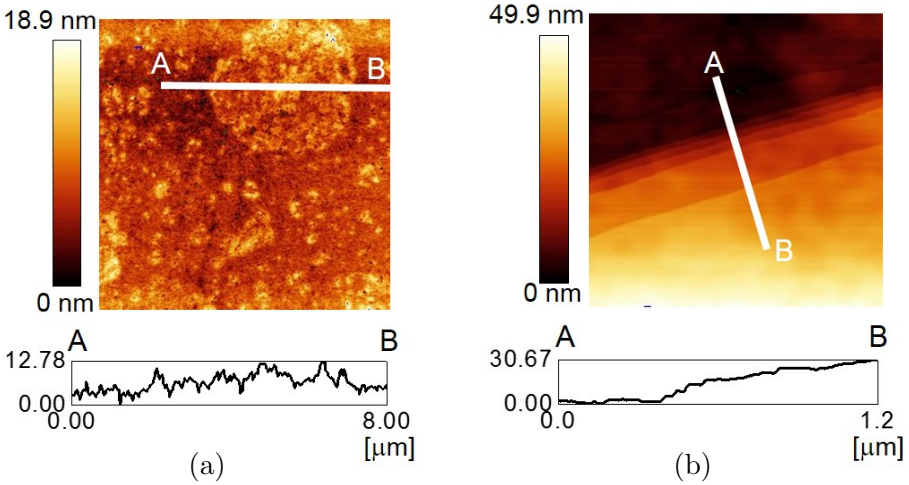

Fig. A.2 AFM images and surface profiles of a bar-coated thin films of $C6PcH_2$, fabricated at a sweep rate of 200 μm/s and the solution concentration of (a) 20 or (b) 60 g/L. The profiles correspond to the white lines in the images.